Aus dem Insitut für Experimentelle Ophthalmologie
der Medizinische Fakultät
der Universität des Saarlandes, Homburg (Saar)
Direktor: Prof. Dr. Achim Langenbucher

Simulation Study of the Visual Errors for Individualized Phakic and Pseudophakic eyes

Dissertation zur Erlangung des Grades eines Doktors
der Naturwissenschaften
der Medizinischen Fakultät
der Universität des Saarlandes
2024

vorgelegt von
Pooria Omidi
geboren am 19. Juni 1993 in Teheran

Tag der mündlichen Prüfung:	09. Mai 2025
Dekan:	Prof. Dr. Michael Menger Institut für Klinisch-Experimentelle Chirurgie
Berichterstatter:	Prof. Dr. Achim Langenbucher Institut für Experimentelle Ophthalmologie
	Prof. Dr. Frank Schmitz Institut für Anatomie und Zellbiologie

Contents

1 Summary

Purpose

The primary aim of this study is to conduct an exhaustive and scientifically rigorous analysis of visual errors in both individualized phakic and pseudophakic eyes. By scrutinizing the specific visual errors that manifest in these distinct ocular conditions, our research seeks to advance our comprehension of the intricate factors influencing visual acuity and quality. This investigation holds the promise of providing invaluable insights into the design and refinement of corrective procedures for individuals with phakic and pseudophakic eyes, ultimately enhancing their overall visual outcomes and quality of life.

At the core of our scientific inquiry lies the objective of enhancing our understanding of the multitude of optical phenomena and visual disturbances associated with cataract surgery and corneal surface modeling. This ambitious goal will be achieved through the development and application of advanced ray tracing models, meticulously tailored to assess the repercussions of intraocular lens (IOL) misalignment on the optical performance of post-cataract surgery eyes. Our focus encompasses the exploration of how lens decentration and tilt impact aberrations such as coma, astigmatism, and defocus. Additionally, we aspire to determine the precise number of Zernike coefficients necessary for an accurate representation of corneal surface geometry, all while rigorously evaluating the fitting quality of models derived from these coefficients. Furthermore, our research endeavors extend to the simulation and evaluation of the photic effects observed after cataract surgery across various regions of the retinal surface. This comprehensive examination aims to quantify the relative intensity of these effects, providing invaluable insights into the nature and magnitude of associated visual disturbances. Such a multifaceted and thorough scientific approach is poised to make substantial contributions to the field of ophthalmological research, potentially ushering in an era of improved surgical outcomes and an overall heightened quality of life for patients grappling with these conditions.

Methods

In this study, we employed ray tracing simulations, corneal surface decomposition to comprehensively investigate the optical performance of the eye. The methods employed in these two distinct aspects of our research are detailed below:

Ray Tracing Simulations:

In order to simulate the lens misalignments, ray tracing was carried out using the Liou-Brennan schematic model of the eye. The lens was horizontally dislocated and tilted relative to the eye's vertical axis. Our investigation covered a dislocation range from -1 mm to 1 mm in increments of 0.2 mm and a tilt range from -10° to 10° in steps of 0.2°. This resulted in a total of 121 combinations of tilt and decentration, which were simulated to assess their impact on the optical performance of the eye. For each configuration, we calculated defocus, astigmatism (in 0/180°), and horizontal coma by analyzing the wavefront error at the image plane. These simulations were conducted for both phakic and pseudophakic eye models, and the results were recorded for a fixed pupil size of 4 mm.
We have also used the same model eye to simulate postoperative photic effects. This time, our model incorporated implanted intraocular lenses (IOLs) with power values of 21 diopters (dpt) and optic diameters of 6 mm and 7 mm. Our analysis encompassed variations in the incident ray angle from 0° to 90° temporally, with increments of 1°. To evaluate the relative intensity of photic effects, we positioned four different detectors within specific regions of the eye during these simulations. These detectors were situated at the pupil, the retina (foveal region), the edge surface of the IOLs, and the periphery of the nasal side of the retina. Additionally, the simulations were repeated with different designs of the IOLs' edge surfaces. This variation in optical properties allowed us to discern the causes of the observed photic effects. For the ray tracing simulations, we employed the ZEMAX ray tracing software (Version 19.8, Washington, USA), using sequential and non-sequential ray tracing modes and an extended light source with a 6 mm diameter.

Corneal Surface Decomposition:

In our comprehensive study, we embarked on an in-depth analysis of clinical records obtained from a cohort of 30 patients who were admitted to the esteemed Saarland University Clinical Centre in Homburg, Germany. The cornerstone of our investigation

revolved around the utilization of a cutting-edge 3D swept-source OCT system known as CASIA2, developed by TOMEY Inc. in Nagoya, Japan. This state-of-the-art technology enabled us to meticulously assess corneal topography with precision and detail. To ensure the robustness and representativeness of our study, our sample was thoughtfully divided into two distinct primary groups. The first group was composed of 15 healthy, normal volunteers whose eyes served as the baseline for our analysis. In stark contrast, the second group encompassed 15 patients at various stages of the Belin Ambrosio keratoconus severity classification, offering us a comprehensive spectrum of corneal conditions to examine.
Within the treasure trove of data at our disposal were height maps meticulously extracted from both the anterior and posterior corneal surfaces, strategically limited to the central 8 mm zone. Importantly, these measurements were derived from native corneas with no history of prior eye surgery, ensuring the purity of our dataset. The process of deriving meaningful insights from this wealth of data involved a rigorous computational approach. We employed normalized Zernike functions to meticulously analyze the corneal height maps, utilizing the least squares regression technique. This method allowed us to iteratively refine our analysis, progressively increasing the number of polynomials until we achieved an optimal fit for the dataset. The volume of variations in the fit error value served as our guiding light in selecting the appropriate radial degree for the Zernike functions. Notably, all these complex data selection and analysis procedures were conducted with precision and expertise using the versatile MATLAB R2019b software, ensuring the highest level of accuracy and reliability in our findings. Our study aimed not only to shed light on the intricacies of corneal topography but also to exemplify the meticulous methodology and cutting-edge technologies that define modern ophthalmic research.

Results

Similar to the methods section, the results are categorized into two distinct aspects of our research, which are detailed below:

Ray Tracing Simulations:

The simulation revealed significant optical characteristics for phakic and pseudophakic eyes when the lens was positioned according to the Liou-Brennan schematic model eye. Specifically, we observed a defocus of 0.026 dpt/-0.001 dpt, astigmatism of -0.045 dpt/-0.018 dpt, and a coma of -0.015 m/0.047 m. Notably, the maximum values for defocus, astigmatism, and coma were recorded at 1.0 mm of horizontal decentration and 10° of vertical axis tilt, reaching 1.547 dpt/2.982 dpt for defocus, 0.971 dpt/1.871 dpt for astigmatism, and 0.441 m/1.209 m for coma.
In addition to these findings, our research also delved into the effects of incident ray angles on light distribution in the eye. We observed variations in light shape and intensity at different detectors located on the fovea, the nasal side of the retina, and the edge surface of the IOLs. Notably, specific incident angles of 77.5° (6 mm IOL) and 78.2° (7 mm IOL) resulted in light being detected in the foveal region. Furthermore, altering the IOLs' edge surface design to incorporate fully reflective, anti-reflective, and scattering surfaces allowed for shifts in the light intensity and shape on various detectors. It's worth noting that the absorbing edge design resulted in negligible intensity at most detectors for incident ray angles exceeding 5°.

Corneal Surface Decomposition:

The results demonstrated that fitting more Zernike polynomials to the corneal height data up to a certain point reduces the fit error. After that certain point, the fit error value does not significantly change as more fitted Zernike terms are added, and the slope of the changes progressively approaches zero. Another observed result is that there is more error fluctuation in the topographic shape and the fit error value of the posterior surface is higher in comparison to the anterior surface of the cornea. By statistical evaluation of the series of normal and keratoconus patients, it seems that there is a correlation between the radial degrees required for modelling the anterior and posterior surfaces and the stage of the disease.

Conclusion

In this comprehensive study, we explored the intricate relationship between intraocular lens (IOL) decentration and tilt, and their consequential effects on defocus, astigmatism, and horizontal coma aberrations. These findings are of paramount importance for clinical practice, particularly in cases where artificial lens implants deviate from the ideal centration and alignment, or in instances where post-cataract surgery astigmatism cannot be fully corrected through corneal topography and keratometric readings alone.

Furthermore, our detailed analysis of the empirical data reveals a compelling insight into the behavior of corneal surfaces reconstructed using finite Zernike polynomials. Significantly, the central region of these corneal surfaces exhibits a high degree of fidelity to the original raw surface profile, indicating a radially dependent pattern in the quality of polynomial fitting. This observation underscores the necessity for employing higher-order Zernike polynomials when fitting corneas compromised by pathological conditions such as corneal ectasia, as opposed to normal, healthy corneas. The enhanced polynomial fitting facilitates a more precise representation of the corneal surface, critical for accurate diagnosis and treatment planning.

Additionally, our investigation into the photic phenomena associated with intraocular lenses (IOLs) featuring light-absorbing properties and thin edge designs presents a reassuring discovery. It was observed that the majority of disruptive photic effects, resulting from light transmission through the interspace between the IOL and the pupil, are predominantly concentrated outside the foveal region. This is a critical finding, as it suggests that such photic effects are unlikely to significantly impair visual acuity or cause substantial disturbances to patients, given their occurrence in the peripheral retinal areas far from the central fovea.

In summary, our research not only elucidates the complexities associated with IOL behavior and its optical implications but also provides valuable insights for clinical practitioners, ophthalmic surgeons, and lens designers.
Moreover, these findings contribute to a more profound understanding of corneal aberrations and the necessity for advanced mathematical models in corneal surface reconstruction. Collectively, this body of work advances our knowledge of optical phenomena and their practical applications in ophthalmology, thereby enhancing the quality of patient care and the precision of corrective lens technologies.

2 Motivation

For over two decades, analytical formulas rooted in Gaussian optics have been the conventional method for determining intraocular lens (IOL) refractive power and positioning during cataract surgery. These formulas gained popularity due to their simplicity and widespread acceptance, yielding satisfactory clinical outcomes globally. Since the 1990s, wavefront analysis has also been employed in ophthalmology to assess high-order aberrations in the human eye postoperatively. Unlike low-order aberrations, such as spherical aberration, high-order optical aberrations cannot be accurately replicated by spherical surfaces, which are the basis of analytical formulas. Consequently, calculations based solely on spherical approximations do not provide a fully personalized description of the eye.

Advancements in ophthalmic equipment have now made it feasible to characterize human corneal surface profiles. Corneal tomography allows for the measurement of anterior and posterior corneal surface heights at a micron scale. These detailed measurements enable the characterization of high-order components within the cornea that were previously inaccessible.

Despite these technological strides, certain photic effects in both natural (phakic) and surgically altered (pseudophakic) eyes remain challenging to measure experimentally. Therefore, ray tracing simulations have become essential tools for studying these phenomena. Ray tracing, a longstanding technique in optical design, involves complex calculations based on Snell's law to accurately predict light refraction. In contrast to Gaussian optics, ray tracing excels in non-paraxial scenarios, offering more precise results. While not yet standardized, the combination of corneal surface profile data and ray tracing methodologies allows for the simulation of fully personalized models that encompass wavefront errors and visual artifacts specific to individual eyes.

In summary, while Gaussian optics have historically guided IOL power calculations, recent advancements in ray tracing simulations, wavefront analysis and tomography are revolutionizing ophthalmic practices. These innovations enable a deeper understanding and more personalized approach to correcting visual aberrations, thereby enhancing clinical outcomes and patient satisfaction in ophthalmology.

3 Background

This chapter examines the human eye's optical system and the correction of its defects using Intraocular lenses (IOL). The chapter will focus primarily on the eye's optical characteristics. This representation does not aim to explore the biology or medical aspects of the eye.

3.1 Basic structure of the eye

The eye is a sensory organ. Although it is small in size, the eye arguably provides us with the most important of the five senses (vision). It collects light from the visible world around us and converts it into nerve impulses. The optic nerve transmits these signals to the brain, which forms an image thereby providing sight. From the optical point of view, the human eye is made up of different components. The main components of the human eyes are two globe-shaped structures called eyeballs, which are encircled by bony sockets in the skull called orbits. The eyeball contains all of the components of the human eye. These components must be transparent and have the appropriate surface profiles and refractive indices in order to provide high-quality retinal images.

3.1.1 Cornea

The majority of the refracting power is provided by the cornea. In an unaccommodated eye, the cornea contributes about 70% of the total power. The cornea can be divided into several layers. From the reflected light it can be seen that the front surface of the cornea is smooth and glossy. From the outside to the inner, the corneal layers are the epithelium, Bowman's membrane, the stroma, Descemet's membrane, and endothelium. Each corneal layer has its specific refractive index. The Stroma is the thickest layer, and its refractive index dominates. A compound value of the corneal refractive index of 1.376 is considered. Besides these layers, the cornea is wetted by the tear film, which covers it with a lipid film. In every blink, the tear film is evenly distributed through the eyelids with a thickness of approximately 4-7 µm. This keeps

the surface smooth and of good optical quality.
The cornea is about 0.5 mm thick in the center. Due to the small proportion of the posterior surface of the cornea in the total refractive power of the eye, the corneal refractive power is often estimated based on only the anterior corneal surface [1]. In order to still obtain the same total refractive index of the cornea, a constant ratio between the radii of curvature of the front and back surfaces of the cornea is assumed and the refractive index of the cornea is estimated using a fictitious refractive index based on the front surface curvature. The estimated refractive index is called the keratometry value.
The refractive index of the cornea varies slightly with different eye models. In the Gullstrand-LeGrand model, the refractive index of the cornea is 1.3771. In the Liou-Brennan model, the refractive index is 1.376. For industrial instruments like the IOL master, the refractive index of the cornea is set to be 1.332.
In general, a sphere can roughly represent the corneal surface. The cornea gradually flattens from the center to the periphery. The cornea can usually be defined by its asphericity and radii of curvature. On average, the cornea has a positive spherical aberration, which can be partially compensated for by the young natural lens.
The anterior corneal radius is around 7.8 mm, and asphericity varies in different studies [2]. Researchers also investigate the posterior corneal surface and report the radius around 6.4 mm [3, 4, 5].

3.1.2 Iris/Pupil

The iris is situated at an approximate distance of 3 millimeters posterior to the cornea. From an optical perspective, the central black circular aperture, known as the pupil, is positioned posterior to the cornea and anterior to the crystalline lens. The iris determines the size of the pupil and helps regulate the amount of light entering the pupil. The size of the opening is governed by the muscles of the iris, which rapidly constrict the pupil when exposed to bright light to let in less light in and expand (dilate) the pupil in dim light to let in more light.
In addition to the aberrations, diffraction at the pupil limits the resolving power of the eye according to the Rayleigh criterion. With a pupil diameter of about 2 mm, the angular resolution is 1.080' for a wavelength of 500 nm (2 mm object can just be detected at a distance of 6 m).

The size of the human pupil may also vary as a result of age, disease, trauma, or other abnormalities within the visual system, including dysfunction of the pathways controlling pupillary movement. Thus, careful evaluation of the pupils is an important part of both eye and neurologic exams.

3.1.3 Crystalline lens

The second refractive component in the eye is the crystalline lens. The lens has an adjustable shape and changes its refractive power to help the eye to focus on objects at a certain distance away. The radius of the anterior surface is about 1.7 times that of its posterior surface. In the relaxed state, the central thickness is around 3.6 mm and the biconvex structure of the lens has an equivalent diameter of around 9 mm.
The lens is built from several nested shells. At first, it was assumed that there is just one optical medium. In the more simplified representation, the lens is divided into a crystalline lens and a lens capsule, and the refractive indices are considered constant in each part. On the other hand, in the more complex models, the lens bulk is a mass of non-uniform gradient-index cellular tissue enclosed in an elastic capsule. Till now, no exact index distribution is provided but generally, the crystalline lens' refractive index is set to be 1.42. For clear vision, the lens must be transparent and have the appropriate surface profile. The natural lens increases in size throughout human life [6]. This creates new layers in the lens nucleus. Therefore, our lens deteriorates as we age and becomes less elastic due to continued growth and simultaneous dehydration. If the lens hardens significantly, the lens loses its ability to accommodate, so that close objects can no longer be focused. This can result in the need for reading glasses. Intraocular lenses are used to replace crystalline lenses clouded by cataracts.

3.1.4 Retina

The retina is a thin layer of tissue that lines the back of the eye on the inside which contains several regions. The retina's function is to collect light that has been focused by the lens, transform it into neural signals, and deliver those signals to the brain for visual recognition.
The retina has two types of photoreceptor cells that convert light into nerve impulses: rods and cones. The rods detect the light for larger field sizes without colour sensitivity

and lower resolution, but with a higher sensitivity to the brightness [7]. This is called scotopic vision. The cones are responsible for colour perception and function best in relatively bright light. There are three different types of cones in the eye, and these are responsible for different spectral ranges of visible light. If the brightness is sufficient for perception to take place entirely through the cones. This is called photopic vision. Under twilight conditions, the signal from the rods is combined with the signal from the cones and this is called mesopic vision.
The area of the sharpest vision on the retina is called the macula. There is a particularly dense concentration of visual cells at the central part of the macula which is called the fovea. The fovea is responsible for sharp central vision (foveal vision), which is necessary for humans for activities for which visual detail is of primary importance, such as reading and driving. The foveal region has the highest resolution in the entire retina but a higher cone density could not necessarily achieve a higher resolution because of the diffraction limit and the aberrations.
The foveal region, with a diameter of 1.8 mm, is not located centrally around the geometrical axis of the eye. but usually lies 2.5 mm towards the human temple (temporal region). The blind spot is another component of the retina. Since the nerve enters the eye here, no light can be detected in the blind spot.

3.1.5 Ocular axes

There are several different axes in the eye, which can be recognized. These axes are: the visual axis, optical axis, pupillary axis, line of sight axis (Videokeratometry axis), and fixation axis [8]. The optical axis is the axis of greatest symmetry of the eye and approximately passes through the centers of curvature of the refractive surfaces of the eye (cornea, lens) [9]. The visual axis goes from the fixation point to the anterior node of the eye and then continues from the posterior node to the location of the image on the retina. The beam that represents the visual axis passes through the fovea to the retina when the nodal points' function is taken into account. Considering that the pupil entrance represents the enlarged image of the pupil in the object space due to the refractive power of the cornea. The visual axis corresponds to the object-side course of the central ray of the light bundle running from the fixation point to the fovea. The direct connection between the fixation point and the fovea (facial axis) can be used as an estimate of the visual axis when the nodal points are close together.
The optical axis is perpendicular to the corneal surface and passes the iris pupil at the

midpoint. The eye adjusts itself in such a way that the fixation point is imaged on the fovea [6]. Since the fovea is offset outwards from the optical axis of the eye, the direction of gaze and the optical axis differ [8]. For this reason, other ocular axes were defined in addition to the optical axis.

The pupillary axis passes through the center of the entrance pupil and perpendicularly intersects the anterior surface of the cornea [8]. The centre of the entrance pupil is shifted towards the nasal side due to the asymmetrical imaging through the cornea system and the off-axis position of the fovea. The pupillary axis usually does not intersect the fixation point.

The line of sight axis was defined to enable better comparability between corneal measurements [10]. It passes through the centroid of the light bundle. The line of sight axis runs along the normal vertex of the corneal anterior surface. Moreover, it is the axis of the ray cone, which enters the eye through the pupil. According to studies, the line of sight axis and the optical axis are angled at a range of 3° to 8°.

The fixation axis is the connecting axis between the fixation point and the center of rotation of the eye [2]. Figure 3.1 illustrates the ocular axes.

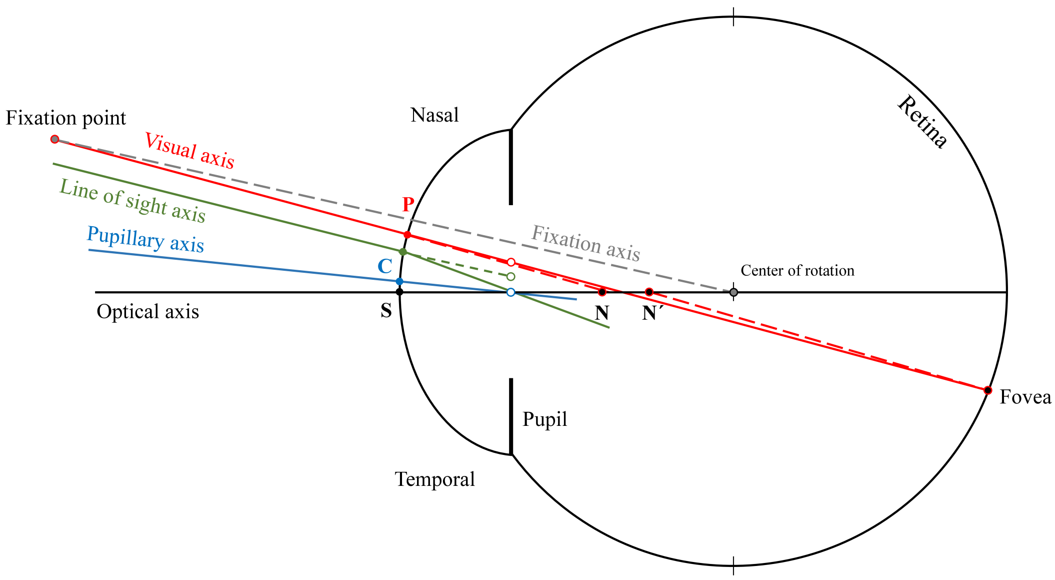

Figure 3.1: Schematic illustration of the ocular axes of the human eye. N and N' indicate object-sided and image-sided nodal points respectively.

3.2 Refractive disorders

Refractive errors or refractive disorders are a type of vision problem that makes it hard to see clearly. They occur when light cannot focus correctly on the retina. It occurs due to abnormalities in the shape of the eye or its optical components, including the cornea, lens, and eye length, typically resulting in blurred vision. Refractive errors are the most common type of vision problem. The most typical refractive disorders in which eyes do not focus light properly are astigmatism, myopia (nearsightedness), and hyperopia (farsightedness). Another well-known refractive disorder in which the crystalline lens can not change shape to allow the eye to focus on different distances is presbyopia. In addition to these common refractive errors, there are also other refractive disorders with different underlying causes. Some examples of these less common refractive disorders include cataracts and keratoconus. These disorders may arise from a variety of factors, including genetics, aging, or injury, and they can have different symptoms and treatment approaches compared to the more prevalent refractive errors. Refractive disorders may often be treated with eyeglasses, contact lenses, or refractive surgery, which attempts to adjust the light beams' pathway toward the retina [11].

3.2.1 Astigmatism

Astigmatism is a type of refractive error in which the eye's refractive power is not rotationally symmetric. Normally, the cornea and lens are smooth and curved equally in all directions. But in astigmatism, there is an imperfection in the curvature of the eye that causes blurred distance and near vision. In other words, either the corneal surfaces or the crystalline lens inside the eye has mismatched curves [12]. The astigmatic error can be corrected by eyeglasses, contact lenses, and surgery.

3.2.2 Myopia

Myopia, also known as nearsightedness, is one of the most prevalent disorders of the eye in people under the age of 40. The underlying mechanism is that the eye focuses light rays in front of the retina, instead of on the retina. Myopia is caused by the growing length of the eyeball longer than normal or the refractive elements of the eye being too strong [13]. In this condition, distant objects appear blurry while close objects appear normal. Myopia is usually correctable using optical aids such as spectacles and contact lenses or surgical means.

3.2.3 Hyperopia

Hyperopia, also known as farsightedness, is a common refractive error in which the eye can not focus on close objects properly but it can focus on distant objects without any trouble. The underlying mechanism is that the eye focuses light rays behind the retina, instead of on the retina [14]. Hyperopia is caused by the growing length of the eyeball shorter than normal or the refractive elements of the eye being not strong enough [15]. The most common treatment for hyperopia is the use of eyeglasses or contact lenses to increase the refractive power of the eye.

3.2.4 Presbyopia

Presbyopia comes from a Greek word that means “old eye”. It is a physiological error that results in insufficiency of accommodation ability to focus clearly on close objects [16]. Presbyopia occurs due to decreased elasticity and increased hardness of the crystalline lens or weakness of the ciliary muscle of the eye. Therefore the eye focuses the light behind the retina rather than on the retina. LASIK surgery, multifocal intraocular lenses, eyeglasses, and contact lenses, are all options for treating presbyopia.

3.2.5 Keratoconus

Keratoconus is a condition in which the cornea assumes a conical shape as a result of noninflammatory thinning of the corneal stroma [17]. In other words, it is an asymmetric degeneration of the cornea that leads the cornea to become thinner and conically bulge [18]. Irregular astigmatism, myopia, and protrusion caused by corneal thinning reduce vision acuity to varying degrees [19]. Keratoconus is a progressive disorder affecting both eyes, although only one eye may be affected initially [20]. Although keratoconus has been studied for decades, the cause is unknown.

It is believed to occur due to a combination of genetic, environmental, and hormonal factors [21].
Many keratoconus patients are unaware they have the disease. Symptoms are highly variable and they depend on the stage of the progression of the disorder. The earliest symptom is a slight blurring but in advanced stages, there is a significant distortion of vision, difficulty seeing at night, and sensitivity to bright light accompanied by profound visual loss. Fortunately, keratoconus patients never completely lose their vision [17].
In terms of severity, keratoconus is classified into four different stages. In the early stages, it can hardly be distinguished from refractive errors (myopia, astigmatism) but it can usually be restored with glasses or intraocular lenses. On the other hand, corneal transplant (epikeratophakia) is currently the only solution for advanced stages of keratoconus. With a cornea transplant, there is a risk that the donor tissue will be rejected by the body and/or that the desired improvement in visual quality will not completely occur. There are other alternatives to corneal transplants such as corneal ring implants (cross-linking and radial keratotomy), and utilizing lenses (hybrid lenses, scleral lenses, piggy-back Lenses).
The diagnosis of keratoconus frequently begins with an ophthalmologist's assessment of the person's medical history and continues with corneal topography, slit-lamp exam, and pachymetry. Various indicators, such as pronounced corneal curvature and low corneal thickness, are used to assess the risk of keratoconus or the stage of keratoconus [22].

3.2.6 Cataract

A cataract is a clouding that develops in the crystalline lens of the eye or its envelope, varying in degree from slight to complete opacity and obstructing the passage of light [23]. Most cataracts are related to ageing and cataracts are very common in older people. Aging is the most common cause of cataracts. But cataracts can also be caused by ionizing radiation, trauma, certain medications, or metabolic diseases. A metabolic disorder in the crystalline lens leads to proteins being stored there and scattering light. The lens changes colour and the patient suffers from symptoms. Symptoms may include faded colours, blurry or double vision, halos around light, trouble with bright lights, and trouble seeing at night [24]. Cataract typically progresses slowly. Therefore, the progression of the disease can lead to complete vision loss and is considered the

leading cause of blindness worldwide [25].
Because cataract progresses irreversibly, the only established treatment option is the surgical removal of the diseased crystalline lens [25]. For this purpose, a synthetic lens is usually implanted at the site of the natural lens to restore the lens's transparency. This procedure is called cataract surgery.
For most people, cataract surgery goes smoothly. Almost 90% of cataract operations successfully restore useful vision and they are causing little or no discomfort to the patients. But like any surgery, there are risks, especially if you have other eye problems or a serious medical condition. The most common complications of cataract surgery are infection, inflammation, retinal detachment, lens fragments, secondary cataracts, floaters and flashes of light, light sensitivity, dislocated intraocular lenses, and dysphotopsia.

3.2.6.1 Alignment errors and dislocation of intraocular lenses

After implantation, the IOLs may be slightly tilted and/or decentered. The decentering and tilting can be partially estimated from the alignment of the natural lens before the operation. In addition, there is a possible subsequent decentration if a secondary cataract forms.
Intraocular lens dislocation is a very rare condition that affects patients who have undergone cataract surgery and consists of the displacement of the implanted lens towards the vitreous cavity of the eye. IOL dislocation has been reported at a rate of 0.2% to 3% [26]. It may occur as a result of an early or late complication of cataract surgery, prior vitreoretinal surgery, trauma, or an inherent pathological process or connective tissue disorder contributing to lens zonular weakness [27].
Patients with a dislocated IOL may experience a decrease or change in vision, diplopia, and/or glare. Some patients also report seeing the edge of the IOL. IOL dislocation may present as phacodonesis, simple lens decentration within an intact capsular bag or in the sulcus, partial lens subluxation out of the capsular bag, or complete dislocation of the lens within or outside of the bag into the anterior or posterior chamber.

3.2.6.2 Secondary cataract

secondary cataract or posterior capsule opacification (PCO) is one of the most common complications of cataract surgery [23]. Up to 40-50% of all patients need some clinical follow-up or treatment due to this complication [28]. Thus, prevention of the formation of secondary cataracts is crucial to secure the outcome of cataract surgery. The secondary cataract is caused by residual lens epithelial cells that settle in the posterior lens capsule in the optic region of the intraocular lens. YAG laser treatment has become an established method to treat this postoperative complication. However, research has indicated that YAG laser treatment can cause some serious side effects, including retinal detachment and damage to the implanted intraocular lens [29, 30].
To prevent secondary cataract formation, the lens epithelial cells that remain after cataract surgery should be removed completely. This could be performed by cleaning the capsular bag [31], cryolysisof the capsule [32], or changing the intraocular lens design [33].

3.2.6.3 Dysphotopsia

Unwanted visual disturbances can arise after the implantation of IOLs. These visual symptoms, which are usually not explained by classical optics, are called Dysphotopsia. Dysphotopsias (both positive and negative) represent undesirable subjective optical phenomena that sometimes occur shortly after seemingly “perfect” cataract surgery [34]. Dysphotopsia can be quite frustrating for surgeons and patients alike, and it has been suggested that dysphotopsia is one of the leading causes of patient dissatisfaction after surgery [35]. Although dysphotopsia is often caused by cataract surgery, it can also be caused by other eye diseases, such as glaucoma and macular degeneration. This condition can affect vision, causing the patients to see things differently than they usually are. In this phenomenon light or shadows which are not directly correlated to an object are detected in the visual field and they are detected at a location where no light or shadows are expected. Clinical studies show that the photic effects caused by dysphotopsia are mostly located in the temporal visual field. This effect has been named by Tester et al. [35].
Generally, dysphotopsia can be categorized into positive (PD) and negative (ND). Since positive dysphotopsia (PD) and negative dysphotopsia (ND) likely have distinct causes, patients may experience both types. In positive dysphotopsia light is perceived

as bright patterns such as arcs, streaks, rings, or halos on the retina centrally or mid-peripherally, but not on the extreme periphery. The cause of PD is reasonably well understood, given the good correlation between optical laboratory and clinical findings. There is no systematic correlation between dysphotopsia and corneal diameter, anterior chamber depth (ACD), iris pigmentation, and photopic and scotopic pupil diameter or refraction. However studies show that there is a correlation between the size, material, and axial position of the IOL. Moreover, the IOL edge design and manufacturing quality can affect positive dysphotopsia.
On the other hand, negative dysphotopsia (ND) is the absence of light reaching certain portions of the retina that manifests as a dark shadow. ND was first described more than 20 years ago and manifests as a temporal dark crescent-shaped shadow after in-the-bag posterior chamber IOL implantation [36]. The mechanism of this disorder has remained a clinical enigma, with proposed explanations that include IOL material with a high index of refraction, cataract incision located temporally in the clear cornea, optics with a sharp or truncated edge, a prominent globe, a shallow orbit, etc [37]. The current treatment options for severe persistent negative dysphotopsia are IOL exchange with the placement of a secondary IOL in the bag or the ciliary sulcus, implantation of a supplementary IOL, reverse optic capture, and Nd: YAG anterior capsulectomy; however, in some cases, the symptoms may persist after treatment [38].

3.3 Ophthalmic lenses

Ophthalmic lenses are lenses for correcting vision in a person with visual impairments where the focal point of the eyes does not hit the retina. Lenses can also be used to address aberrations like astigmatism. Based on the severity of the refractive errors, ophthalmic lenses are utilized in various forms including plastic and glass lenses worn in glasses, contact lenses placed in direct contact with the cornea, and lenses implanted surgically inserted into the eye.

3.3.1 Spectacles

Spectacles, also known as eyeglasses. are devices worn in front of the eyes to correct refractive errors or to protect the eyes from light exposure. They are nowadays also

worn for aesthetic or fashion reasons. According to historical records, the first pair of glasses was manufactured in Egypt in the sixth century B.C. They are thought to have been made of polished crystal which was attached to the head of the wearer using a kind of fixture. At the start of the 13th century, crystals were used as lenses to improve visual acuity. Initially, only convex lenses were available, primarily to help people read and write again. The idea of utilizing concave lenses to help short-sighted patients didn't develop until the middle of the 15th century.
Spectacles are typically used for vision correction, such as with reading glasses and glasses used for nearsightedness; however, without the specialized lenses, they are sometimes used for cosmetic purposes. Today, glasses are available in a wide variety of types, such as corrective glasses, safety glasses, light protection glasses, blue-blocking, and polarising filters.

3.3.2 Contact lenses

Contact lenses are small plastic lenses placed directly on the surface of the eye to help correct refractive errors, that is to say, the loss of focus. They float on the tear film layer that coats the surface of the eye and in comparison to spectacles, contact lenses typically provide better peripheral vision. In his 1508 Codex of the Eye, Leonardo da Vinci is credited with introducing the concept of contact lenses [39]. In 1887, Louis J. Girard invented the first scleral contact lens [40]. However, the first successful afocal scleral contact lens (with 18–21 mm diameter) was invented in 1888 by German ophthalmologist Adolf Gaston Eugen Fick.
Contact lenses can be worn to correct vision or for cosmetic or therapeutic reasons [41]. There are two main types of contact lenses. They are classified into two main groups: rigid gas permeable (RGP) contact lenses and soft contact lenses. RGP lenses maintain their shape and differ from soft lenses in size and stability. They are significantly smaller than soft lenses and float on the tear film produced by the eye. On the other hand, soft lenses are more flexible than rigid lenses and can be gently rolled or folded without damaging the lens. Soft lenses adapt their shape in any direction and adjust easily to every eye bulb form, thus requiring only a short adaptation period. Contact lenses are typically used to correct refractive errors but presbyopia also can be corrected by progressive contact lenses.
Another small group of contact lenses are hybrid lenses. Typically these contact lenses consist of a rigid centre and a soft "skirt". A comparable method is "piggybacking"

a smaller, rigid lens onto the surface of a bigger, soft lens. These techniques are often chosen to give the vision correction benefits of a rigid lens and the comfort of a soft lens [42].

3.3.3 Intraocular lenses

The replacement lens implanted in the cataract surgery is called an intraocular lens or IOL. The first IOL implantation was performed in 1949. IOL implantation became widespread in the 1970s with the improvement of lens design and advance of surgical techniques. If the natural lens is left in the eye, the IOL is known as phakic, otherwise, it is a pseudophakic. Similar to a natural crystalline lens, a pseudophakic IOL performs the task of focusing light. On the other hand, The phakic IOL is used in refractive surgery to cover the existing natural lens' refractive power.
In cataract treatment, there are three ways to remove the cataract. The natural lens can be removed in its entirety with or without the capsular bag. Both methods require relatively large incisions in the cornea to remove the cataract from the eye. The third option is the modern small incision technique. The cataract inside the eye is crushed with ultrasound and then sucked out (phacoemulsification).
IOLs consist of two main components: the optic area that determines the optical properties of the IOL and the haptics that ensure it is held at the implantation site. IOLs can be classified according to implant location, optic shape, function, material, and feel. With one-piece IOLs, the haptics and optics are made of the same material. With three-piece IOLs, the haptics and optics of the IOL are manufactured independently of one another and then assembled. Haptics ensure the hold of the IOL. Therefore, their diameter depends on the implantation site. Haptics are intended to prevent alignment errors of the IOL as much as possible. The predominant haptic geometries are C- or L-shaped haptics and two-ended plate haptics. Figure 3.2 shows a schematic drawing of an intraocular lens with C-loop haptics.

The anterior chamber, sulcus (haptic is behind the iris but in front of the capsular bag) and the capsular bag can be used as implantation sites. Phakic IOLs are either implanted in the anterior chamber and fixed to the iris or positioned directly in the sulcus. The same applies to add-on IOLs, which are used in addition to the IOL implanted in the capsular bag to enable subsequent refraction correction. Most IOLs used to treat cataracts (pseudophakic IOLs) are implanted in the capsular bag at the

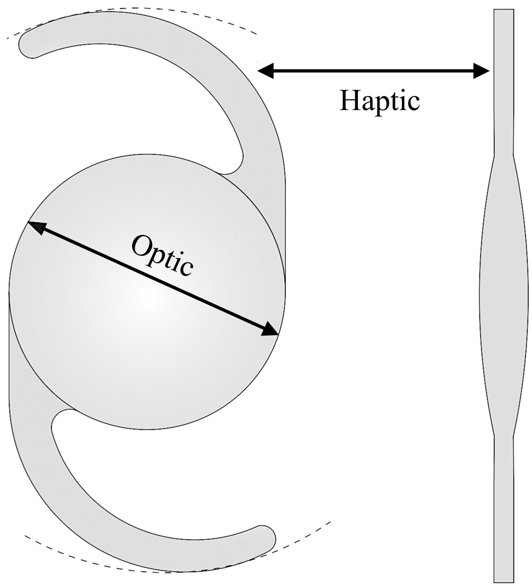

Figure 3.2: Schematic illustration of an intraocular lens from the front and side view. The IOL consists of the optic area and haptics.

site of the natural lens. If implantation in the capsular bag cannot take place, a sulcus-fixated IOL is used.
IOLs are generally categorized into hydrophilic and hydrophobic lenses. Hydrophilic IOLs have good biocompatibility, are easy to handle, and have a comparatively low refractive index (depending on the water content). Hydrophobic IOLs are characterized by higher refractive indices and lower secondary cataract rates. The first IOLs were hydrophobic and were made of polymethyl methacrylate (PMMA). This material cannot be folded; therefore, it is not suitable for small incision surgery. The unfoldable IOLS are made from materials such as silicon, acrylic polymers, and hydrogel.
By refractive behaviour, IOLs also can be distinguished as monofocal IOLs, toric IOLs, multifocal IOLs, and accommodating IOLs.

3.3.3.1 Monofocal

The monofocal IOL is the most commonly used and promising IOL type. Most IOLs fitted today are fixed monofocal lenses matched to distance vision. Within the monofocal IOLs, different designs can be distinguished like spherical IOLs and aspheric IOLs. The first IOLs had spherical optics. This continues to be the case with many IOL models. Spherical IOLs are generally biconvex spherical lenses with varying powers to attempt to match a patient's choice of primary focal length. They sharpen only one focus (far, intermediate, or near).
Atchison studied the ideal radii ratio between the IOL anterior surface and the IOL posterior surface for imaging quality with IOL implanted in the capsular bag [43, 44, 45]. He concluded that the ideal spherical IOL shape lies between a convex-planar IOL (convex front) and a biconvex IOL.
The problem for spherical IOL is the high residual spherical aberration when the pupil enlarges in dim light conditions. As spherical aberration is observed from the patients who implanted the spherical IOL, aspherical IOL designs for eliminating spherical aberration are demanded. Aspheric IOLs are classified based on their aberration correction. Aberration-correcting IOLs have negative spherical aberrations, which are intended to partially or completely compensate for the mean spherical aberration of the cornea [46]. IOLs that have no spherical aberration are referred to as aberration-free or aberration-neutral IOLs. Aberration-free IOLs also slightly influence the spherical aberration in the pseudophakic eye if its optical properties deviate from the calculation model for which the IOLs were designed [46].
Both, spherical and aspherical IOLs, only consider rotationally symmetric aberrations, the common aberration astigmatism is not taken into account in such designs. In other words, the radius of curvature in all cross-sectional meridians of the surface is similar. Therefore, the refractive power in both sagittal and tangential planes is identical. Figure 3.3 shows the front surface topography of a monofocal IOL. The IOL model used for this figure is HOYA-XY1 and the measurements were done by the NIMO wavefront sensor device.

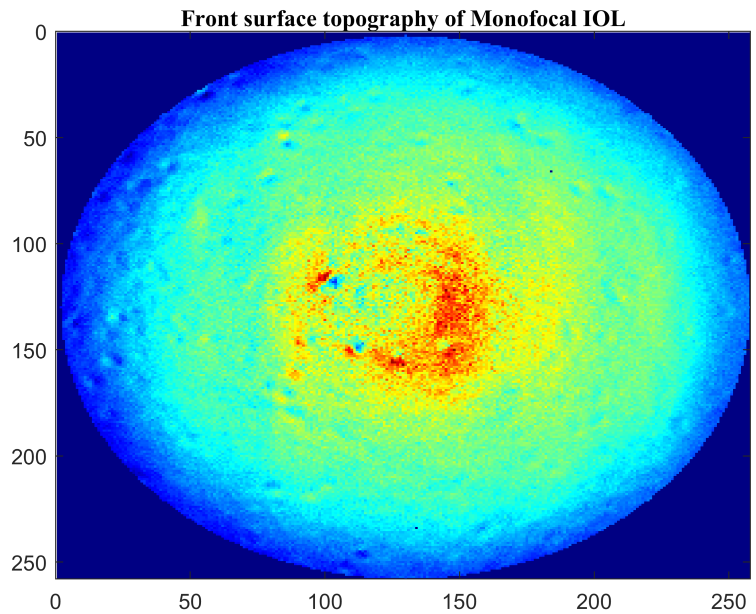

Figure 3.3: The front surface topography of the HOYA-XY1 IOL is measured by the NIMO wavefront sensor device.

3.3.3.2 Toric

Toric lenses may correct distance focus and substantially reduce astigmatism. Toric IOLs are specially crafted to correct the asymmetry associated with corneal astigmatism of 1 D. Besides rotationally symmetric aberrations, other kinds of aberrations like coma and trefoil exist. Generally in toric IOLs, the refractive power in sagittal and tangential planes is not identical. Standard toric IOLs are available in cylinder powers of 1.5 D to 6.0 D. They are usually intended for regular corneal astigmatism in a range from 0.75 D to 4.75 D and extended series or customized IOLs are available to achieve higher cylindrical power. Toric IOLs are available as monofocal and multifocal lenses. The outcomes after toric IOL implantation are influenced by numerous factors, right from the preoperative case selection and investigations to accurate intraoperative alignment and postoperative care [47]. Unfortunately, a misaligned toric IOL can cause blurred vision that cannot be easily improved with corrective lenses. Figure 3.4 shows the surface topography of a multifocal IOL. The IOL model used for this figure is ZEISS-AT TORBI and the measurements were done by the NIMO wavefront sensor device.

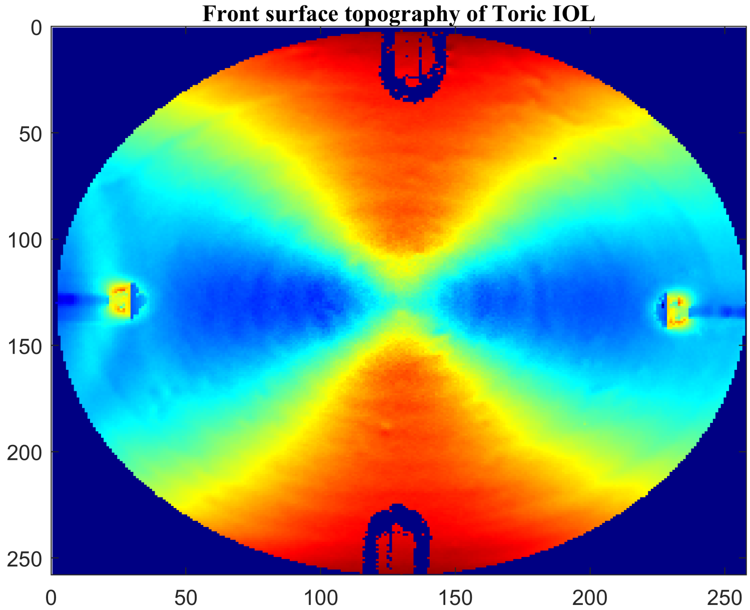

Figure 3.4: The front surface topography of the Zeiss-AT TORBI IOL is measured by the NIMO wavefront sensor device.

3.3.3.3 Multifocal and Enhanced depth of focus lenses

In the last decades, ophthalmic surgeons have been affected by alternative intraocular lens designs in addition to classical monofocal lenses. Besides toric lenses for correction of corneal astigmatism, refractive and diffractive bifocal or multifocal lenses (MF), refractive enhanced depth of focus lenses (EDOF), or monofocal plus lenses have been developed to maintain pseudophakic pseudo accommodation after cataract surgery [48].

The most common approach to correcting presbyopia is through the use of multifocal IOLs. They can be implanted in the capsular bag or as an add-on IOL. MF lenses are simultaneously generating images from objects positioned at varying distances from the retina [49]. The multifocal lens is designed with specialized segments that incorporate specific patterns, akin to the structure of Fresnel lenses. But the difference of the neighboring segments is much smaller than that in a Fresnel lens, less than half wavelength. These segments are strategically crafted to change the phase of the incident light in such a way that interference leads to high intensities in different

focal points while the intensity outside the focal points is minimized. The diffractive segments of multifocal IOLs change the phase of the incident light in such a way that interference leads to high intensities in different focal points while the intensity outside the focal points is minimized [50].
These IOLs usually have a high near addition for activities that require near and intermediate vision such as reading and working with tablets and cell phones. The difference between the refractive values of the far and near focal points is called near addition. Figure 3.5 shows the surface topography of a multifocal IOL. The IOL model used for this figure is Alcon-PanOptix and the measurements were done by the NIMO wavefront sensor device.

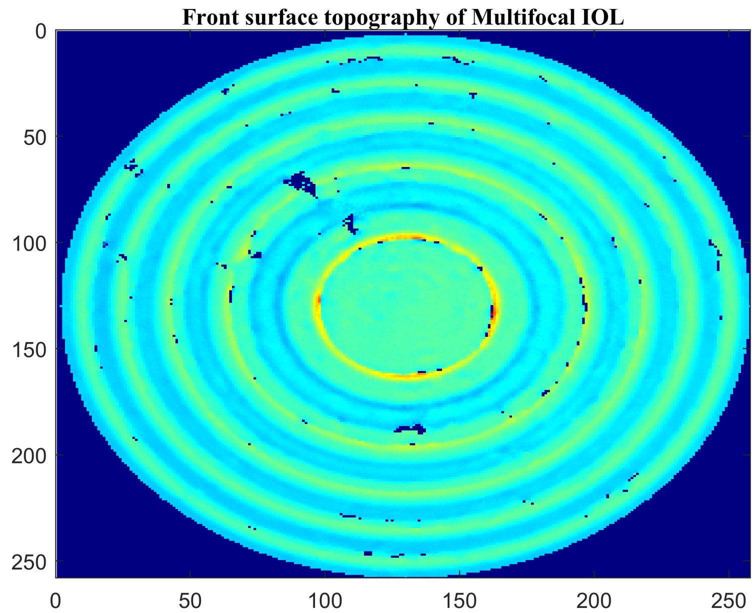

Figure 3.5: The front surface topography of the Alcon-PanOptix IOL is measured by the NIMO wavefront sensor device.

In contrast to multifocal IOLs used in the treatment of presbyopia, EDOF lenses with a low near addition have been proposed to maintain both far and intermediate-distance vision by stretching out the focal point. EDOF IOL is a new technology that has recently emerged in the treatment of Presbyopia-correcting IOLs. An increased depth of field means that the patient can see clearly over an extended distance range. These IOLs have a biconvex wavefront-designed anterior aspheric surface and a posterior achromatic diffractive surface with an echelette design. They are usually manufactured with rotationally symmetrical concentric zones with different diameters. This exclusive format creates an achromatic refractive pattern that elongates a single focal point and compensates for the chromatic aberration of the cornea. Therefore, pupil size regulates the proportion of light in the superimposed image and causes pseudo-accommodation. Both multifocal and EDOF lenses have been shown to increase levels of spectacle independence, however, both lens types may be associated with unwanted photic phenomena such as glare and halos. High levels of patient satisfaction were achieved in at least one initial study. One hundred two patients (91.1%) and 283 patients (94.6%) in the monovision and non-monovision groups, respectively, said they would recommend the same procedure to their friends and family. In the entire cohort of 411 patients, 385 (93.7%) would recommend the surgery and 388 (94.4%) would choose the same IOL again [51]. Figure 3.6 shows the surface topography of an EDOF IOL. The IOL model used for this figure is Bausch and Lomb-LuxSmart and the measurements were done by the NIMO wavefront sensor device.

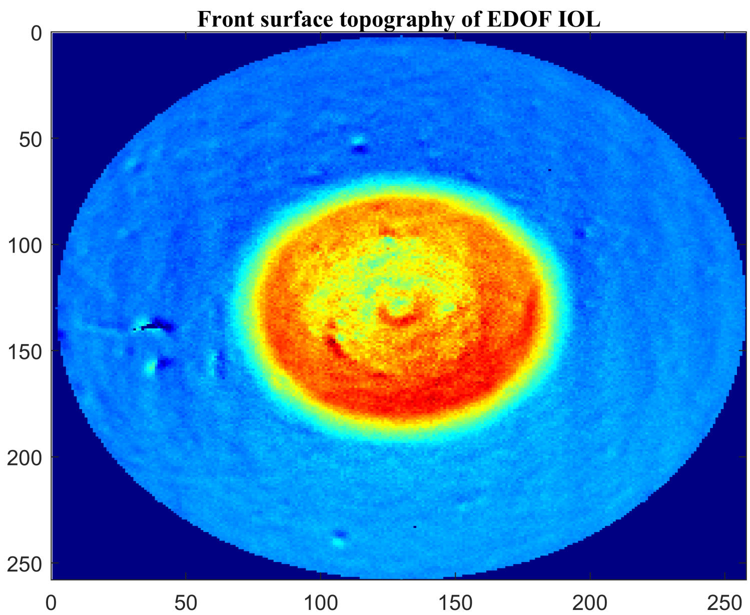

Figure 3.6: The front surface topography of the Bausch and Lomb-LuxSmart IOL is measured by the NIMO wavefront sensor device.

3.3.3.4 Intraocular lens calculation

The goal of cataract surgery is to remove the cloudy lens and adequately replace the missing refractive power. The refractive power of the IOL is often selected in such a way that the patient does not need glasses postoperatively for distance vision. The desired postoperative prescription of glasses for distance vision is called target refraction. If the patient wishes to be able to see far without glasses, slight myopia is usually aimed to avoid postoperative hyperopia. A postoperatively hyperopic patient can only see clearly at all distances with glasses.
The first theoretical formula for IOL power calculation was developed in 1967 by Fyodorov [52]. All of the formulas use the eye's axial length and corneal radius as input parameters. The radius of the cornea can be measured by keratometry. The eye's axial length can be achieved by A-scan ultrasound biometry or a partial coherent interferometer. All the formulas use Gaussian approximation and thin lens calculation. They use different strategies for lens position determination and power calculation.
The IOL calculation usually takes place in two steps. In the first step, the postoperative effective lens position (ELP) is estimated based on preoperative biometry. Various formulas are available to calculate ELP. In the second step, the IOL refractive index is calculated based on the ELP with the paraxial approach [53].

$$P = \frac{n_{Eye}}{AL - ELP} - \frac{n_{Eye}}{\dfrac{n_{Eye}}{K + \dfrac{Ref}{1 - Ref.12mm}} - ELP} \tag{3.1}$$

Some formulas require slight modifications to their ELP estimates. Alternatively, ray tracing is used. The exception to this two-step procedure is the empirical procedure of the Hill-RBF calculator [1]. However, the results of IOL power calculation depend on the accuracy of the axial length measurement. There are other sources of error, such as the accuracy of the keratometry, postoperative changes of the corneal curvature, misestimation of the postoperative anterior chamber depth, and mislabeling of IOL power.

[1] www.rbfcalculator.com

3.3.3.5 Axial position of the intraocular lens

The main source of uncertainty in current IOL power calculation formulas is variation in the preoperative estimation of postoperative IOL position, known as the estimated lens position (ELP) [54, 55]. Therefore, improvements in the ELP will provide better IOL power selection and thus refractive and visual outcomes. Since the 1970s, various theoretical formula generations have been proposed, each with a unique approach to estimating the lens positions. The first generation assumed a constant value for the ELP [56, 57]. The second generation individualized the prediction by replacing the constant ELP with one variable dependent on the axial length (AL) measured for every patient [58]. The third generation formulas used axial length and anterior corneal curvature to predict ELP [59, 60], and the fourth and fifth generations included the preoperative anterior chamber depth (ACD) to improve the prediction [61].
Predicting the postoperative axial position of the IOL in the eye based on preoperative measurements is crucial to selecting the IOL refractive power using equation 3.1. The position of the IOL in the eye can currently only be predicted by empirical estimates. There are no physiologically or physically justified descriptions of the healing process and its effects on the axial position of the IOL considering different haptic geometries and optic designs.
In order to improve the prediction of the axial IOL position, some parameters were adapted to the prediction formulas. The parameters based on the refractive results provided for this are referred to as IOL constants.

3.4 Ophthalmic devices

In the analytical formulas, the input parameters are the keratometric power of the cornea and the axial length of the eye. For ray tracing, the axial length of the eye is also a necessary input. Meanwhile, the surface profile of the cornea is another one.

3.4.1 Axial eye length measurement

Axial length (AL) is the combination of anterior chamber depth, lens thickness and vitreous chamber depth, and it is the most significant contributor to refractive error. A variety of techniques have been used to measure intraocular distances. For axial length measurement, two experimental methods are applied. The first one is to use an A-scan ultrasound measurement. The second is to use a partial coherent interferometric method. We can call one method traditional AL, and the other method sum-of-segments AL [62]. Haigis et al. calibrated this biometer to ultrasound (US)-derived ALs using a weighted-average refractive index of the whole eye. The segmental refractive indices of the eye were weighted in proportion to the segment lengths in the Gull-strand model eye to obtain one representative average refractive index for the whole eye [63]. We call this method traditional AL. Another researcher in optical biometry named Hitzenberger proposed the sum-of-segments AL method [64]. To obtain an AL, he suggested adding the geometric lengths of the ocular segments (cornea, aqueous, lens, and vitreous). However, partial coherence interferometry (PCI) (IOLMaster, Carl Zeiss Meditec AG), the original optical biometer, could only identify two locations: The anterior cornea and the retinal pigment epithelium (RPE).

3.4.1.1 Ultrasound biometry

A-scan biometry, also referred to as A-scan, utilizes an ultrasound device for diagnostic testing. The first measurements of the length of the optical axis of the eye by the ultrasonic echo-impulse techniques were performed by Franken as early as 1961 [65]. Ultrasonic measurement of the axial length of the eye has become an accepted technique to provide an essential part of the information required for preoperative intraocular lens calculation. This device can determine the length of the eye and can be useful in diagnosing common sight disorders. A-scans are also extremely beneficial

in cataract surgeries, as they enable the ophthalmologist to determine the power of the IOL needed for the artificial implant. A-scans are also used to diagnose and measure masses in the eyes.
Measuring the axial length of the eye using an A-scan is dependent upon the sound velocity of the instrument for the measurement [66]. Some instruments use an average velocity for the entire eye while others use individual velocities for each part of the eye. A-scan ultrasound biometry is a more challenging technique to use on children due to the contact nature of the instrument. It has been observed that the refractive results of IOL calculation have improved significantly with ultrasonic axial length measurement as compared to the results obtained with clinical judgment alone [67].

3.4.1.2 Interferometry with partially coherent light

Even as reliable as immersion ultrasound has been, clinicians have increasingly used optical coherence biometry for IOL calculations. The advantages of this method are high longitudinal accuracy and a high transversal resolution. In addition, it is more comfortable for the patient, because it is a noncontact method; thus, no anesthesia is needed [68]. since minimal patient cooperation is necessary for this method, it can be performed in the fully upright position by technicians with adequate training. In the interferometric technique, a statistically stationary fluctuating light beam emitted by a semiconductor laser is used. With the help of an interferometer, the optical path length of the human eye can be measured. The axial length of the eye can be calculated with the refractive indices and optical path length of the eye [69].
For example, the Carl Zeiss IOL Master uses 780 nm light to measure the distance from the retinal pigment epithelium to the corneal surface. It's quick, accurate, and doesn't require contact with the corneal surface.

3.4.2 Corneal measurements

3.4.2.1 Keratometer

Keratometry is a classic ophthalmic device. It is a diagnostic instrument for measuring the curvature of the anterior surface of the cornea, and for assessing the extent and axis of astigmatism. A keratometer uses the relationship between object size (O), image size (I), the distance between the reflective surface and the object (d), and the radius of the reflective surface (R). If three of these variables are known (or fixed), the fourth can be calculated using the formula

$$R = 2\frac{dI}{O} \tag{3.2}$$

And the power of the cornea is

$$K = \frac{n_{Cornea} - 1}{R} \tag{3.3}$$

where n is the refractive index of the cornea. There are two distinct variants of determining R; Javal-Schiotz type keratometers have a fixed image size and are 'two positions', whereas Bausch and Lomb type keratometers have a fixed object size and are usually 'one position'.

3.4.2.2 Corneal topographer

Most corneal topographers project a Placido ring pattern onto the cornea and capture the image of the Placido ring with a camera in the center. With the corneal topographer, a corneal topography composed of thousands of sampling points can be generated. By these sampling points, a more detailed corneal anterior surface characterization can be achieved.

3.4.3 Optical coherence tomography

Optical coherence tomography (OCT) is a technique that uses low-coherence light to capture micrometre-resolution, two- and three-dimensional images from the eye tissues [70]. By using the anterior segment optical coherence tomography (AS-OCT), the structure of the anterior segment (including the cornea, anterior chamber, and anterior lens surface) can be examined in one measurement. Both the corneal anterior and posterior surface height profiles and corneal thickness information can be extracted. This can provide enough information to build a surface model for individualized

corneas.
In recent years, software and hardware have advanced significantly. The OCT data obtained from devices like the IOLMaster 700 (Carl Zeiss Meditec, Jena, Germany)[2], OA-2000 (TOMEY Inc., Nagoya, Japan)[3], or EyeStar (Haag-Streit, Wedel, Germany)[4] serve various purposes in ophthalmology and eye care. Each of these instruments may have specific features and capabilities, but generally, they are used for the following purposes:

- **Cataract Surgery Planning:** Optical coherence tomography plays a pivotal role in preoperative evaluation for cataract surgery. Parameters including axial length, anterior chamber depth, and corneal curvature are precisely quantified. These measurements are essential for calculating (IOL) power, thereby ensuring accurate postoperative refractive outcomes.

- **Refractive Surgery Evaluation:** Anterior segment OCT (AS-OCT) facilitates the meticulous evaluation of corneal morphology and anterior segment structures. This is indispensable in the assessment of corneal topography, thickness, and other characteristics crucial for the planning and assessment of refractive surgeries like LASIK, PRK, and phakic IOL implantation.

- **Glaucoma Assessment:** OCT devices, including the OA-2000, are extensively utilized for the quantitative analysis of the optic nerve head and peripapillary retinal nerve fiber layer (RNFL) thickness. These measurements are pivotal in the diagnosis and monitoring of glaucoma, a progressive optic neuropathy associated with characteristic structural changes.

- **Macular and Retinal Disease Management:** OCT is a cornerstone in the assessment and management of macular and retinal pathologies, such as age-related macular degeneration (AMD), diabetic retinopathy, and macular edema. High-resolution OCT scans yield cross-sectional images of the macula, facilitating early detection, treatment monitoring, and the assessment of therapeutic efficacy.

- **Corneal Evaluation:** OCT technology enables precise imaging and assessment of the cornea. This capability is of paramount importance in the diagnosis and

[2]www.zeiss.de/meditec-ag
[3]www.tomey.de
[4]www.haag-streit.com

characterization of corneal disorders, including keratoconus, corneal dystrophies, and corneal scars. Additionally, corneal pachymetry measurements, obtained via OCT, inform various surgical interventions.

- **Anterior Segment Assessment:** OCT instruments, such as the EyeStar, contribute to the quantitative evaluation of the anterior segment, including the anterior chamber angle. This information is integral to the assessment of conditions like narrow-angle glaucoma, providing insights into anatomical structures.

- **Postoperative Monitoring:** OCT measurements serve a critical role in the postoperative phase following ocular surgeries. They are essential for tracking the healing process, detecting postoperative issues, and assessing the overall effectiveness of surgical procedures.

In summary, OCT data derived from cutting-edge devices are essential resources in contemporary ophthalmology. These measurements provide precise, high-resolution information about eye structures, facilitating accurate diagnosis, treatment strategy formulation, and ongoing monitoring for various eye conditions.
In our study, we used a 3D swept-source OCT setup called CASIA2 (TOMEY Inc., Nagoya, Japan)[5]. CASIA2 has an axial resolution of 10 µm with a scanning range of 16 µm in diameter and a maximum penetration depth of 13 mm. CASIA2 uses polar coordinates to provide several types of tomographic data such as elevation, refractive, keratometric, etc., from the anterior and posterior surfaces of the cornea. The CASIA2 software provides raw data files in both CSV and DAT formats. Each data set has 16 meridians with 16 mm of diameter, with each meridian containing 800 data points. The CASIA2 considers a tangent plane to the center of the anterior surface as a reference for measuring the height of each point.

3.4.4 Wavefront aberrometry

In the 1970s, Dr. Roland Shack and Dr. Ben Platt advanced the concept by replacing the screen with a sensor based on an array of tiny lenslets, thus creating the Hartmann-Shack sensor. In 1978, Dr. Josef Bille of Germany was the first person to use

[5] www.tomey.de

the Hartmann-Shack sensor in ophthalmology. Other wavefront pioneers include Dr. Junzhong Liang and Dr. David Williams who developed a wavefront device that could be used in a clinical setting. Wavefront analysis became a useful tool for human eye diagnostics in the 1990s [71] when the vision complaints of patients could not be explained by the normal understanding of refractive power. The visual performance can be improved in the refractive surgery process when taking the wavefront view for the activity.

The wavefront error is the optical path length difference among the rays in ray tracing. The optical path length is the summation of geometrical length multiplied by the refractive index of each media of the eye system. The shape of the refractive components will determine the optical path length. The result of the wavefront error will vary with different surface profiles.

The aberration data is converted into a treatment formula by using Zernike polynomials which are also called modes. Each mode describes a certain three-dimensional surface and the Zernike polynomials correspond with ocular aberrations. For instance, second-order Zernike polynomials represent conventional aberrations such as defocus and astigmatism. Zernike polynomials above the second order represent the higher-order aberrations that are suspected of causing glare and decreased contrast sensitivity. Zernike polynomials help to simplify wavefront technology by combining all aberrations into one simple map. This is called Zernike decomposition which is the standard way for analysis of wavefront errors.

By extracting the Zernike coefficients from the propagated wavefront, it is also possible to simulate the optical performance of each patient's eye. This capability aids in the development of individualized IOLs to correct wavefront errors and enhance visual quality. Additionally, by reconstructing the wavefront at different distances, it becomes possible to simulate the visual acuity of patients using ray tracing software.

3.5 Eye simulations

There is a need for eye simulations to model vision accurately under various conditions such as refractive surgical procedures, contact lens and spectacle wear, and near vision. Recent advances in the biometric measurement of the eye and in computerization to expedite extensive, complex optical calculations have made it possible to model the optical performance of the eye accurately. In order to investigate refractive errors in clinical and basic research studies, several mathematical eye models have been developed in recent decades.

3.5.1 Schematic eye models

The schematic eye model is a simplified statistical and mathematical model for the theoretical study of the human eye. These models represent human vision under different conditions such as refractive surgeries, spectacle wear, contact, and intraocular lens implementation. There are several theoretical eye models in the literature. The refractive elements of the eye in the schematic model eyes are the cornea and the lens. Almost all models offer two versions of the data, one for the accommodating eye and the other for the relaxed eye. All the models describe the eye by radii, distances, and refractive indices of the elements.
Since the schematic models are simplified, each value of the describing parameters is effective. The earlier models described by spherical surfaces and the refractive indices of their elements are reported for one wavelength in green. On the other hand, more modern and sophisticated eye models are described by aspherical surfaces to model spherical aberration of the eye. Furthermore, their inventors use several refractive indices and in some cases, gradient index media to model the human eye more realistically.
There is no eye model that covers all the cases which represent the human eye. Each schematic model has positive and negative aspects. These models are not realistic anatomical models and they just describe the optical properties of the human eye. Some of the well-known schematic eye models are Helmholtz-Laurance [72], Gullstrand [73], LeGrand [74], Emsley [75], Schwiegerling [76], Kooijman [77], Navarro [78], and Liou-Brennan [79].
Liou and Brennan's schematic eye is the one that most closely resembles the vivo biological eye. Therefore, in applications, such as research or product development

for customized vision correction, which must consider optical properties intrinsic to the biological eye, this model is recommended. For applications that do not require refraction-limited performance, the other models can be a good approximation [80].

3.5.2 Liou–Brennan eye

In 1997, Hwey-Lan Liou and Noel A. Brennan introduced a finite model eye by adopting empirical values of ocular parameters to produce a model structurally similar to the human eye [79].
The liou-Brennan model eye is characterized by four coaxial refracting surfaces and it has an equivalent power of 60.35 D and an axial length of 23.95 mm. The cornea of this model is defined by two rotationally symmetric surfaces with a thickness of 0.5 mm. These two rotationally symmetric surfaces (front and back surfaces) are described by radii 7.77 and 6.40 mm, and asphericities -0.18 and -0.60, respectively. The interspace between corneal surfaces is 0.5 mm.
According to the schematic model eye of Liou-Brennan, all optical elements (corneal front and back surface, lens front and back surface) are centered on the 'optical axis'. The pupil is somehow decentered by 0.5 mm in the nasal direction concerning the optical axis to consider the incident ray angle of 5° from the nasal direction so that an incident ray bundle passes through the aperture stop and is focused on the fovea. The fovea is located about 1.4 mm temporally from the optical axis. This model uses gradient media to describe crystalline lens. Therefore it predicted the aberrations of the eye very precisely. The spectral properties of this model are only applicable in the visible range and cannot be extended to the ultraviolet and infrared spectrums.
In our study, the optical performance of the eye after cataract surgery in different situations is the aspect of interest.

3.5.3 Ray tracing procedure

In physics, ray tracing emerges as a powerful method for predicting the behavior of waves or particles as they traverse through complex optical systems, characterized by varying absorption characteristics, propagation velocities, and reflective surfaces. Ray tracing, at its core, is founded on the concept that these waves or particles can be approximated as an extensive array of exceedingly narrow beams or rays.

It is important to note that ray tracing, although a valuable tool, does not encompass certain optical phenomena such as interference and diffraction. These phenomena necessitate the application of wave theory to explain their manifestations. In contrast, ray tracing is intrinsically rooted in geometric optics, making it the ideal choice for calculations about systems governed by simple ray behavior.
Compared to Gaussian optics, ray tracing boasts distinct advantages that render it indispensable in various optical applications. Firstly, ray tracing exhibits remarkable versatility in its ability to be applied to optical surfaces of varying shapes, as it primarily concerns itself with the local characteristics of the surface profile and its derivatives. This flexibility sets it apart from Gaussian optics, which predominantly accommodates the paraxial regime, making ray tracing a more universal tool for optical simulations and design. Secondly, Gaussian optics often confines itself to paraxial cases, while ray tracing operates without such limitations. By leveraging Snell's law, ray tracing enables precise calculations of refraction at interfaces with varying refractive indices, making it an invaluable asset in the accurate modeling of optical systems. Moreover, the ability to employ a large number of rays in numerical ray tracing provides a highly detailed description of the optical behavior within a given lens system. This detailed information is particularly valuable in optimizing the performance of optical components and systems.
Ray tracing models find extensive utility in a multitude of applications within optics. One notable application is the calculation of intraocular lens (IOL) refractive values. This involves assessing how IOLs interact with the eye's optical system, considering factors like lens alignment and corneal aberrations. Ray tracing methodologies offer precision in these calculations, enhancing the accuracy of IOL designs. Additionally, ray tracing is instrumental in investigating the effects of misalignment of IOLs within the eye. This detailed analysis aids in understanding and mitigating potential visual disturbances caused by IOL positioning. Furthermore, ray tracing is a powerful tool to develop personalized IOLs tailored to correct specific corneal aberrations, ensuring optimal visual outcomes for individual patients.
Ray tracing holds promise in ophthalmology, it's essential to note that its practical application may require specialized software and hardware, as well as expertise in both ophthalmology and computer graphics. As technology continues to advance, the integration of ray tracing into ophthalmic practice may become more common, potentially leading to improved patient care and outcomes. Ray tracing, with its ability to simulate light propagation through complex optical systems, has proven to be an invaluable tool in ophthalmology, particularly in the design and optimization of

intraocular lenses and the study of their interaction with the eye's optical system. Its precision and versatility make it an essential component of modern optical research and practice within the field of ophthalmology.
Numerous ray tracing software programs are available to facilitate these calculations and simulations. Prominent examples include ZEMAX, ASAP, OSLO, VirtualLab, and more. In our study, we used ZEMAX Ray Tracing Software (Version 21.3, Washington, USA) in both sequential and non-sequential ray tracing modes. This software helped us gain a better understanding of how optical systems behave and contributed significantly to our research.

3.5.3.1 ZEMAX OpticStudio

ZEMAX is a software that can model, analyze, and assist in the design of optical systems. It models many types of optical components. These include conventional spherical glass surfaces, plus aspheres, toroids, cylinders, and others. ZEMAX can also model components such as diffraction gratings, binary optics, Fresnel lenses, holograms, and others. ZEMAX has two different modes of ray tracing: sequential and non-sequential [81].
Sequential ray tracing means rays are traced from surface to surface in a predefined sequence. ZEMAX numbers surface sequentially, starting with zero for the object surface. The first surface after the object surface is 1, then 2, then 3, and so on, until the image surface is reached. Tracing rays sequentially means a ray will start at surface 0, then be traced to surface 1, then surface 2, etc. No ray will trace from surface 5 to 3; even if the physical locations of these surfaces would make this the correct path.
Non-sequential ray tracing means rays are traced only along a physically realizable path until they intercept an object. The ray then refracts, reflects, or is absorbed, depending upon the properties of the object struck. The ray then continues on a new path. In non-sequential ray tracing, rays may strike any group of objects in any order, or may strike the same object repeatedly; depending upon the geometry and properties of the objects.
In ZEMAX, each surface can be defined by different parameters like the radius of curvature, thickness, material, etc. In eye simulations, the most commonly used optical surface is spherical. The sphere is centered on the optical axis, with the vertex located at the axis position. ZEMAX treats planes as a special case of the sphere (a sphere

with an infinite radius of curvature) and conics as a special case as well. The "sag" or z-coordinate of the standard surface is given by

$$Z = \frac{cr^2}{1 + \sqrt{1 - (1+k)c^2r^2}} \tag{3.4}$$

where c is the curvature (the reciprocal of the radius), is the radial coordinate in lens units, and is the conic constant. The conic constant is less than -1 for hyperbolas, -1 for parabolas, between -1 and 0 for ellipses, 0 for spheres, and greater than 0 for oblate ellipsoids.
This formula is used to design simple spherical intraocular lenses, but to design aspherical IOLs, we should change the formula and add new terms to it. Rotationally symmetric polynomial aspheric surfaces are described by a polynomial expansion of the deviation from a spherical (or aspheric described by a conic) surface. The aspheric surface model uses the radial coordinate to describe the asphericity. The model uses the base radius of curvature and the conic constant. The surface sag is given by

$$Z = \frac{cr^2}{1 + \sqrt{1 - (1+k)c^2r^2}} + \sum_{i=1}^{n} \alpha_i r^i \tag{3.5}$$

On the other hand, toric intraocular lenses are simulated by biconic surfaces. The biconic surface is similar to the standard surface, except the conic constant and base radius may be different in the X and Y directions. The sag of a biconic surface is given by

$$Z = \frac{c_x x^2 + c_y y^2}{1 + \sqrt{1 - (1+k)c_x^2 x^2 - (1+k)c_y^2 y^2}} \tag{3.6}$$

In order to simulate alternative intraocular lens designs like EDOF IOLs, Zernike polynomials are added to the sag equation. The Zernike standard sag surface is defined by the same polynomial as the aspheric surface (which supports planes, spheres, conics, and polynomial aspheres) plus additional aspheric terms defined by the Zernike Standard coefficients. The surface sag is of the form

$$Z = \frac{cr^2}{1 + \sqrt{1 - (1+k)c^2r^2}} + \sum_{i=1}^{n} \alpha_i r^i + \sum_{i=1}^{N} A_i Z_i(\rho, \varphi) \tag{3.7}$$

where N is the number of Zernike coefficients in the series, A_i is the coefficient on the i^{th} Zernike standard polynomial, r is the radial ray coordinate in lens units, ρ is the normalized radial ray coordinate, and φ is the angular ray coordinate.

Simulating multifocal diffractive IOLs is much more challenging since in diffractive IOLs, a structure is placed on the lens surface where the shape of the structure is chosen to intentionally induce diffraction so that the waves exiting the lens will have constructive interference at distinct foci. Therefore, it is impossible to describe surface topography with a single equation.

So far, the explanations given were for surfaces with normal refractive indices. However these surfaces are not accurate enough to represent the internal structure of the crystalline lens in the phakic eye. In order to simulate the crystalline lens, the gradient surface type should be utilized. the gradient surface has the same shape as the standard surface, with media whose index of refraction is described by

$$n = n_0 + n_{r2}r^2 + n_{r4}r^4 + n_{r6}r^6 + n_{z1}z + n_{z2}z^2 + n_{z3}z^3 \tag{3.8}$$

where $r^2 = x^2 + y^2$. This surface is suitable to simulate the crystalline lens of the human eye. Eight parameters are required: the maximum step size, Δt, the base index, n_0 and the remaining six coefficients of the preceding equation. The maximum step size Δt determines the trade-off between ray tracing speed and accuracy. It should be noted that some of the coefficients have units. Table 3.1 and Table 3.2 list all the relevant parameters of the proposed phakic and pseudophakic model eye. Note that the IOL in this table 3.2 is a basic monofocal aspheric IOL with an equivalent power of 20 D.

Table 3.1: Structural parameters of the Liou-Brennan phakic eye model

Surface:type	Medium	Radius	Thickness	Semi-diameter	Conic	Delta T	n_0	n_{r2}	n_{z1}	n_{z2}
1:Standard	Cornea	7.77	0.55	5	-0.18	-	-	-	-	-
2:Standard	Aqueous	6.40	3.16	5	-0.6	-	-	-	-	-
3:Standard	Pupil	∞	0	1.5	0	-	-	-	-	-
4:Standard	Lens Front	12.40	1.59	5	0	-	-	-	-	-
5:Gradient 3	Lens Back	∞	2.43	5	0	1	1.368	-0.00198	0.04906	-0.01543
6:Gradient 3	Vitreous	-8.10	16.23	5	0.96	1	1.407	-0.00198	0	-0.00660
7:Standard	Retina	-12	-	12	0	-	-	-	-	-

Table 3.2: Structural parameters of the pseudophakic eye model

Surface:type	Medium	Radius	Thickness	Semi-diameter	Conic	α_2	α_4	α_6	α_8
1:Standard	Cornea	7.77	0.55	5	-0.18	-	-	-	-
2:Standard	Aqueous	6.40	3.16	5	-0.6	-	-	-	-
3:Standard	Pupil	∞	1	1.5	0	-	-	-	-
4:Even Asphere	IOL Front	13.86	0.97	3	0	-	-	-	-
5:Even Asphere	IOL Back	-11.66	18.69	3	-1.5	$-6.34e^{-3}$	$1.15e^{-3}$	$-3.86e^{-7}$	$-2.47e^{-8}$
6:Standard	Retina	-12	-	12	0	-	-	-	-

3.6 State of research

The main purpose of this simulation study is to increase the prediction accuracy of the optical performance of the human eye and can help us to model visual errors before and after cataract surgery. To achieve this goal, several ray-tracing simulations of phakic and pseudophakic eyes were done. All of them attempt to evaluate the optical performance of the patient's eye in uncommon conditions before or after cataract surgery.

3.6.1 Lateral position of the intraocular lens

Predicting the postoperative axial position of the IOL in the eye based on preoperative measurements is crucial for the selection of the IOL refractive power. On the other hand, predicting the lateral position of the IOL is a tool to measure the optical aberrations of pseudophakic eyes. A pseudophakic eye with optical aberrations will produce a blurred image on the retina. Low-order optical aberrations like defocus and astigmatism are common in the human eye. Besides these two, there also exist high-order optical aberrations in the human eye system.
The position of the IOL can currently only be predicted by empirical estimates. There are no physiologically or physically justified descriptions of the healing process and its effects on lateral IOL position considering different haptic geometries and optic designs of the IOL. In order to improve the prediction of the lateral IOL position and its effect on the optical performance of the eye, some parameters were adapted to the prediction formulas. The parameters provided for this are referred to as IOL constants. These IOL constants are based on the refractive results of a large number of operations with the same IOL model in such a way that the mean prediction error is as small as possible. This increases the prediction accuracy [82]. Consequently, optimization of the IOL constants is recommended [83]. In addition to optimizing IOL constants, they can be customized (personalized) specifically for a surgeon, specific patient groups, or biometric devices.
Before optimization, predicting the impact of the IOL displacement on the optical performance of the eye is crucial. With this prediction, it is possible to prioritize the aims of IOL's optics and haptics optimization. In order to be able to assess not only the influence of the IOL on the refraction of the postoperative eye but also its influence on higher-order aberrations, the description in the approximation of a thin IOL is not

sufficient.
With the help of ZEMAX simulations (sequential mode), it is possible to simulate the misaligned conditions of IOLs and their effects on the optical performance of the eye after cataract surgery. To achieve more accuracy in simulations, realistic design data from a commercialized IOL patent is used in simulations. However, the simulations can be even more realistic by using corneal surface tomography of the patients instead of using the average corneal shape reported by the statistical studies.

3.6.2 Individualized corneal surface geometry

Generally, IOLs are designed, optimized, and tested with model corneas. Model corneas have the potential to provide a better understanding of the average biometry of the human cornea. In general, the central cornea can be seen as a sphere. This is the reason why the cornea has been assigned as a sphere in the traditional calculation. However, the measurement data from modern ophthalmic devices show that the corneal shape cannot simply be seen as a sphere if a larger area of measurement is considered. In a larger area, the corneal shape can be deformed from a sphere by introducing asphericity into the corneal representation.
Even with the IOLs designed with this representation, the residual deformation errors in some patients' cornea might lead to minor visual problems like glare and halos. To solve this problem, some other corneal representations were proposed, which vary from patient to patient. This demands a more sophisticated cornea model including high-order components. However, it is crucial to understand whether our surface model with high-order components is robust enough to reliably represent the characteristics of the surface.[84, 85]
The standard way for wavefront analysis is the Zernike polynomial decomposition. These polynomials could also be used for the representation of a corneal surface. It is considered to be particularly robust against measurement noise. The problem for such high-order polynomial fitting is the appropriate order. For representing the high-order part of the corneal surface, the order of such polynomials should be high enough to describe detailed surface information. But, a higher order of the polynomial used means a more rough surface representation. Besides, the larger number of degree of freedom in the surface fit might negatively impact the robustness of the surface fit [86].
Based on the fact that the corneal surface is smooth, a high order polynomial induced

local fluctuation is not acceptable. However, a low order will not provide real superiority compared to the statistical representations. Another drawback of such a polynomial fit is that it is a global representation and it cannot deal with local changes. This is the reason why fluctuations are becoming sufficient to deteriorate the surface smoothness if the polynomial order is too high. Therefore, certain corneal pathologies can only be reproduced with sufficient accuracy by a very high degree of polynomials.
Evaluating the smoothness of a surface represented using Zernike polynomials involves several approaches. One way to start is by visually inspecting the reconstructed surface and comparing it to the original or expected smoothness criteria. This qualitative assessment can give you an initial idea of how well the surface conforms to smoothness standards. It is also possible to calculate residuals by subtracting the Zernike surface representation from the original surface data. Large residuals at specific points or regions may indicate deviations from smoothness, and visualizing these residuals with color maps or contour plots can help identify problematic areas.
There are other approaches to evaluate surface smoothness such as root mean square (RMS) error, coefficient distribution, surface derivatives, curvature analysis, and sample density. It should be mentioned that the choice of Zernike polynomial degree and the number of coefficients used can affect the representation's ability to capture surface smoothness. Adjusting these parameters may be necessary to achieve a smoother fit.
Studies showed that the advantage of such a change in corneal representation is that the individualized IOL designs are more reliable and accurate. However, the process of optimal fitting of Zernike polynomials to corneal height data is the main objective of our study.

3.6.3 Postoperative photic effects

Investigating the postoperative unwanted visual artifacts on the retina is an approach to understanding the causes of patient dissatisfaction after uncomplicated cataract surgery. There are several theories to explain this phenomenon but the exact nature of these events is incompletely understood, but there are many different theories with both clinical and laboratory evidence to support them. It seems that the leading hypotheses as to the cause of these photic effects currently include the shape, size, index of refraction, and material makeup of the intraocular lens [36, 87, 88].
One of the risk factors for these photic effects includes IOL edge design, such as truncated-edge IOLs (including both square and oval lenses), and the optical properties

of the edge surface. There is no definitive prevention method against postoperative unwanted photic effects. There is no definitive method for the prevention of these photic phenomena, but certain modifications in the edge design can reduce these effects. The other risk factor is the optic diameter of the IOLs. Studies showed that 7.0 mm optic diameter and plate haptics can reduce these photic effects.

The main purpose of our study is to simulate postoperative photic effects and the influence of the edge design on their intensity and shape of them. With the help of ZEMAX simulations (non-sequential mode), it is possible to simulate the visual artifacts generated from reflection or transmission through the edge surface of IOLs.

4 Peer Reviewed Papers

4.1 Paper 1

Title: Combination of lens decentration and tilt in phakic and pseudophakic eyes-Optical simulation of defocus, astigmatism and coma

Authors: Achim Langenbucher, Pooria Omidi, Timo Eppig, Nóra Szentmáry, Rupert Menapace, Peter Hoffmann

Publication date: 30/09/2020

Journal: The Ophthalmologist (Journal of the German Ophthalmological Society)

Volume(Issues): 118(8)

Pages: 828-837

Der Ophthalmologe

Originalien

Ophthalmologe 2021 · 118:828–837
https://doi.org/10.1007/s00347-020-01235-x
Eingegangen: 31. Juli 2020
Angenommen: 2. September 2020
Online publiziert: 30. September 2020

Achim Langenbucher[1] · Pooria Omidi[1] · Timo Eppig[1] · Nóra Szentmáry[2,3] · Rupert Menapace[4] · Peter Hoffmann[5]

[1] Institut für Experimentelle Ophthalmologie, Universität des Saarlandes, Homburg, Deutschland
[2] Dr. Rolf M. Schwiete Zentrum für Limbusstammzellforschung und kongenitale Aniridie, Universität des Saarlandes, Homburg, Deutschland
[3] Klinik für Augenheilkunde, Semmelweis-Universität, Budapest, Ungarn
[4] Universitätsklinik für Augenheilkunde und Optometrie, AKH Wien, Wien, Österreich
[5] Augen- und Laserklinik Castrop-Rauxel, Castrop-Rauxel, Deutschland

Kombination aus Dezentrierung und Verkippung der Linse im phaken und pseudophaken Auge – optische Simulation von Defokus, Astigmatismus und Coma

Die Dezentrierung und Verkippung der natürlichen Augenlinse im phaken Auge bzw. der Kunstlinse im pseudophaken Auge nach einer Kataraktoperation konnte für viele Jahre nur abgeschätzt werden [22]. Zur Verfügung standen dafür optische Messverfahren wie Purkinje-Meter oder Scheimpflug-Kameras [4, 6, 16]. Allerdings ist speziell bei Scheimpflug-Kameras das Messfeld in axiale Richtung deutlich begrenzt, da die Einhaltung der Scheimpflug-Bedingung voraussetzt, dass die Bildebene, die Linsenebene sowie die Ebene der Spaltbeleuchtung in eine Linie schneiden. Bei Purkinje-Metern sind dagegen vereinfachende Annahmen über die Grenzflächen der Hornhaut und die axiale Position der Linse und deren Krümmungsradien nötig, um absolute Messgrößen zur Dezentrierung und Verkippung der Augenlinse zu extrahieren.

Mit der neuen Generation der optischen Kohärenztomographie für den vorderen Augenabschnitt hat der Kliniker erstmals die Möglichkeit, in einer Messung mit hoher Auflösung den gesamten vorderen Augenabschnitt zu vermessen [21]. Das Messfenster von lateral deutlich mehr als 12 mm und axial mehr als 10 mm reicht aus, um neben der Hornhaut sowohl die natürliche Augenlinse wie auch die Kunstlinse nach der Kataraktoperation zu vermessen. Zum Teil existieren entsprechende Applikationen oder Messmodalitäten, die speziell für die Auswertung der Dezentrierung und Verkippung der Augenlinse entwickelt wurden [19].

Die Auswirkung der Dezentrierung oder Verkippung von Kunstlinsen wurde in der Literatur hinreichend adressiert. Meist stehen bei diesen Studien das Abbildungsverhalten oder optische Kenngrößen wie die „point spread function" oder Modulationstransferfunktion beim pseudophaken Auge im Vordergrund [1, 3–5, 7, 9–11, 13, 17, 18, 23]. So wurden vergleichende Untersuchungen an sphärischen wie auch asphärisch aberrationsneutralen und aberrationskorrigierenden Kunstlinsen durchgeführt. Systematische Untersuchungen zu Defokus und Astigmatismus oder der Veränderung der Sehachse sind selten [8, 9, 11, 19].

Betrachtet man moderne schematische Augenmodelle wie das Liou-Brennan-Auge [14], so kann direkt eine Asymmetrie in horizontaler Richtung abgelesen werde. Dadurch, dass die Fovea nach temporal ausweicht, verläuft die Sehachse nicht zentriert durch das Auge. Vielmehr wird von einer horizontalen Verkippung des Strahls von etwa 5° (Winkel alpha bzw. kappa) ausgegangen, wodurch die optischen Elemente Hornhaut und Linse gegenüber der Fixationsachse in horizontaler Richtung dezentriert und um die vertikale Achse verkippt erscheinen. In vertikaler Richtung ist dagegen in derartigen Modellaugen keine Asymmetrie vorgesehen, sodass die Hornhaut und Linse in vertikale Richtung keine Dezentrierung sowie um die horizontale Achse keine Verkippung gegenüber der Sehachse erfahren [2, 14].

Nach einer Kataraktoperation mit Implantation einer Kunstlinse in den Kapselsack richtet sich das Implantat in der Regel so aus, dass sich die Haptikebene der Linse näherungsweise in der Äquatorebene der natürlichen Linse positioniert [20, 21]. Das bedeutet, dass die Kunstlinse in grober Abschätzung eine Dezentrierung und Verkippung zur Fixationsachse aufweist, die vergleichbar der natürlichen Linse ist.

Allerdings wurden nach unserem Kenntnisstand der zu erwartende Defokus, Astigmatismus sowie die Coma am phaken und pseudophaken Auge bei horizontaler Dezentrierung in Kombination mit einer Verkippung um die vertikale Achse nicht systematisch untersucht.

Das Ziel der vorliegenden Arbeit ist es, in einem Simulationsmodell, basierend auf dem schematischen Modellauge nach Liou-Brennan, die natürliche Linse in horizontale Richtung zu dezentrieren sowie um die vertikale Achse zu verkippen und den resultierenden Defokus, Astigmatismus sowie die Coma in der Fokalebene zu ermitteln. Des Weiteren soll die natürliche Linse durch eine aberrationskorrigierende Kunstlinse ersetzt werden, und am pseudophaken Auge sollen ebenfalls der resultierende Defokus, Astigmatismus sowie die Coma bei Dezentrierung der Linse in horizontale Richtung und Verkippung um die vertikale Achse untersucht werden.

Methoden

Als Ausgangspunkt für die Simulation in ZEMAX wird das schematische Modellauge nach Liou-Brennan herangezogen [14]. Das Auge ist so definiert, dass der Eingangsstrahl in horizontale Richtung um 5° nach nasal geneigt ist und somit die Fixationsachse gegenüber der Symmetrieachse geneigt ist [2, 14, 19]. Für die Blende des optischen Systems wird ein Durchmesser von 4 mm in der Pupillenebene gewählt, sodass auch bei einer Dezentrierung von 1 mm sowie einer Verkippung von 10° kein Strahl außerhalb der pseudophaken Linsenoptik verläuft, wenn man einen typischen Optikdurchmesser von 6 mm annimmt [12]. Die Fovea wird in die Ebene mit dem besten Fokus gelegt. Als Beleuchtung wurde ein monochromatischer (Wellenlänge = 500 nm) kollimierter Eingangsstrahl (entsprechend einem Objekt im Unendlichen) definiert.

Ausgehend von dieser Konstellation, wird die kristalline Linse des Auges in einem Bereich von ±1,0 mm (Schrittweite 0,2 mm) in horizontale Richtung dezentriert sowie in einem Bereich von ±10° (Schrittweite 2°) um die vertikale Achse verkippt. Somit ergeben sich insgesamt 11 × 11 = 121 Szenarien für Kombinationen aus Dezentrierung und Verkippung. Für jedes Szenario wurden der resultierende Astigmatismus, der Defokus sowie die Coma als die wichtigsten optischen Abbildungsfehler bei dezentrierten und verkippten Grenzflächen protokolliert. Die Wellenfrontfehler Defokus und Astigmatismus wurden zur besseren Interpretation in Dioptrien umgerechnet.

In einem zweiten Schritt wurde die natürliche Augenlinse mit Gradientenindex gegen eine aberrationskorrigierende Kunstlinse ausgetauscht (Modell: Z9000 der Fa. Advanced medical Optics, Santa Ana, CA, USA, jetzt Johnson & Johnson Vision, Brechwert 21 dpt, Designdaten wurden aus der Patentschrift entnommen [4]). Die Linse wurde so im Auge positioniert, dass die Haptikebene der Kunstlinse nach der Äquatorebene der natürlichen Linse ausgerichtet wurde. Anschließend wurde die Bildebene so gewählt, dass sie in der Ebene des besten Fokus zu liegen kommt. Ausgehend von dieser Positionierung, wurde die Kunstlinse in einem Bereich von ±1,0 mm (Schrittweite 0,2 mm) horizontal dezentriert sowie in einem Bereich von ±10° (Schrittweite 2°) um die vertikale Achse verkippt. Auch hier wurden insgesamt 121 Kombinationen aus Dezentrierung und Verkippung berücksichtigt. Vergleichbar zum Vorgehen beim phaken Liou-Brennan-Modellauge wurden der Defokus, der resultierende Astigmatismus sowie die Coma protokolliert. Die Wellenfrontfehler Defokus und Astigmatismus wurden zur besseren Interpretation in Dioptrien umgerechnet.

Die ◻ Abb. 1 zeigt exemplarisch das pseudophake Augenmodell (nach Ersatz der natürlichen Augenlinse durch eine Kunstlinse) eines rechten Auges von oben. Die ◻ Abb. 1a kennzeichnet die Dezentrierung der Linse um +1,0 mm in horizontale Richtung und ◻ Abb. 1b die Verkippung um die vertikale Achse um +10°. Die entsprechende Situation für linke Augen ergibt sich durch eine Spiegelung an der vertikalen Achse.

Zur grafischen Aufarbeitung der Ergebnisse wurden Darstellungen gewählt, bei denen, ausgehend von der Positionierung der Augenlinse im Liou-Brennan-Modellauge (entsprechend Dezentrierung und Verkippung gleich null), die Dezentrierung der Linse in horizontale Richtung auf der Abszisse, die Verkippung der Linse um die vertikale Achse auf der Ordinate und die Zielgrößen Defokus, Astigmatismus oder Coma in Farbe kodiert aufgetragen wurden.

Ergebnisse

Bei der Dezentrierung der Linse in horizontale Richtung sowie Verkippung um die vertikale Achse (Gradientenlinse im phaken Auge oder Kunstlinse im pseudophaken Auge) sind der resultierende Astigmatismus in den schrägen Achsen (45°/135°) sowie die vertikale Coma (90°) gleich null. Somit konnte vereinfachend auf die Darstellung des schrägen Astigmatismus (45° bzw. 135°) sowie der vertikalen Coma verzichtet werden.

Ist die Linse im phaken/pseudophaken Auge entsprechend den Vorgaben im Liou-Brennan-Modellauge positioniert, ergibt sich ein Defokus von 0,026/–0,001 dpt, ein Astigmatismus in 0° von –0,045/–0,018 dpt sowie eine horizontale Coma von –0,015/0,047 µm.

Die ◻ Abb. 2 zeigt die Abhängigkeit der Zielgrößen Defokus, Astigmatismus und Coma für verschiedene Kombinationen aus horizontaler Dezentrierung der Linse und Verkippung der Linse um die vertikale Achse für das phake Augenmodell. Aufgrund der Wahl der Bildebene im „best focus" ist der Defokus ohne Dezentrierung und Verkippung (Dezentrierung und Verkippung der natürlichen Linse entsprechen den Gegebenheiten des Liou-Brennan-Modellauges) sehr gering. Die zugehörigen Skalen sind dem Farbbalken neben der jeweiligen Grafik zu entnehmen. Die ◻ Abb. 2a stellt den Defokus für das phake Auge dar. Speziell Kombinationen aus hoher positiver Dezentrierung und hoher positiver Verkippung führen zu einem hohen Defokusfehler (bei 1,0 mm Dezentrierung und 10° Verkippung: 1,547 dpt). Maximal negative Werte traten für eine Dezentrierung von 0,0 mm und eine Verkippung von –10° auf (–0,293 dpt). Die ◻ Abb. 2b stellt den Astigmatismus in horizontale Richtung (0°/180°) dar. Hohe positive Dezentrierungen in Kombination mit hoher po-

Zusammenfassung · Abstract

Ophthalmologe 2021 · 118:828–837 https://doi.org/10.1007/s00347-020-01235-x

A. Langenbucher · P. Omidi · T. Eppig · N. Szentmáry · R. Menapace · P. Hoffmann

Kombination aus Dezentrierung und Verkippung der Linse im phaken und pseudophaken Auge – optische Simulation von Defokus, Astigmatismus und Coma

Zusammenfassung

Hintergrund und Zielsetzung. Der Einfluss von Dezentrierung und Verkippung von Kunstlinsen auf die Abbildungsqualität ist in den vergangenen Jahren ausgiebig in Simulationen wie auch klinischen Studien untersucht worden. Ziel dieser Arbeit ist es, den Einfluss der Dezentrierung und Verkippung auf die Induktion von Defokus, Astigmatismus und Coma im phaken und pseudophaken Auge zu untersuchen.
Methoden. Auf der Basis des Liou-Brennan-Modellauges wurde eine Simulation mit Zemax durchgeführt. Ausgehend von der im Augenmodell beschriebenen Position der Gradientenlinse, wurde nach der Bestimmung der Fokusebene die Linse von –1,0 bis 1,0 mm in Schritten von 0,2 mm horizontal dezentriert und von –10° bis 10° in Schritten von 2° um die vertikale Achse verkippt. Zu jeder der 121 Kombinationen wurde bei einer Pupille von 4 mm der Defokus, der reguläre Astigmatismus in 0/180° sowie die horizontale Coma aus der Wellenfront extrahiert. Analog zum phaken Auge wurde die Gradientenlinse durch ein aberrationskorrigierendes Kunstlinsenmodell ersetzt und die Simulation für das pseudophake Auge wiederholt.
Ergebnisse. Ist die Linse im phaken/pseudophaken Auge entsprechend den Vorgaben des Liou-Brennan-Modellauges positioniert, ergibt die Simulation einen Defokus von 0,026/–0,001 dpt, einen Astigmatismus von –0,045/–0,018 dpt sowie eine Coma von –0,015/0,047 µm. Maximale Werte treten bei einer Dezentrierung von 1,0 mm und einer Verkippung von 10° auf: 1,547/2,982 dpt für den Defokus, 0,971/1,871 dpt für den Astigmatismus sowie 0,441/1,209 µm für die Coma. Maximal negative Werte treten im phaken/pseudophaken Auge auf bei: –0,293/–1,224 dpt für den Defokus, –0,625/–0,663 dpt für den Astigmatismus sowie –0,491/–0,559 µm für die Coma.
Diskussion. In dieser Studie wurde erstmals der Effekt einer Kombination aus horizontaler Dezentrierung der Linse und Verkippung um die Vertikale auf den induzierten Defokus, Astigmatismus sowie die horizontale Coma in einem Simulationsmodell untersucht. Die Ergebnisse können bei der Ursachenforschung helfen, wenn bei dezentrierter oder verkippter Kunstlinse die Zielrefraktion nicht mit der erreichten Refraktion übereinstimmt oder der resultierende Astigmatismus durch den Hornhautastigmatismus alleine nicht erklärbar ist.

Schlüsselwörter

Intraokularlinse · Linsenausrichtung · Abbildungsqualität · Modellierung · Strahldurchrechnung

Combination of lens decentration and tilt in phakic and pseudophakic eyes—Optical simulation of defocus, astigmatism and coma

Abstract

Background and purpose. The effect of lens decentration and tilt on retinal image quality has been extensively studied in the past in simulations and clinical studies. The purpose of this study was to analyze the effect of combined lens decentration and tilt on the induction of defocus, astigmatism and coma in phakic and pseudophakic eyes.
Methods. Simulations were performed with Zemax on the Liou-Brennan schematic model eye. Based on the position of the gradient lens the image plane was determined (best focus). The lens was decentered horizontally from –1.0 mm to 1.0 mm in steps of 0.2 mm and tilted with respect to the vertical axis from –10° to 10° in steps of 2° (in total 121 combinations of decentration and tilt). For each combination of decentration and tilt defocus, astigmatism (in 0/180°) and horizontal coma was extracted from wave front error and recorded for a pupil size of 4 mm. After replacement of the gradient lens with an aberration correcting artificial lens implant model with the equatorial plane of the artificial lens aligned to the equatorial plane of the gradient lens, the simulations were repeated for the pseudophakic eye model.
Results. For the lens positioned according to the Liou-Brennan schematic model eye the simulation yielded a defocus of 0.026 dpt/–0.001 dpt, astigmatism of –0.045 dpt/–0.018 dpt, and a coma of –0.015 µm/0.047 µm for phakic/pseudophakic eyes. Maximum values were observed for a horizontal decentration of 1.0 mm and a tilt with respect to the vertical axis of 10° with 1.547 dpt/2.982 dpt for defocus, 0.971 dpt/1.871 dpt for astigmatism, and 0.441 µm/1.209 µm for coma. Maximum negative values occurred in phakic/pseudophakic eyes with –0.293 dpt/–1.224 dpt for defocus, for astigmatism –0.625 dpt/–0.663 dpt and for coma –0.491 µm /–0.559 µm, respectively.
Conclusion. In this simulation study the effect of a combination of lens decentration in horizontal direction and tilt with respect to the vertical axis on defocus, astigmatism and horizontal coma was analyzed. The results may help to describe in clinical routine if with a decentered or tilted artificial lens implant the postoperative refraction does not match the target refraction or the resulting astigmatism after cataract surgery is not fully explained by measurement of corneal astigmatism.

Keywords

Intraocular lens · Lens alignment · Image performance · Modelling · Raytracing

sitiver Verkippung führen zu einem starken Astigmatismus (bei 1,0 mm Dezentrierung und 10° Verkippung: 0,971 dpt). Maximal negative Werte traten für eine Dezentrierung von 0,8 mm und eine Verkippung von –10° auf (–0,625 dpt). Die ◘ **Abb. 2c** stellt die horizontale Coma in Falschfarbenkodierung dar. Die horizontale Coma ist besonders ausgeprägt bei Kombinationen aus deutlicher positiver Dezentrierung und Verkippung der Linse (Dezentrierung 1,0 mm und Verkippung 10°: 0,441 µm). Maximal negative Werte traten für eine Dezentrierung von –1,0 mm und eine Verkippung von –10° auf (–0,491 µm).

Die ◘ **Abb. 3** zeigt die Abhängigkeit der Zielgrößen Defokus, Astigmatismus

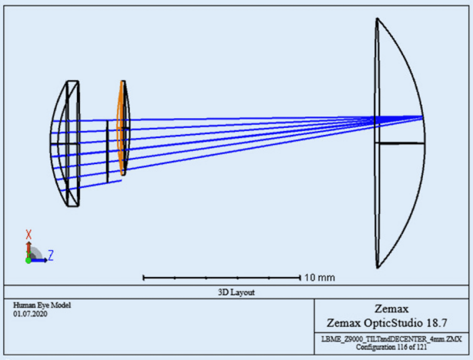

a

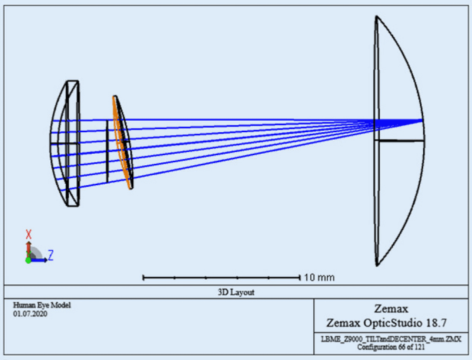

b

Abb. 1 ▲ **a** Schematisches Modellauge (rechtes Auge) von oben betrachtet. Die natürliche Linse wurde durch eine Kunstlinse ersetzt. Ausgehend von einer Positionierung, bei der die Haptikebene der Kunstlinse mit der Äquatorebene der Linse im Liou-Brennan-Modellauge übereinstimmt, wurde hier die Linse exemplarisch um +1,0 mm in horizontale Richtung dezentriert (positiver Wert meint eine Dezentrierung nach temporal). **b** Schematisches Modellauge (rechtes Auge) von oben betrachtet. Die natürliche Linse wurde durch eine Kunstlinse ersetzt. Ausgehend von einer Positionierung, bei der die Haptikebene der Kunstlinse mit der Äquatorebene der Linse im Liou-Brennan-Modellauge übereinstimmt, wurde hier die Linse exemplarisch um +10° um die vertikale Achse verkippt (positive Verkippung ist so definiert, dass die Linse in Richtung der normalen Sehachse, also nach nasal verkippt ist)

in 0/180° und horizontale Coma für verschiedene Kombinationen aus horizontaler Dezentrierung der Linse und Verkippung der Linse um die vertikale Achse für das pseudophake Augenmodell mit einer aberrationskorrigierenden Z9000-Kunstlinse. Aufgrund der Wahl der Bildebene nach dem „best focus" ist der Defokus ohne Dezentrierung und Verkippung (die Haptikebene der Kunstlinse stimmt mit der Äquatorebene der Gradientenlinse im phaken Augenmodell überein) sehr gering. Die zugehörigen Skalen sind dem Farbbalken neben der jeweiligen Grafik zu entnehmen. Die **Abb. 3a** stellt den Defokus im pseudophaken Auge dar. Speziell für eine große positive Dezentrierung und Verkippung der Kunstlinse wird ein deutlicher Defokus beobachtet (Dezentrierung von 1,0 mm und Verkippung von 10°: 2,982 dpt). Maximal negative Werte traten für eine Dezentrierung von 0,2 mm und eine Verkippung von −10° auf (−1,224 dpt). Die **Abb. 3b** stellt den Astigmatismus in 0°/180° für das pseudophake Auge dar. Speziell für eine große positive Dezentrierung und Verkippung der Kunstlinse wird ein deutlicher Astigmatismus beobachtet (Dezentrierung von 1,0 mm und Verkippung von 10°: 1,871 dpt). Maximal negative Werte traten für eine Dezentrierung von 0,0 mm und eine Verkippung von −10° auf (−0,663 dpt). Die **Abb. 3c** zeigt die horizontale Coma für das pseudophake Auge in Falschfarbenkodierung. Die horizontale Coma ist besonders ausgeprägt bei Kombinationen aus starker positiver Dezentrierung und Verkippung der Linse (Dezentrierung von 1,0 mm und Verkippung von 10°: 1,209 µm). Maximal negative Werte traten für eine Dezentrierung von −1,0 mm und eine Verkippung von −10° auf (−0,559 µm).

Die **Abb. 4** zeigt für das phake (**Abb. 4a**) und pseudophake (**Abb. 4b**) Auge exemplarisch für 9 der 121 ausgewählten Szenarien (Kombinationen aus Dezentrierung von 0,6/0,0/0,6 mm und Verkippung von −6/0/6°) die Punktbildverwaschungsfunktion („point spread function") in der Bildebene. Beide Abbildungen zeigen qualitativ, dass die Abbildungsfehler beim phaken wie auch beim pseudophaken Auge mit Ausnahme der Linsenpositionierung gemäß Liou-Brennan-Augenmodell (jeweils mittleres Bild) und der Kombination aus Dezentrierung von −0,6 mm und Verkippung von −6° durch die horizontale Coma dominiert werden, der Einfluss des Astigmatismus auf die Punktbildverwaschungsfunktion spielt hier eine untergeordnete Rolle.

Diskussion

Viele schematische Augenmodelle (z. B. Gullstrand, Kooijman, Lotmar etc.) vereinfachen das Auge als ein rotationssymmetrisches optisches System, bei dem sphärische oder asphärische optische Grenzflächen unterschiedliche Medien voneinander trennen [2]. Tatsächlich liegt beim menschlichen Auge aufgrund der exzentrischen Lage der Foveola keine Symmetrie in horizontale Richtung vor. Die Stelle des schärfsten Sehens weicht aus dem hinteren Pol nach temporal aus. Somit verläuft die Sehachse des Auges um etwa 4–7° in horizontale Richtung geneigt [2]. Diese Neigung der Sehachse relativ zur idealisierten optischen Achse wird als Winkel α bezeichnet. Hiervon unterscheidet sich der klinisch verwendete Winkel κ, der die

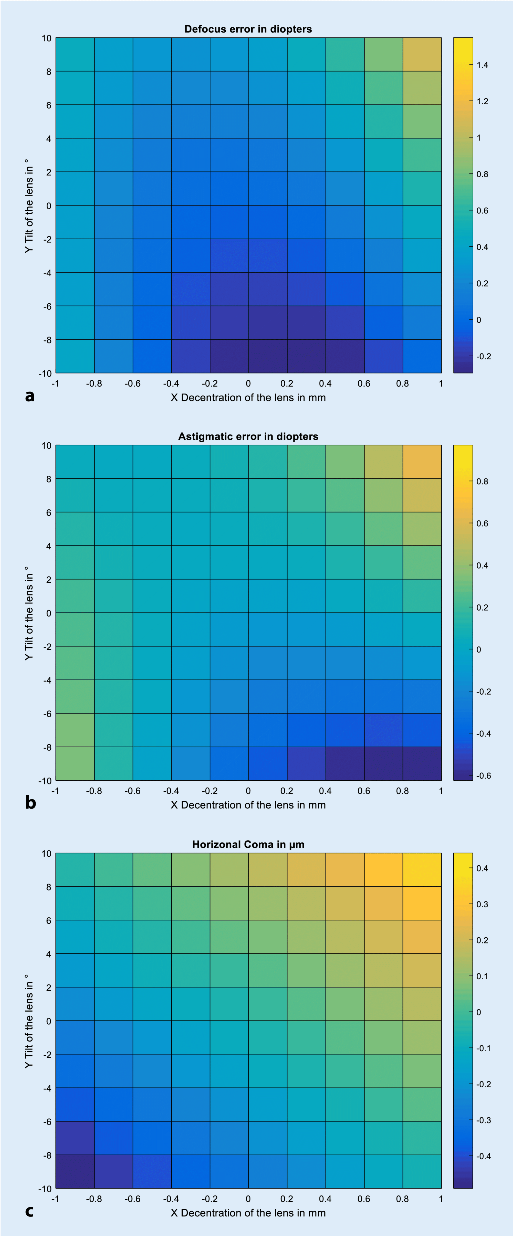

Abb. 2 ▲ **a** Defokus bei verschiedenen Kombinationen aus Dezentrierung (in horizontale Richtung) und Verkippung (um die vertikale Achse) der natürlichen Augenlinse im Liou-Brennan-Modellauge bei einer Pupille mit 4 mm Durchmesser. Die Bildebene wurde so gewählt, dass sie im phaken Auge ohne Dezentrierung und Verkippung im Fokus liegt. Die Farbskala gibt die Defokussierung in Dioptrien wieder. **b** Astigmatismus bei verschiedenen Kombinationen aus Dezentrierung (in horizontale Richtung) und Verkippung (um die vertikale Achse) der natürlichen Augenlinse im Liou-Brennan-Modellauge bei einer Pupille mit 4 mm Durchmesser. Die Farbskala gibt den Astigmatismus in 0°/180° in Dioptrien wieder, negative Werte entsprechen einem Astigmatismus in 90°. **c** Coma bei verschiedenen Kombinationen aus Dezentrierung (in horizontale Richtung) und Verkippung (um die vertikale Achse) der natürlichen Augenlinse im Liou-Brennan-Modellauge bei einer Pupille mit 4 mm Durchmesser. Die Farbskala gibt die horizontale Coma in Mikrometern in Dioptrien wieder

Neigung der Sehachse zur Pupillenachse (Lot auf der Hornhaut, welches das Pupillenzentrum schneidet) angibt und welcher deutlich geringer ausfällt als α. Aufgrund des schrägen Durchlaufs der Sehachse durch die optischen Medien trifft die Sehachse die Hornhaut und Linse nicht senkrecht oder zentriert [21]. Im Liou-Brennan-Modellauge ist dieser Verkippung der Sehachse dadurch Rechnung getragen, dass zwar die optischen Elemente Hornhaut und Augenlinse zentriert zur Symmetrieachse angeordnet sind, jedoch der Eingangsstrahl um 5° in der Horizontalen nach nasal verkippt ist [14].

Ein optisches System mit dezentrierten oder verkippten optischen Elementen weist Abbildungsfehler auf, die in zentrierten Systemen vernachlässigt werden können. Neben dem Astigmatismus schiefer Bündel tritt v. a. ein Coma-Fehler auf, der sich in der Bildebene durch eine Konfiguration vergleichbar einem Kometenschweif äußert. Zusätzlich verschiebt sich der Fokus in axiale Richtung, wodurch sich der Brechwert des optischen Systems verändert. In der Ophthalmologie wird oft unter einem Astigmatismus sowohl der reguläre Anteil, der mit einer zylindrischen Korrektur kompensiert werden kann, wie auch der irreguläre Anteil verstanden, der ausschließlich durch eine individuelle Wellenfrontkorrektur behoben werden kann.

In der vorliegenden Arbeit wurde ein Simulationsansatz gewählt, bei dem, ausgehend von einem modernen nicht zentrierten schematischen Augenmodell (Liou-Brennan [14]), eine Strahldurchrechnung erfolgte. Dabei wurde zunächst im phaken Modellauge die Bildebene („best focus“) ermittelt und anschließend die natürliche Linse (Gradientenlinse) in horizontale Richtung dezentriert und um die vertikale Achse verkippt. Insgesamt wurden jeweils für die Dezentrierung und Verkippung

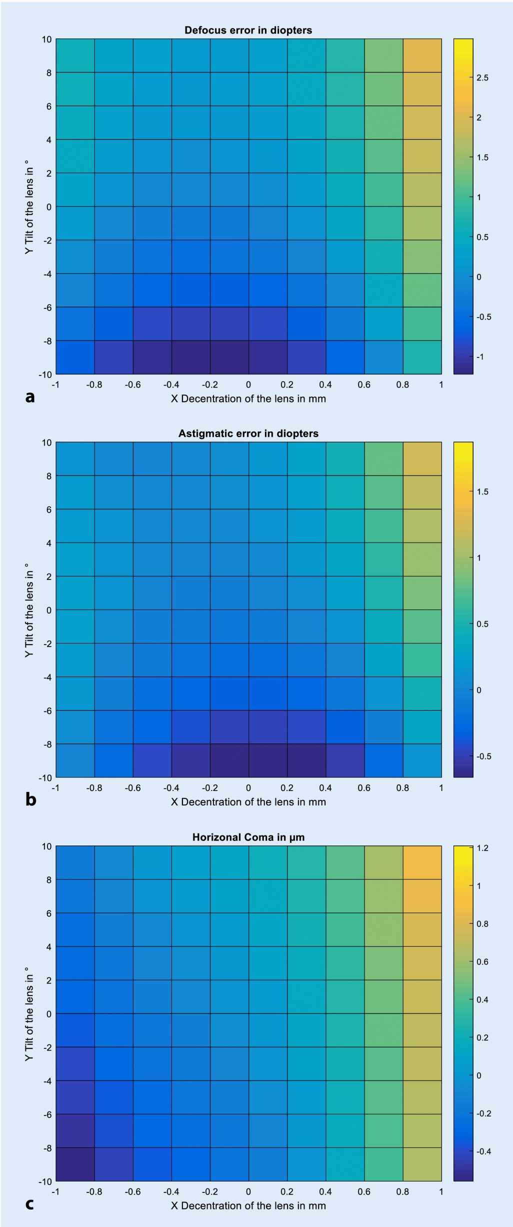

11 Szenarien durchgerechnet, sodass sich insgesamt in einem Bereich der Dezentrierung von −1,0 bis 1,0 mm und einem Bereich der Verkippung von −10 bis 10° 121 Kombinationen ergaben. Die Bildebene wurde dabei nicht verändert. Aus dem Wellenfrontfehler wurden der Defokusanteil, der Anteil des regulären durch eine zylindrische Korrektur kompensierbaren Astigmatismus (in 0/180°, in den schrägen Achsen ergibt sich bei unserem Ansatz ein Wert identisch 0) sowie die horizontale Coma (vertikale Coma ist aufgrund unseres Ansatzes identisch 0) extrahiert. In einem zweiten Schritt wurde die Gradientenlinse des Liou-Brennan-Augenmodells (stellvertretend für die natürliche Augenlinse) durch eine Kunstlinse ersetzt (Z9000, 21 dpt Brechwert, Designdaten aus der Patentschrift entnommen). Die Linse wurde zunächst so im pseudophaken Modellauge platziert, dass die Haptikebene der Kunstlinse mit der Äquatorebene der natürlichen Linse im phaken Modellauge übereinstimmt [6, 20]. Danach wurde die Bildebene justiert, um eine Abbildung im Fokus zu erreichen („best focus"). Anschließend wurde entsprechend dem Vorgehen beim phaken Modellauge die Kunstlinse im Bereich von −1,0 bis 1,0 mm dezentriert und im Bereich −10° bis 10° verkippt.

Aus den ◘ **Abb. 2a, b** sowie **3a, b** kann man direkt ablesen, dass die isolierte Betrachtung von Dezentrierung und Verkippung der Linse eine unrealistische Vereinfachung darstellt und die Kombination aus beidem ggf. die Beeinträchtigung der Abbildungsleistung verstärken oder auch abschwächen kann [4, 5, 15]. Beim phaken wie auch beim pseudophaken Auge verhalten sich der induzierte Defokus sowie der induzierte reguläre Astigmatismus grundsätzlich ähnlich: Für deutlich positive Werte für Dezentrierung und Verkippung treten jeweils der höchste positive Wert im

Abb. 3 ▲ **a** Defokus bei verschiedenen Kombinationen aus Dezentrierung (in horizontale Richtung) und Verkippung (um die vertikale Achse) der Kunstlinse (Z9000) als Ersatz der natürlichen Linse im Liou-Brennan-Modellauge bei einer Pupille mit 4 mm Durchmesser. Die Bildebene wurde so gewählt, dass sie beim pseudophaken Auge ohne Dezentrierung und Verkippung im Fokus liegt. Die Farbskala gibt die Defokussierung in Dioptrien wieder. **b** Astigmatismus bei verschiedenen Kombinationen aus Dezentrierung (in horizontale Richtung) und Verkippung (um die vertikale Achse) der Kunstlinse (Z9000) als Ersatz der natürlichen Linse im Liou-Brennan-Modellauge bei einer Pupille mit 4 mm Durchmesser. Die Farbskala gibt den Astigmatismus in 0°/180° in Dioptrien wieder, negative Werte entsprechen einem Astigmatismus in 90°. **c** Coma bei verschiedenen Kombinationen aus Dezentrierung (in horizontale Richtung) und Verkippung (um die vertikale Achse) der Kunstlinse (Z9000) als Ersatz der natürlichen Linse im Liou-Brennan-Modellauge bei einer Pupille mit 4 mm Durchmesser. Die Farbskala gibt die horizontale Coma in Mikrometern in Dioptrien wieder

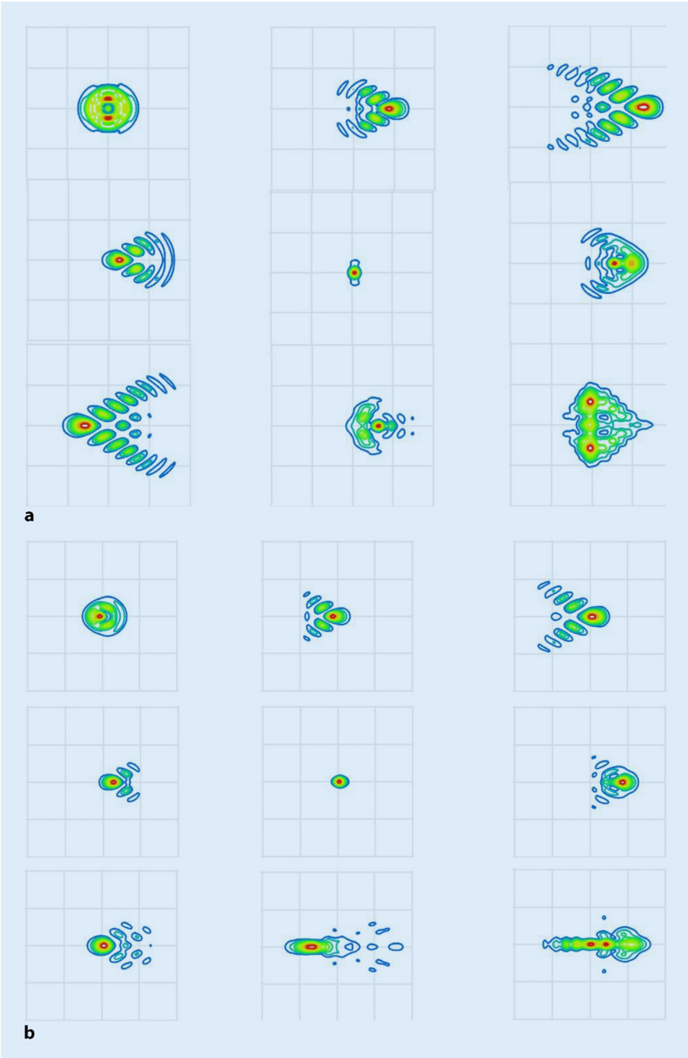

Abb. 4 ▲ **a** Punktbildverwaschungsfunktion („point spread function") in der Bildebene für 9 ausgewählte Szenarien der Kombination aus Dezentrierung (in horizontale Richtung) und Verkippung (um die vertikale Achse) der natürlichen Augenlinse im Liou-Brennan-Modellauge bei einer Pupille mit 4 mm Durchmesser. Die linke/mittlere/rechte Spalte entsprechen einer Dezentrierung von −0,6/0,0/0,6 mm, die obere/mittlere/untere Reihe einer Verkippung um 6/0/−6°. Jede Skalenunterteilung in horizontale und vertikale Richtung hat eine Abmessung von 10 µm in der Bildebene. **b** Punktbildverwaschungsfunktion („point spread function") in der Bildebene für 9 ausgewählte Szenarien der Kombination aus Dezentrierung (in horizontale Richtung) und Verkippung (um die vertikale Achse) der Kunstlinse (Z9000) als Ersatz der natürlichen Linse im Liou-Brennan-Modellauge bei einer Pupille mit 4 mm Durchmesser. Die linke/mittlere/rechte Spalte entsprechen einer Dezentrierung von −0,6/0,0/0,6 mm, die obere/mittlere/untere Reihe einer Verkippung um 6/0/−6°. Jede Skalenunterteilung in horizontale und vertikale Richtung hat eine Abmessung von 10 µm in der Bildebene

Defokus sowie der höchste positive Wert im regulären Astigmatismus auf (jeweils orangene Bereiche in den **Abb. 2a, b und 3a, b**). Beim phaken Auge können innerhalb des simulierten Parameterfensters der Dezentrierung/Verkippung rund 1,5 dpt an Defokus bzw. 1,0 dpt an Astigmatismus induziert werden. *Beim pseudophaken Auge liegen die entsprechenden Werte für den Defokus bei maximal 3,0 dpt bzw. für den regulären Astigmatismus bei maximal 1,9 dpt, also deutlich höhere Werte im Vergleich zum phaken Auge*. Das Ausmaß des induzierten Defokus, Astigmatismus sowie der Coma beim pseudophaken Auge hängt natürlich deutlich vom Design der Intraokularlinse ab, aus der Literatur ist bekannt, dass sphärische oder aberrationsneutrale Intraokularlinsen deutlich toleranter auf Dezentrierung und Verkippung reagieren als die hier exemplarisch gezeigte aberrationskorrigierende Linse mit einem hohen Korrekturgrad für die sphärische Aberration [4, 5]. Ein sehr viel milderer negativer Defokus sowie Astigmatismus werden dagegen induziert bei geringen Werten der Dezentrierung und deutlich negativen Werten für die Verkippung (blauer Bereich mittig unten in den **Abb. 2a, b** und **3a, b**. Für den Defokus bedeutet ein positiver Wert eine Myopisierung des Auges und ein negativer Wert eine Hyperopisierung des Auges. Für den Astigmatismus bedeuten positive Werte einen induzierten Astigmatismus in 0°, negative Werte dagegen einen Astigmatismus in 90°. Bei der horizontalen Coma ist die Charakteristik beim phaken und pseudophaken Auge unterschiedlich zu Defokus und Astigmatismus. Die Kombination aus starker positiver Dezentrierung und Verkippung liefert auch hier hohe positive Werte für die Coma (0,44 für das phake und 1,21 µm für das pseudophake Auge; orangene Bereiche in **Abb. 2c** und **3c**, rechts oben), jedoch liefert in der Berechnung die Kombination aus starker negativer Dezentrierung und Verkippung einen hohen Wert an negativer Coma von −0,49 µm für das phake und −0,56 µm für das pseudophake Auge (blaue Bereiche in **Abb. 2c** und **3c**, links unten). Zwischen der positiven Coma im Bild rechts oben und der nega-

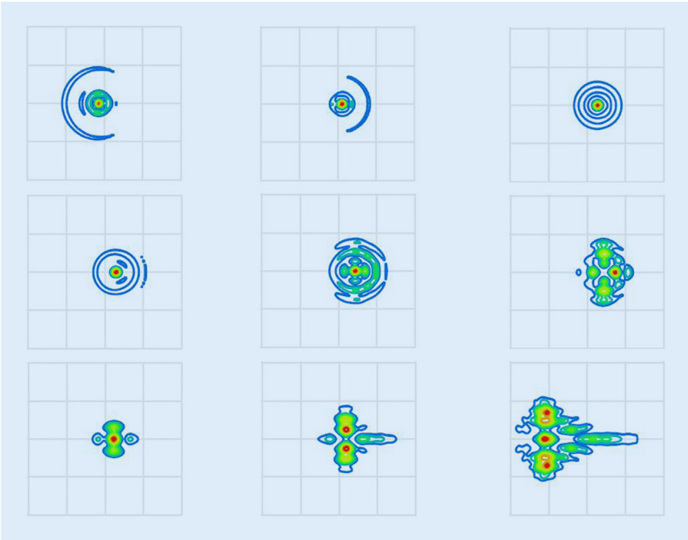

Abb. 5 ▲ Punktbildverwaschungsfunktion („point spread function") in der Bildebene für 9 ausgewählte Szenarien der Kombinatio aus Dezentrierung (in horizontale Richtung) und Verkippung (um die vertikale Achse) für eine sphärische equikonvexe Kunstlinse (hier wurden die gleichen Materialeigenschaften und der gleiche Brechwert von 21 dpt wie bei der Z9000 angenommen) als Ersatz der natürlichen Linse im Liou-Brennan-Modellauge bei einer Pupille mit 4 mm Durchmesser. Die linke/mittlere/rechte Spalte entsprechen einer Dezentrierung von −0,6/0,0/0,6 mm, die obere/mittlere/untere Reihe einer Verkippung um 6/0/−6°. Jede Skalenunterteilung in horizontale und vertikale Richtung hat eine Abmessung von 10 µm in der Bildebene

tiven Coma im Bild links unten besteht beim phaken Auge eine Symmetrie, beim pseudophaken Auge nicht.

Die Ergebnisse zeigen auf, dass sich die Abbildungsqualität im phaken wie auch im pseudophaken Auge bei Dezentrierung der Linse in horizontale Richtung und Verkippung um die vertikale Achse deutlich verschlechtert. In der vorliegenden Studie wurden ausschließlich horizontale Dezentrierungen und Verkippungen der Linse um die vertikale Achse berücksichtigt, im allgemeinen Fall können natürlich auch vertikale Dezentrierungen sowie Verkippungen um die horizontale Achse auftreten [13, 15]. Allerdings sind die Ergebnisse im allgemeinen Fall mit 4 Freiheitsgraden (jeweils 2 für Dezentrierung und Verkippung) nicht mehr intuitiv und grafisch nicht mehr geschlossen darzustellen oder interpretierbar. Die horizontale Richtung für die Dezentrierung und die Verkippung um die vertikale Achse wurden in dieser Arbeit ausgewählt, da das Auge in horizontale Richtung wegen der Verkippung der Sehachse ohnehin keine Symmetrie aufweist. Aus den Ergebnissen kann direkt abgelesen werden, dass bei der Kataraktoperation mit Implantation einer Kunstlinse immer dann, wenn die Kunstlinse sich mit ihrer Haptikebene dezentriert oder verkippt gegenüber der Äquatorebene der natürlichen Augenlinse im Auge positioniert, ein Refraktionsfehler zu erwarten ist. Dieser Refraktionsfehler äußert sich zum einen in einer Abweichung der erreichten Refraktion (sphärisches Äquivalent, hier dargestellt über den Defokus) von der Zielrefraktion, aber auch in der Induktion eines Astigmatismus, der durch den keratometrisch, topografisch oder tomografisch gemessenen Hornhautastigmatismus alleine nicht erklärbar ist. Sehr viel wichtiger ist jedoch, dass neben den korrigierbaren Refraktionsfehlern Defokus und Astigmatismus zusätzlich mit der Coma ein wesentlicher Abbildungsfehler auftritt, der mit klassischen Korrekturverfahren wie Brille oder Kontaktlinse nicht korrigierbar ist. Die **Abb. 4** zeigt, wenn auch nur für eine kleine Auswahl an 9 von 121 verschiedenen Szenarien für die Dezentrierung und Verkippung, welche Kombinationen im phaken Auge (**Abb. 4a**) und im pseudophaken Auge exemplarisch für die Kunstlinse des Typs Z9000 (**Abb. 4b**) mehr oder weniger von der Verschlechterung der Abbildungsqualität betroffen sind. So sieht man, dass das phake Liou-Brennan-Modellauge auch bei rotationssymmetrischen Hornhaut- und Linsengrenzflächen einen geringen Astigmatismus gegen die Regel (bei 90°) aufweist (**Abb. 4a** Mitte) und mit Ausnahme der Kombination aus Dezentrierung von −0,6 mm und 6° Verkippung (Bild links oben) die horizontale Coma die Abbildung dominiert. Ist das hier für die Simulation verwendete Kunstlinsenmodell (Z9000) perfekt nach der natürlichen Linse im Liou-Brennan-Augenmodell ausgerichtet, wird kein Astigmatismus beobachtet (**Abb. 4b** Mitte). Allerdings sind die anderen 8 Szenarien mit Dezentrierung und/oder Verkippung – auch die im Abschnitt vorher für das phake Auge hervorgehobene Kombination aus Dezentrierung von −0,6 mm und 6° Verkippung (Bild links oben) in abgeschwächter Form – durch die horizontale Coma in der Abbildung gekennzeichnet. Zum Vergleich wurden die entsprechenden Verhältnisse mit einer equikonvexen sphärischen Linse Kunstlinse untersucht. Die Linse wurde so modelliert, dass sie die gleichen Materialeigenschaften und den gleichen Brechwert (21 dpt) wie die vorher beschriebene Z9000 aufweist. Die **Abb. 5** zeigt die Punktbildverwaschungsfunktion an dieser sphärischen Linse. Bei einer Positionierung im Auge entsprechend der Vorgabe des Liou-Brennan-Modellauges (Dezentrierung und Verkippung jeweils 0, mittlere Grafik) weist das Auge eine deutliche sphärische Aberration auf, trotzdem sind etwa 80 % der Lichtenergie im zentralen Spot gebündelt. Der Spotdurchmesser ist hier mit etwa 16 µm deutlich größer im Vergleich zum phaken Auge oder dem pseudophaken Auge mit der Z9000, und die sphärische Aberration kommt auch in den anderen 8 Szenarien deutlich zum Tragen. Allerdings ist die horizontale Coma bei den

8 Szenarien mit Dezentrierung und/oder Verkippung ungleich 0 nicht so dominant im Vergleich zum pseudophaken Auge mit einer Z9000 (**Abb. 4b**).

Zum Schluss sei angemerkt, dass die hier verwendete Dezentrierung und Verkippung Extremwerte darstellen, die außerhalb der typischerweise gemessenen Werte liegen. Für die Dezentrierung von Kunstlinsen werden in der Literatur ein Mittelwert von ca. 0,3–0,4 mm angegeben sowie eine Dezentrierung von 3–5° [4], wobei hier zu beachten gilt, dass sich die Referenzachsen für die Angaben meist fundamental unterscheiden, sodass ein direkter Vergleich der einzelnen Studien nur schwer möglich ist. Legt man jedoch diese mittleren Werte als Messlatte zugrunde, so liegen die Werte für Defokus und Astigmatismus bei weniger 0,5 dpt und somit im Bereich der Zielgenauigkeit gängiger Berechnungsmethoden für Kunstlinsen. Somit können unvermeidbare Dezentrierung/Verkippung neben den Messunsicherheiten der Biometrie und der zulässigen Fertigungstoleranz für Kunstlinsen ursächlich sein für die Limitierung der Vorhersagegenauigkeit moderner Kataraktchirurgie.

Fazit für die Praxis

Dezentrierung und Verkippung können im phaken wie auch im pseudophaken Auge in Kombination auftreten und die Abbildungsqualität deutlich beeinträchtigen. Ausgehend von einem modernen schematischen Modellauge von Liou-Brennan, wurde hier in einer optischen Simulation gezeigt, welcher Defokus und Astigmatismus durch eine Dezentrierung in horizontale Richtung und Verkippung um die vertikale Achse auftreten und wie ggf. eine verringerte Abbildungsqualität oder ein Astigmatismus im phaken oder pseudophaken Auge zu erklären ist, der auf der Basis keratometrischer, topografischer oder tomografischer Messdaten nicht von der Hornhaut herrührt.

Korrespondenzadresse

Univ.-Prof. Dr. Achim Langenbucher
Institut für Experimentelle Ophthalmologie, Universität des Saarlandes
Kirrberger Str. 100, Gebäude 22, 66424 Homburg, Deutschland
achim.langenbucher@uks.eu

Funding. Open Access funding provided by Projekt DEAL.

Einhaltung ethischer Richtlinien

Interessenkonflikt. A. Langenbucher, P. Omidi, T. Eppig, N. Szentmáry, R. Menapace und P. Hoffmann geben an, dass kein Interessenkonflikt besteht.

Für diesen Beitrag wurden von den Autoren keine Studien an Menschen oder Tieren durchgeführt. Für die aufgeführten Studien gelten die jeweils dort angegebenen ethischen Richtlinien.

Literatur

1. Atchison DA, Suheimat M, Mathur A, Lister LJ, Rozema J (2016) Anterior corneal, posterior corneal, and lenticular contributions to ocular aberrations. Invest Ophthalmol Vis Sci 57(13):5263–5270
2. Atchison DA, Thibos LN (2016) Optical models of the human eye. Clin Exp Optom 99(2):99–106
3. Ben Yaish S, Zlotnik A, Raveh I, Yehezkel O, Belkin M, Zalevsky Z (2010) Intraocular omni-focal lens with increased tolerance to decentration and astigmatism. J Refract Surg 26(1):71–76
4. Eppig T, Scholz K, Löffler A, Messner A, Langenbucher A (2009) Effect of decentration and tilt on the image quality of aspheric intraocular lens designs in a model eye. J Cataract Refract Surg 35(6):1091–1100
5. Gillner M, Langenbucher A, Eppig T (2012) Untersuchung der theoretischen Abbildungsqualität asphärischer Intraokularlinsen bei Dezentrierung. Hoya AF-1 iMics1 und Zeiss ASPHINA(TM) (Invent ZO) [Investigation of the theoretical image quality of aspheric intraocular lenses by decentration. Hoya AF-1 iMics1 und Zeiss ASPHINA(TM) (Invent ZO). Ophthalmologe 109(3):263–270
6. Hu CY, Jian JH, Cheng YP, Hsu HK (2006) Analysis of crystalline lens position. J Cataract Refract Surg 32(4):599–603
7. Korynta J, Bok J, Cendelin J, Michalova K (1999) Computer modeling of visual impairment caused by intraocular lens misalignment. J Cataract Refract Surg 25(1):100–105
8. Korynta J, Bok J, Cendelin J (1994) Changes in refraction induced by change in intraocular lens position. J Refract Corneal Surg 10(5):556–564
9. Kozaki J, Takahashi F (1995) Theoretical analysis of image defocus with intraocular lens decentration. J Cataract Refract Surg 21(5):552–555
10. Kozaki J, Tanihara H, Yasuda A, Nagata M (1991) Tilt and decentration of the implanted posterior chamber intraocular lens. J Cataract Refract Surg 17(5):592–595
11. Langenbucher A, Reese S, Seitz B (2005) Impact of decentration of astigmatic intra-ocular lenses on the residual refraction after cataract surgery. Ophthalmic Physiol Opt 25(6):568–575
12. Langenbucher A, Viestenz A, Viestenz A, Brünner H, Seitz B (2006) Ray tracing through a schematic eye containing second-order (quadric) surfaces using 4 x 4 matrix notation. Ophthalmic Physiol Opt 26(2):180–188
13. Lawu T, Mukai K, Matsushima H, Senoo T (2019) Effects of decentration and tilt on the optical performance of 6 aspheric intraocular lens designs in a model eye. J Cataract Refract Surg 45(5):662–668
14. Liou HL, Brennan NA (1997) Anatomically accurate, finite model eye for optical modeling. J Opt Soc Am A Opt Image Sci Vis 14(8):1684–1695
15. Marcos S, Rosales P, Llorente L, Barbero S, Jiménez-Alfaro I (2008) Balance of corneal horizontal coma by internal optics in eyes with intraocular artificial lenses: evidence of a passive mechanism. Vision Res 48(1):70–79
16. Nishi Y, Hirnschall N, Crnej A, Gangwani V, Tabernero J, Artal P, Findl O (2010) Reproducibility of intraocular lens decentration and tilt measurement using a clinical Purkinje meter. J Cataract Refract Surg 36(9):1529–1535
17. Pérez-Merino P, Marcos S (2018) Effect of intraocular lens decentration on image quality tested in a custom model eye. J Cataract Refract Surg 44(7):889–896
18. Rong X, Miao A, Yu J, Du Y, He W, Lu Y, Zhu X (2019) Case series: slight Intraocular lens malpositioning as a potential cause of vision loss. Optom Vis Sci 96(10):802–807
19. Schröder S, Schrecker J, Daas L, Eppig T, Langenbucher A (2018) Impact of intraocular lens displacement on the fixation axis. J Opt Soc Am A Opt Image Sci Vis 35(4):561–566
20. Siedlecki D, Nowak J, Zajac M (2006) Placement of a crystalline lens and intraocular lens: retinal image quality. J Biomed Opt 11(5):54012. https://doi.org/10.1117/1.2358959
21. Wang X, Dong J, Wang X, Wu Q (2013) IOL tilt and decentration estimation from 3 dimensional reconstruction of OCT image. PLoS One 8(3):e59109. https://doi.org/10.1371/journal.pone.0059109
22. Wu M, Li H, Cheng W (1998) Determination of intraocular lens tilt and decentration using simple and rapid method. Yan Ke Xue Bao 14(1):13–16
23. Yu F, Chang P, Li J, Zhou Y, Zhao Y (2015) Comparative study of the tilt, decentration and

4.2 Paper 2

Title: Evaluation of optimal Zernike radial degree for representing corneal surfaces

Authors: Pooria Omidi, Alan Cayless, Achim Langenbucher

Publication date: 26/05/2022

Journal: Plos one (Public Library of Science)

Volume(Issues): 17(5)

Pages: e0269119

PLOS ONE

RESEARCH ARTICLE

Evaluation of optimal Zernike radial degree for representing corneal surfaces

Pooria Omidi[1]*, **Alan Cayless**[2], **Achim Langenbucher**[1]

1 Department of Experimental Ophthalmology, Saarland University, Homburg/Saar, Germany, **2** School of Physical Sciences, The Open University, Milton Keynes, United Kingdom

* Pooria.omidi@uks.eu

Abstract

Tomography data of the cornea usually contain useful information for ophthalmologists. Zernike polynomials are often used to characterize and interpret these data. One of the major challenges facing researchers is finding the appropriate number of Zernike polynomials to model measured data from corneas. It is undeniable that a higher number of coefficients reduces the fit error. However, utilizing too many coefficients consumes computational power and time and bears the risk of overfitting as a result of including unnecessary components. The main objective of the current study is to analyse the accuracy of corneal surface data modelled with Zernike polynomials of various degrees in order to estimate a reasonable number of coefficients. The process of fitting the Zernike polynomials to height data for corneal anterior and posterior surfaces is presented and results are shown for normal and pathological corneas. These results indicate that polynomials of a higher degree are required for fitting corneas of patients with corneal ectasia than for normal corneas.

OPEN ACCESS

Citation: Omidi P, Cayless A, Langenbucher A (2022) Evaluation of optimal Zernike radial degree for representing corneal surfaces. PLoS ONE 17(5): e0269119. https://doi.org/10.1371/journal.pone.0269119

Editor: Michael Mimouni, University of Toronto, CANADA

Received: October 8, 2021

Accepted: May 13, 2022

Published: May 26, 2022

Data Availability Statement: All relevant data are within the paper and its Supporting Information files.

Funding: The author(s) received no specific funding for this work.

Competing interests: The authors have declared that no competing interests exist.

Introduction

The cornea is one of the most influential optical components of the human eye, being responsible for about two-thirds of the eye's refractive power. The cornea is characterized by its anterior and posterior surfaces. Although the standard shape of the cornea is a prolate spheroid, there is a wide diversity of shapes in the human cornea. Corneal deformations are generally caused by corneal diseases such as keratoconus. Therefore, accurate evaluation and simulation of corneal surfaces are mandatory.

The shape measurement of the anterior and posterior surfaces of the cornea can be performed by non-destructive instruments such as optical coherence tomography devices. For the purpose of modelling the corneal surfaces, one can utilize Zernike polynomial expansion (named after Fritz Zernike, who proposed them in 1934 [1]). The first fundamental obstacle that arises in applying Zernike polynomials is to determine the appropriate number of terms. Vision researchers typically use the first 15 Zernike terms [2]. However, the question is how many Zernike terms are appropriate to describe the refractive properties of any cornea that has more aberration in its surfaces without any loss in profitable data [2, 3].

In this paper, we first describe our data acquisition system and mathematical method. Then we demonstrate the simulation outcomes on two different corneas, and present a statistical approach to 30 different eyes with diverse circumstances. Finally, we discuss our technique to determine the appropriate number of Zernike terms to describe corneal surface shape properly.

Materials and methods

Measurement setup

In order to measure corneal shape, we used a 3D swept-source OCT setup CASIA2 (TOMEY Inc., Nagoya, Japan). CASIA2 has an axial resolution of 10 μm with a scanning range of 16 mm in diameter and maximum penetration depth of 13 mm.

Data collection

For the present study, we used clinical records of patients who were admitted to the Saarland University Clinical Centre (Homburg, Germany). The study was registered at the local ethics committee of the Medical Association of Saarland (Ärztekammer des Saarlandes, 157/21).

A total of 15 normal volunteers and 15 patients were enrolled in the study. The volunteers show a normal corneal tomography, and the patients show corneal ectasia (keratoconus). These patients were in different stages of the Belin Ambrosio keratoconus severity classification (from 0 to 4). This study was carried out on native corneas without any history of eye surgery such as corneal cross-linking or intracorneal ring (segment) implantation.

Data selection

CASIA2 uses polar coordinates to provide several types of tomographic data such as elevation, refractive, keratometric, etc., from the anterior and posterior surfaces of the cornea.

The CASIA2 software provides raw data files in both CSV and DAT formats. Each data set has 16 meridians with 16 mm of diameter, with each meridian containing 800 data points. This study was restricted to the central 8 mm zone because this represents the average adult cornea diameter under the typical clinical conditions. It should be noted that CASIA2 considers a tangent plane to the centre of the anterior surface as a reference for measuring the height of each point.

All of the data selection procedure and data analysis was carried out using MATLAB R2019b software.

Zernike polynomials

Zernike polynomials are a set of orthogonal polynomials defined on a unit circle. These polynomials are a product of angular functions and radial polynomials [3]. Since CASIA2 obtains data in polar coordinates, it is advantageous to use polar Zernike functions instead of Cartesian functions because conversion from polar to Cartesian coordinates may affect the data as a result of internal corrections. The radial polynomials are formulated from the Jacobi polynomials and the angular functions are basic functions for the two-dimensional rotation group [4]. Commonly, vision researchers utilize two dimensional Zernike expansions in terms of radial and azimuthal parameters, introduced by Noll [5]. In the present study, Noll notation has not been used, hence the value of the radial polynomials has more priority for us.

The Zernike polynomials are defined as [5]

$$Z_p(\rho,\theta) = \begin{cases} \sqrt{2(n+1)}R_n^m(\rho)\cos(m\theta), \text{even}p, m \neq 0 \\ \sqrt{2(n+1)}R_n^m(\rho)\sin(m\theta), \text{odd}p, m \neq 0 \\ \sqrt{2(n+1)}R_n^0(\rho), m = 0 \end{cases}$$

Where n is the radial degree, m is the azimuthal frequency, and

$$R_n^m = \sum_{s=0}^{(n-m)/2} \frac{(-1)^s (n-s)!}{s!\left(\frac{n+m}{2}-s\right)!\left(\frac{n-m}{2}-s\right)!}\rho^{n-2s}.$$

The values of n and m are always integral satisfy $m \leq n$ and $n-|m|$ = even. The index ρ is a mode ordering number and is a function of n and m.

To reconstruct the surface from extracted Zernike terms, height data from corneal surface in polar coordinates can be modelled by a superposition of weighted Zernike polynomials [5].

$$h(\rho_d, \theta_d) = \sum_{p=1}^{P} a_p Z_p(\rho_d, \theta_d) + \varepsilon_d, d = 1, \ldots, D,$$

where $h(\rho_d, \theta_d)$ is corneal surface height, $Z_p(\rho_d, \theta_d)$ is the p-th Zernike polynomial sampled from $Z_p(\rho, \theta)$ at points (ρ_d, θ_d). Also ρ is normalized distance from the origin, θ is angle and ε is the deviation of modelled data from raw data.

Fitting Zernike polynomials

After clipping height data from the periphery (outside the 8 mm central region), we fitted normalized Zernike functions to the topographic shape of the cornea using a least squares regression method to find the best fit for a set of data points. The normalization factor of orthogonal Zernike functions is defined as:

$$N = \sqrt{\frac{(2-\delta_{m0})(n+1)}{\pi}}.$$

For continuous data points the integral of $(rZ(\rho, \theta))^2$ over the unit circle is unity. In this study, the data acquisition resolution is sufficient to consider the discrete data points as continuous and to neglect the mathematical error in the normalization factor.

Our goal is to find a reasonable balance between a low fit error (high number of Zernike polynomials) and avoidance of complexity of the surface (low number of Zernike polynomials).

To validate the method, a surface can be reconstructed with a limited number of calculated Zernike coefficients. The fit error is then calculated by subtracting the reconstructed height data from original height data.

This procedure is repeated each time by adding more coefficients and computing the root mean square of the fit error. For a better examination of the fit error behaviour, The RMS of the absolute value of fit error is plotted as a function of the number of fitted Zernike terms. This diagram (as shown in Fig 1) allows us to determine the reasonable number of Zernike coefficients which represents the refracting surfaces appropriately. In this diagram, vertical and horizontal lines are plotted as threshold indicators for Zernike radial degrees and RMS of the fit error value respectively.

The criterion for choosing the appropriate radial degree is based on the volume of changes in the fit error value by adding more Zernike terms. In other words, an appropriate radial degree is a degree at which adding more Zernike coefficients does not cause a considerable improvement in the fit performance.

The next step is to reconstruct each surface using the estimated radial degree. To calculate the difference between the reconstructed surface and the original one, reconstructed height data are subtracted from the original height data.

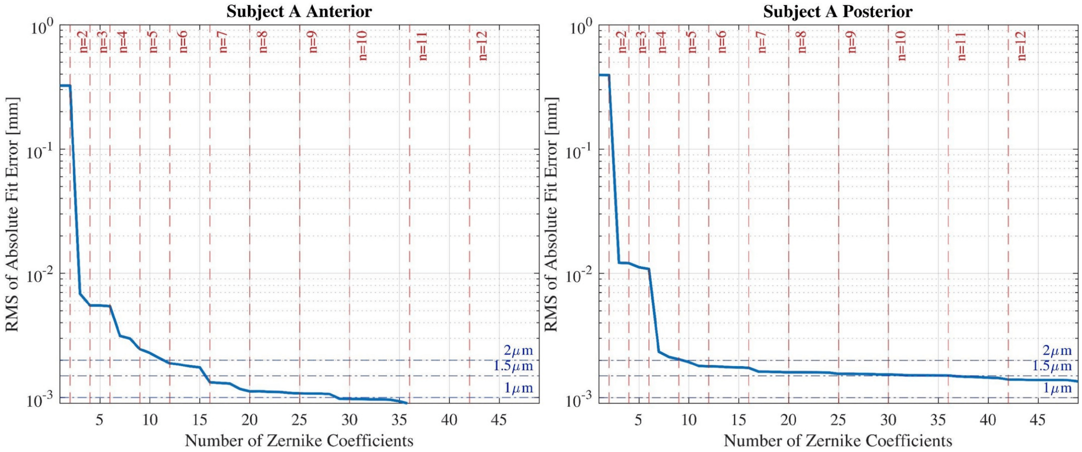

Fig 1. The results of fitting Zernike polynomials to corneal height for subject A. The horizontal dashed lines indicate the radial degree of fitted Zernike terms.

https://doi.org/10.1371/journal.pone.0269119.g001

To evaluate the performance of the composed height data in different radial zones, we have reconstructed the height data with the selected degree of coefficients at different radii and calculated the mean, median, and maximum from the absolute value of the fit error each time.

Results

This method was used to estimate the appropriate number of Zernike terms for corneal topography in 2 clinical examples. The first example uses eye measurement data from a normal subject (subject A). For the second example, a subject with mild keratoconus at the corneal surface was selected (subject B). For statistical analysis, the same procedure was then repeated for 15 normal corneas, and also for 15 corneas with various amount of corneal ectasia.

Fig 1 illustrates the RMS of the absolute value of fit error over the number of Zernike terms representing the height data of the anterior and posterior surfaces of subject A. Each radial degree of Zernike terms is denoted by dashed red vertical lines. The blue horizontal lines indicate the RMS value threshold.

From the graphs a radial degree of 7 is estimated for both anterior and posterior surfaces of subject A cornea. The reason for choosing this radial degree is that there is no significant decrease in RMS value with addition of more Zernike components. Each surface is reconstructed using the estimated radial degree. Fig 2 displays the residuals calculated at each coordinate point and displayed as a contour map.

Fig 3 shows the mean, median and maximum amounts of absolute value of fit error for variations of the central zone diameter for subject A.

The same procedure was repeated with corneal height data for subject B. Fig 4 illustrates the RMS of the absolute value of fit error over the number of fitted Zernike terms on subject B corneal surfaces.

From the results, radial degrees of 7 and 9 were selected for the anterior and posterior surfaces. Fig 5 displays the residuals at each point of coordinates for subject B.

Finally, Fig 6 shows the mean, median and maximum absolute value of the fit error for variations of the central zone diameter for subject B.

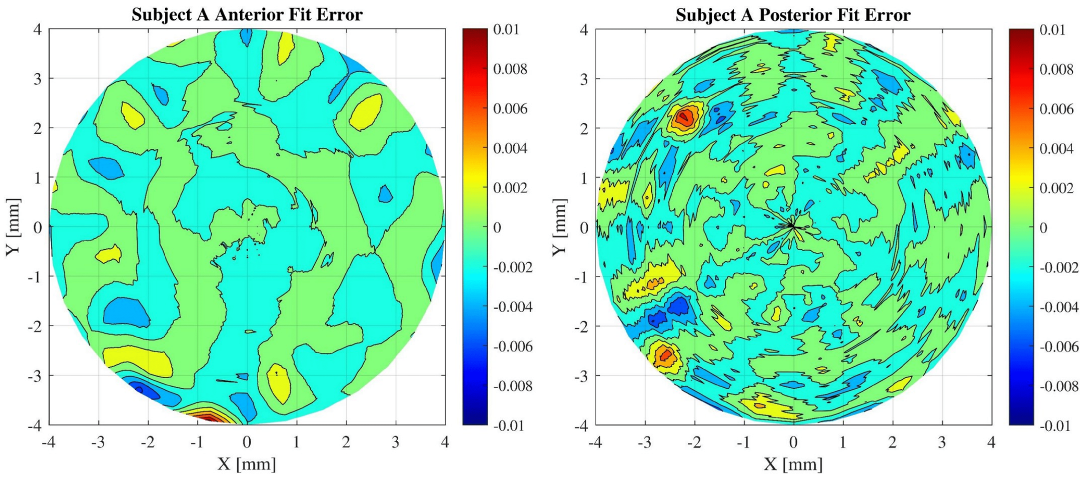

Fig 2. Error values of the fitted corneal surfaces. Both reconstructed anterior and posterior surfaces modelled with Zernike radial degree of 7.

https://doi.org/10.1371/journal.pone.0269119.g002

The strategy of OCT data processing was used to analyse 30 subjects with a variety of corneal conditions. The results are presented in the next subsection.

Evaluation of a series of normal and patients

In this subsection, we present the results of our method as tested on 15 normal and 15 patients with various amount of corneal ectasia. Table 1 provides information on the normal subjects and the radial degrees required for modelling the anterior and posterior surfaces of their corneas. Appropriate radial degree for anterior surface denoted by n_A and for posterior surface denoted by n_P.

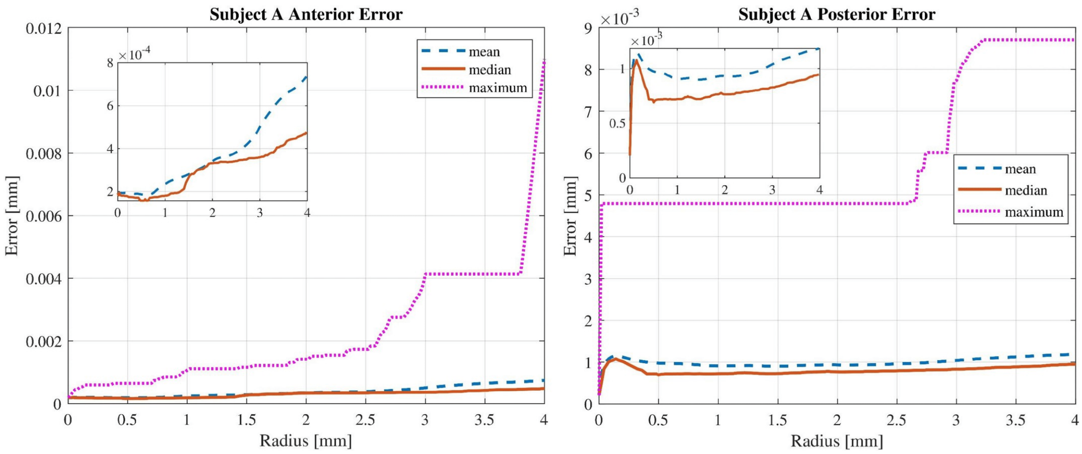

Fig 3. Error analysis for anterior and posterior surfaces modelled with radial degree of 7. Mean, median and maximum values are denoted by dashed, solid, and doted lines.

https://doi.org/10.1371/journal.pone.0269119.g003

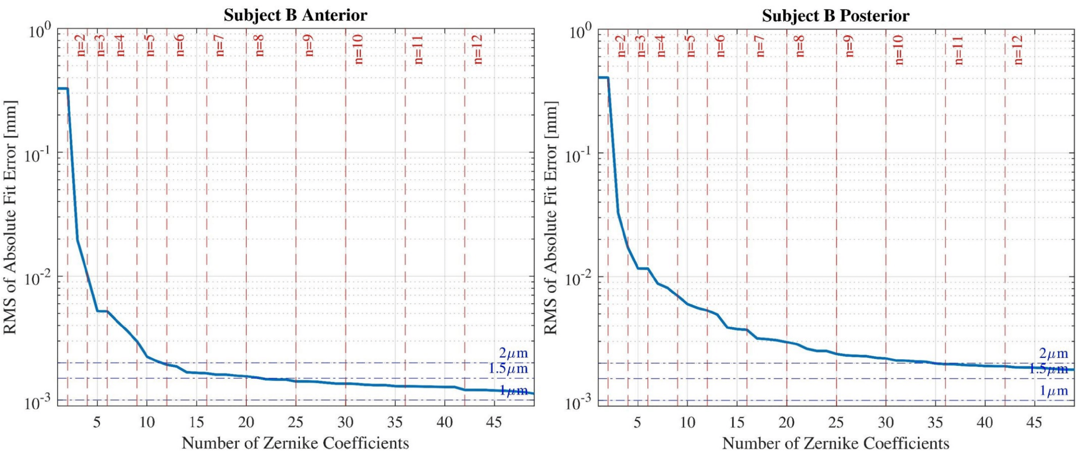

Fig 4. The results of fitting Zernike polynomials to corneal height for subject B. The horizontal dashed lines indicate the radial degree of fitted Zernike terms.

https://doi.org/10.1371/journal.pone.0269119.g004

Similarly, Table 2 provides information on the keratoconus subjects and the radial degrees required for modelling the anterior and posterior surfaces of their corneas.

Discussion

From Figs 1 and 4 it can be concluded that fitting more Zernike polynomials to the height data of cornea decreases the fit error, up to a certain point. After this point there is no significant change in the fit error value with increasing number of fitted Zernike terms and the slope of the changes gradually tends to zero. Therefore potential overfitting may cause the addition of

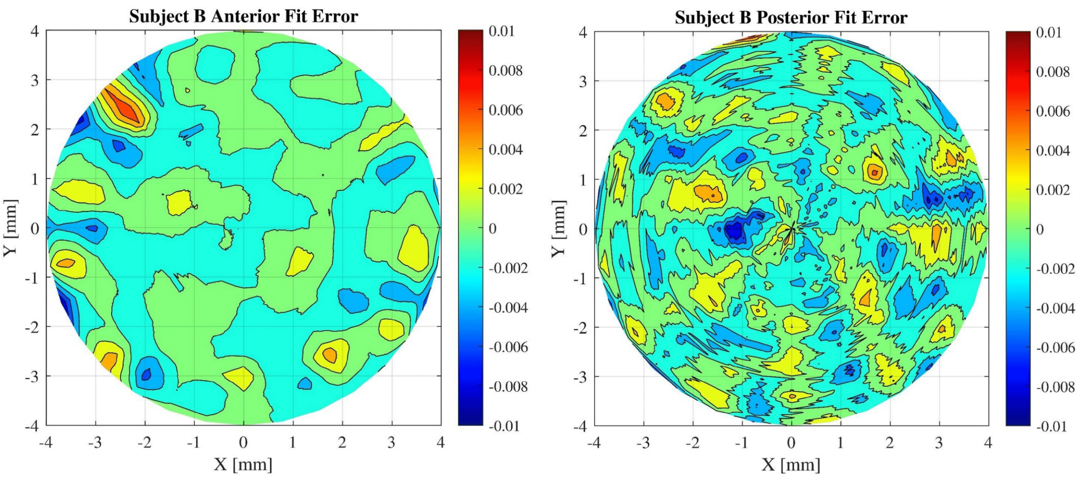

Fig 5. Error values of the fitted corneal surfaces. Reconstructed anterior and posterior surfaces modelled with Zernike radial degree of 7 and 9 respectively.

https://doi.org/10.1371/journal.pone.0269119.g005

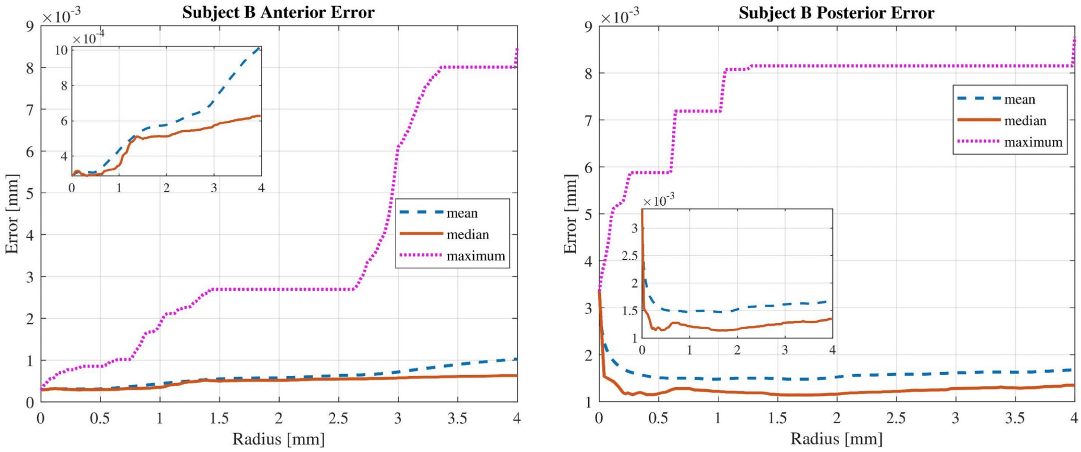

Fig 6. Error analysis for anterior and posterior surfaces modelled with radial degree of 7 and 9 respectively. Mean, median and maximum values are denoted by dashed, solid, and doted lines.

https://doi.org/10.1371/journal.pone.0269119.g006

more measurement noise to the modelled surface. For that reason there should be a balance between accuracy and noise elimination criteria of the modelled surface.

Another result that can be observed from the figures is that the amount of fluctuation of the surface height in the posterior surface is greater than that for the anterior surface of the cornea. This behaviour can be observed in OCT devices, where the amount of white noise increases when deeper structures are measured [6]. Since the optical path difference between the sample and the reference mirror in deeper layers increases, this leads to decrease of contrast. As a result, it can be deduced from Figs 2 and 5 that the posterior surface shows more error fluctuation in its topographic shape and the fit error value of the posterior surface is higher in comparison to the anterior surface.

By analysing the results, it can be concluded that simulated surfaces with finite Zernike polynomials have more similarity in the centre rather than in the periphery. Moreover, the absolute value of fit error increases with increasing zone diameter. It means that the fitting quality has a radial behaviour. This phenomenon can be explained from two perspectives. First, the sparse sampling in the periphery and the denser sampling in the centre. Second, signal to noise ratio decreases if the OCT beam meets the surface more obliquely in the periphery of the cornea.

As expected, the radial degree required for modelling corneas in patients with corneal ectasia is more than for normal corneas. The results in Tables 1 and 2 support this hypothesis.

Limitations of this study

Our sample did not include eyes with history of corneal surgery and there are only two groups of normal and keratoconic eyes. So it can be concluded that there is a lack of generality in the samples.

This study has the character of a pilot study and our aim was to show the applicability of this concept rather than to study the difference between normal and keratoconic corneas. Therefore, we did not perform a power analysis and the number of samples is limited.

Table 1. Appropriate radial degree of fitted Zernike polynomials for normal subjects.

Subject	Age	Sex	OD/OS	n_A	n_P
1	53	Female	OD	7	8
2	30	Female	OS	7	7
3	26	Female	OD	6	8
4	27	Male	OS	6	7
5	27	Male	OD	7	7
6	22	Male	OD	6	7
7	29	Male	OD	7	7
8	28	Female	OD	7	8
9	28	Female	OS	6	7
10	72	Male	OD	5	7
11	45	Female	OS	6	7
12	27	Male	OD	7	7
13	71	Male	OD	7	8
14	35	Female	OD	5	6
15	53	Female	OS	7	7

https://doi.org/10.1371/journal.pone.0269119.t001

Table 2. Appropriate radial degree of fitted Zernike polynomials for keratoconus subjects.

Subject	Age	Sex	OD/OS	n_A	n_P	Classification stage
1	61	Female	OS	7	9	1
2	25	Male	OD	7	9	1
3	42	Male	OS	8	8	2
4	42	Male	OD	7	8	1
5	33	Male	OD	7	9	1
6	28	Male	OD	6	8	1
7	64	Male	OS	8	10	3
8	64	Male	OD	9	11	3
9	14	Female	OD	8	9	2
10	63	Female	OS	7	9	2
11	45	Female	OD	8	8	2
12	80	Female	OD	7	8	1
13	59	Male	OS	9	9	3
14	53	Male	OS	8	8	2
15	18	Male	OS	8	9	2

https://doi.org/10.1371/journal.pone.0269119.t002

Supporting information

S1 Data.
(XLSX)

S2 Data.
(XLSX)

Author Contributions

Formal analysis: Pooria Omidi, Achim Langenbucher.

Methodology: Pooria Omidi.

Project administration: Achim Langenbucher.

Software: Pooria Omidi.

Supervision: Achim Langenbucher.

Validation: Alan Cayless, Achim Langenbucher.

Visualization: Pooria Omidi.

Writing – original draft: Pooria Omidi.

Writing – review & editing: Alan Cayless.

References

1. Zernike F. Diffraction theory of the knife-edge test and its improved form: the phase-contrast method. Monthly Notices of the Royal Astronomical Society. 1934; 94: 377–384.
2. Iskander DR, Collins MJ, Davis B. Optimal modelling of corneal surfaces with Zernike polynomials. IEEE Transactions on biomedical engineering. 2001; 48(1): 87–95. https://doi.org/10.1109/10.900255 PMID: 11235595
3. Schwiegerling J, Greivenkamp JE. Using corneal height maps and polynomial decomposition to determine corneal aberrations. Optometry and vision science: official publication of the American Academy of Optometry. 1997; 74(11): 906–916. https://doi.org/10.1097/00006324-199711000-00024 PMID: 9403887
4. Szeg G, Orthogonal polynomials. Vol 23. American Mathematical Soc.; 1939.
5. Noll RJ, Zernike polynomials and atmospheric turbulence. JOsA. 1976; 66(3): 207–211.
6. Fercher AF, Drexler W, Hizzenberger CK, Lasser T. Optical coherence tomography-principles and applications. Reports on progress in physics. 2003; 66(2): 293.

4.3 Paper 3

Title: Simulation of photic effects after cataract surgery for off-axis light sources

Authors: Pooria Omidi, Alan Cayless, Achim Langenbucher

Publication date: 20/01/2022

Journal: Plos one (Public Library of Science)

Volume(Issues): 17(1)

Pages: e0262457

PLOS ONE

RESEARCH ARTICLE

Simulation of photic effects after cataract surgery for off-axis light sources

Pooria Omidi[1]*, Alan Cayless[2], Achim Langenbucher[1]

1 Department of Experimental Ophthalmology, Saarland University, Homburg, Saarland, Germany, **2** School of Physical Sciences, The Open University, Milton Keynes, United Kingdom

* Pooria.omidi@uks.eu

Check for updates

Abstract

Photopsia is a phenomenon that sometimes disturbs patients after cataract surgery. To evaluate the impact of the edge design of intraocular lenses (IOL) on the location, shape and relative intensity of photic effects at the retina caused by photopsia in pseudophakic eyes, photopsia was simulated using ZEMAX software. The structural parameters of the pseudophakic eye model are based on the Liou-Brennan eye model parameters with a pupil diameter of 4.5 mm. The IOLs implanted in the eye model have a power of 21 diopter (D) with optical diameter of 6 mm and 7 mm. From the ray-tracing analysis, covering variations of incident ray angle of 50˚ to 90˚ from temporally, a photic image is detected at the fovea at specific ray angles of 77.5˚ (6 mm IOL) and 78.2˚ (7 mm IOL). This photic image disappears when a thin IOL with an edge thickness of 0 mm or a thick IOL with absorbing edges is replaced in the eye model. With an anti-reflective edge, this photic image remains, but with a fully reflecting edge it disappears at the critical angles and appears with different shapes at other angles. The intensity of this photic image can be reduced by changing the edge design to a frosted surface. Most of the photic patterns in IOLs are not observed with absorbing and thin edge designs. IOLs with anti-reflecting and fully reflecting edges generate disturbing photic effects at different angles on the fovea. IOLs with frosted edges reduce the contrast of the photic effects and make them less disturbing for patients.

OPEN ACCESS

Citation: Omidi P, Cayless A, Langenbucher A (2022) Simulation of photic effects after cataract surgery for off-axis light sources. PLoS ONE 17(1): e0262457. https://doi.org/10.1371/journal.pone.0262457

Editor: Michael Mimouni, University of Toronto, CANADA

Received: September 6, 2021

Accepted: December 23, 2021

Published: January 20, 2022

Data Availability Statement: Relevant simulation data are within the manuscript and its Supporting Information files. All Data are available from the Institute of Experimental Ophthalmology Institutional Data Access for researchers who meet the criteria for access to confidential data.

Funding: J.S. was supported in part by the Rolf M. Schwiete Stiftung under project nr. 11/2018. (https://schwiete-stiftung.com/). The funders had not and will not have a role in study design, data collection and analysis, decision to publish, or preparation of the manuscript.

Introduction

Photopsia is an optical phenomenon defined by the presence of effects in the visual field which are not directly correlated to imaging of an object. In photopsia light is detected at a location where no light is expected.

This phenomenon sometimes occurs in a time period shortly after intraocular lens implantation. In the literature it is shown that this effect could be associated with the position and optical design of IOLs, as first reported by Masket et al. [1] The effect has been named *dysphotopsia* by Tester et al. [2].

Several explanations, such as: IOL material with a high index refractive index [3–5], optics with sharp or truncated edges [3–5], defects in the IOL optics during manufacturing, central optical defects during folding and injection, a cataract incision located temporally in the clear cornea [6], a prominent globe [7], a shallow orbit [7], neural adaptation [8], and reflection of

Competing interests: We have no conflicts of interest to disclose.

the anterior capsulotomy edge projected onto the nasal peripheral retina for photopsia, have been discussed as effect sizes [9]. Holladay et al. determined the impact of the edge design as the cause of this phenomenon using a ZEMAX program simulation [10, 11].

Photopsia cannot be measured or quantified objectively and there is no clinical test to prove or verify these phenomena. However, in rare cases, it can be detected with a 90˚ visual field measurement. Generally, following cataract surgery, patients are either free of these photic side effects or the effects are below perceptible levels. A few cases who encounter these symptoms can tolerate them and not feel disturbed [3, 12]. Some patients report symptoms with the help of drawings originated from photopsia.

In photopsia light is perceived as bright patterns such as arcs [10], streaks [13], rings or halos [14] which become visible on the central or mid peripheral visual field without correlation to illumination. In contrast, in some cases, this phenomenon causes a gap in the homogeneous lighting of the retina that appears as a crescent, sickle, arc, or ring shadows [3].

Clinical studies show that photopsia always appears shortly after cataract surgery, that the photic effects are mostly located in the temporal visual field, and that they can be made to disappear with the use of ocular blinkers. Moreover, there is no systematic correlation between photopsia and corneal diameter, anterior chamber depth, iris pigmentation, and photopic and scotopic pupil diameter or refraction [6, 14].

Methods

This study was registered at the local ethics committee of the Medical Association of Saarland (Ärztekammer des Saarlandes, 157/21).

Eye model specifications

The pseudophakic eye model used for optical simulations in this study is based on the Liou-Brennan schematic model eye introduced in 1997 [15]. The cornea of this model is defined by two aspheric refracting surfaces with a thickness of 0.5 mm. These two rotationally symmetric surfaces (front and back surface) are described by a radius of 7.77 and 6.40 mm, an asphericity of -0.18 and -0.60, and a refractive index of 1.376 respectively. Other parameters of this model are as follows: internal ACD, 3.79 mm; decentration of the pupil nasally, 0.5 mm; distance between pupil and IOL, 0.63 mm; total axial length, 23.95 mm. The model is centred on the optical axis and therefore, the retinal surface is symmetrical about the optical axis. Moreover, the pupil diameter used in this model is 4.5 mm.

Fig 1 illustrates a schematic sketch of the eye model used in this study. Each surface is labelled with a number from 1 to 6.

The IOLs in this model are acrylic hydrophilic with refractive power of 21 dpt and refractive index of 1.458, an edge thickness of 0.3 mm and a sharp circular optic edge. The front surface of the IOLs defined by a spherical surface, but the back surface is an aspherical surface optimised for 0.26 μm spherical aberration in the total eye model. The optical diameters of the IOLs were 6 mm and 7 mm, respectively. The lenses were positioned with the equator aligned to the equator of the crystalline lens in the model eye. Table 1 lists all relevant parameters of the proposed pseudophakic model eye and the polynomial coefficients that describe the rotationally symmetric aspheric surface of the IOL. Note that polynomial coefficient values not mentioned in the table equal zero.

Ray tracing procedure

Ray tracing was performed with the ZEMAX professional ray tracing software (Version 19.8, Washington, USA) using the non-sequential ray tracing mode to study the photopsia. For this simulation, an extended light source with a diameter of 6 mm was used.

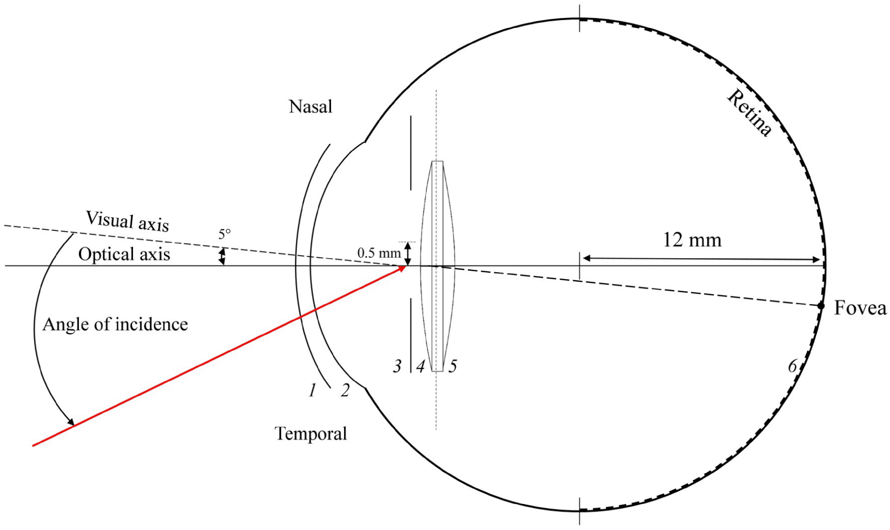

Fig 1. Schematic drawing of the pseudophakic eye. (See Table 1 for parameter values).

https://doi.org/10.1371/journal.pone.0262457.g001

To identify the position of the fovea on the retinal surface, rays are traced through the pupil with a physiological entrance angle slanted by 5° with respect to the optical axis in the nasal direction. The retina is modelled as a half-sphere with a radius of 12 mm.

A collimated light pencil made up of 1 million rays from the extended source in the visible range is used to analyse the photopsia. Rays from 50 to 90 degrees in steps of 5° with respect to the optical axis are traced temporally through the pupil to evaluate the intensity distribution on the retinal surface.

At some specific angles between 50° to 90°, arc-shaped ghost images in the foveal region were noticed. For these specific angles further simulations were performed.

By simulating a thick absorbing IOL edge, light transmission through and reflection off the edge is suppressed. With thick specular reflecting and anti-reflecting IOL edges, the effects of internal specular reflection and transmission are highlighted respectively. With a thick scattering IOL edge, the effect of 'frosting' is resampled and the transmitted light is scattered, as is the internally reflected light. The Lambertian scattering model is used to define the frosted edge surface in this IOL type. To avoid complexity, an isotropic scattering model was applied, in

Table 1. Structural parameters of the pseudophakic eye model.

Surface	Radius[mm]	Asphericity	Thickness[mm]	Optical diameter[mm]
1	7.77	-0.18	0.5	14
2	6.40	-0.6	3.16	14
3	∞	-	0.63	4.5
4	13.86	-	0.97	6 and 7
5	-11.66	-1.5	18.69	6 and 7
6	-12	-	-	24
Surface	α_2[mm^{-1}]	α_4[mm^{-3}]	α_6[mm^{-5}]	α_8[mm^{-7}]
5	-6.34e^{-3}	1.15e^{-3}	-3.86e^{-7}	-2.47e^{-8}

https://doi.org/10.1371/journal.pone.0262457.t001

which the scattered ray projection vector has an equal probability for all directions in the space. Lambertian scattering is independent of the incident ray angle and each point on the surface was treated as a point source.

In contrast, with the thin optics edge no light transmission or internal light reflection occurs at the edge. These settings enabled the impact of transmission, reflection or scattering of the optical edge on the intensity distribution in the retina to be studied.

In summary, to evaluate the contribution of the IOL edges on photopsia, IOLs were simulated with thin edges (0.0 mm instead of 0.3 mm), and additionally with absorbing, fully reflecting, anti-reflecting, and scattering edges (0.3 mm edge).

Results

Fig 2 shows the simulation results from the foveal position on the retinal surface when the entrance angle is 0° with respect to the visual axis. The simulation results show that the foveal position is not located at the geometrical axis. It is shifted 1.462 mm towards temporally.

Fig 3 shows the light intensity profile on the retina for the IOL types (6 mm and 7 mm optics) for variations of incident ray angle of 50° to 90° temporally in steps of 5°.

Within this variation of the incident ray angle, we note a specific incident ray angle of 77.5° (6 mm optics) and 78.2° (7 mm optics) where an arc-shaped photic image is located at the fovea.

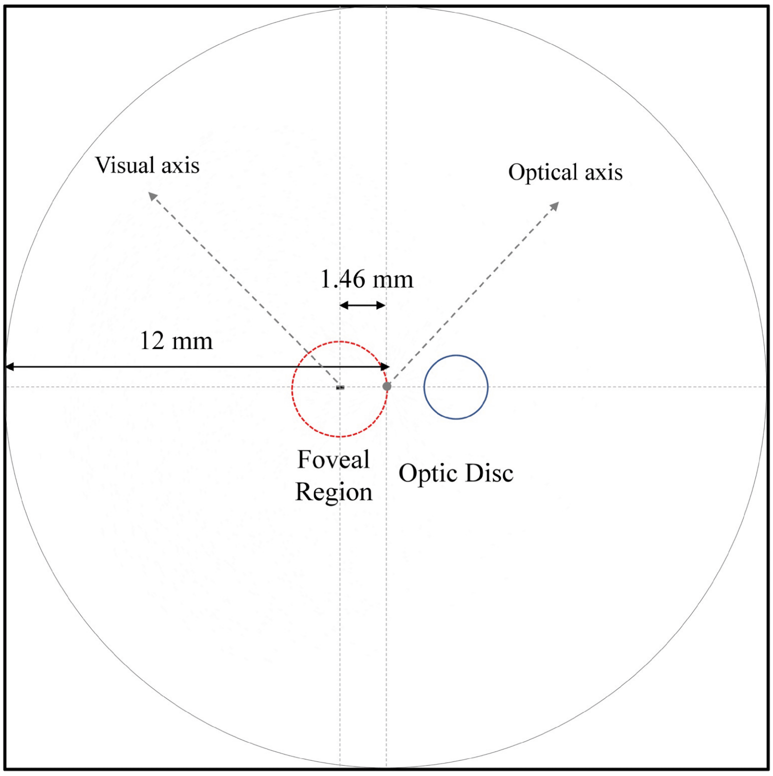

Fig 2. Fovea and optic disc positions on the retinal surface.

https://doi.org/10.1371/journal.pone.0262457.g002

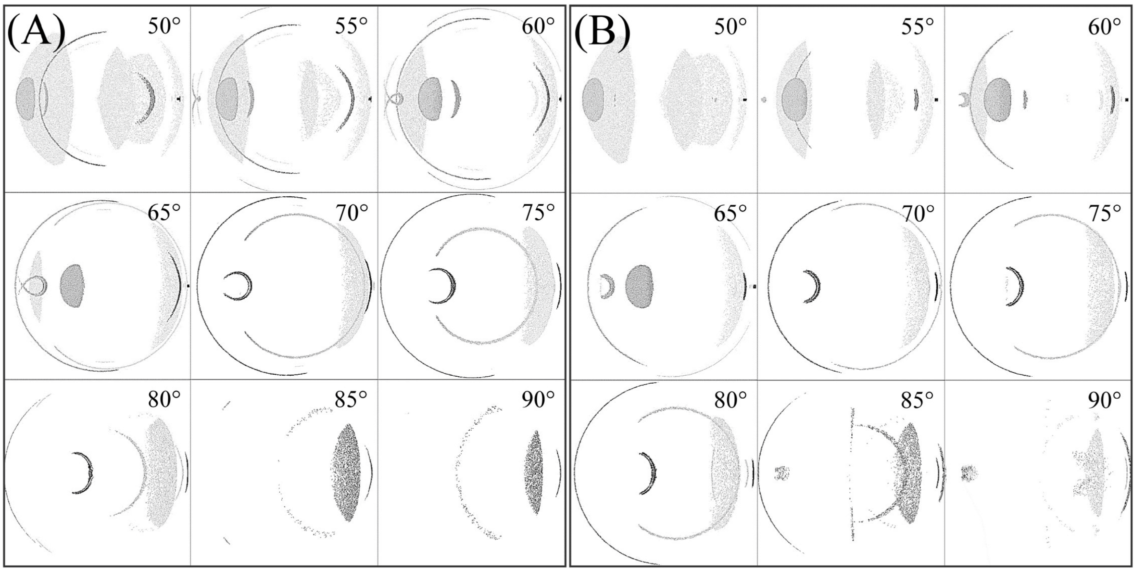

Fig 3. Intensity distribution on the retina for variation of incident ray angle of 50˚ to 90˚. (A) For IOL with 6 mm optics diameter. (B) For IOL with 7 mm optics diameter.

https://doi.org/10.1371/journal.pone.0262457.g003

Fig 4 shows the light intensity distribution at these specific angles. Note that in Figs 3–9, section (A) refers to the 6 mm optic diameter with incidence angle of 78.2˚ and section (B) refers to the 7 mm optic diameter with incidence angle of 77.5˚. Moreover, the red circle with a dashed line illustrates the foveal region and the smaller circle with a solid line illustrates the optic disc.

In a further analysis we analysed how the different edge conditions affect the properties of this photic phenomenon. Fig 5 illustrates the intensity distribution at the retina for IOLs with absorbing edges.

By changing the edge type between anti-reflective and fully reflective surfaces, photic patterns generated by transmission or reflection of light from the edges can be classified independently. Anti-reflective edges remove the photic patterns that arise from internal reflection at the edges. On the other hand, fully reflective edges increase the intensity of the photic patterns caused by internal reflection while eliminating light passing through the edges. Figs 6 and 7 show the intensity distribution in situations where the edges are fully reflective and anti-reflective respectively.

Fig 8 illustrates the intensity distribution at the retina with a frosted IOL optics edge design.

In the final ray tracing simulation, the contribution of edge thickness on different photic patterns is analysed. Fig 9 illustrates the retinal image using a thin edge design (0 instead of 0.3 mm) which fully avoids edge effects such as transmission or internal reflections.

Fig 10 illustrates a schematic view of the thick and thin IOLs in this study. In 10A the colored part shows the edge surface is and in 10B edge thickness is zero.

Discussion

From Fig 3 it is observed that with increasing incident ray angle photic patterns initially located far nasally move to the central part of the retina and change their shape and intensity.

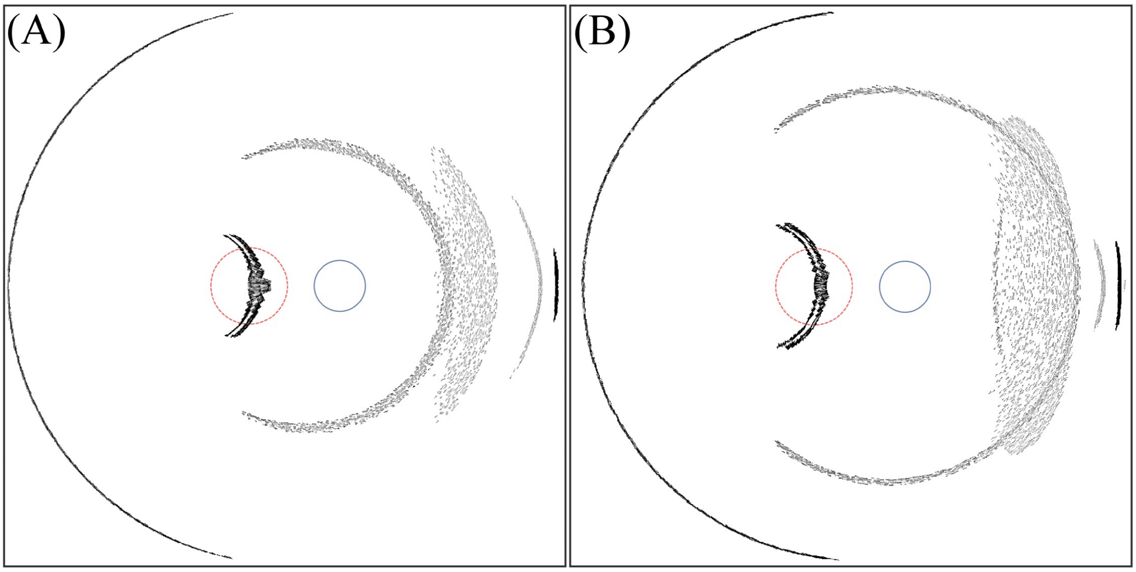

Fig 4. Intensity distribution on the retina for IOL with the standard edge design. (A) For angle of incidence of 77.5˚ and 6 mm optics diameter. (B) For angle of incidence of 78.2˚ and 7 mm optics diameter.

https://doi.org/10.1371/journal.pone.0262457.g004

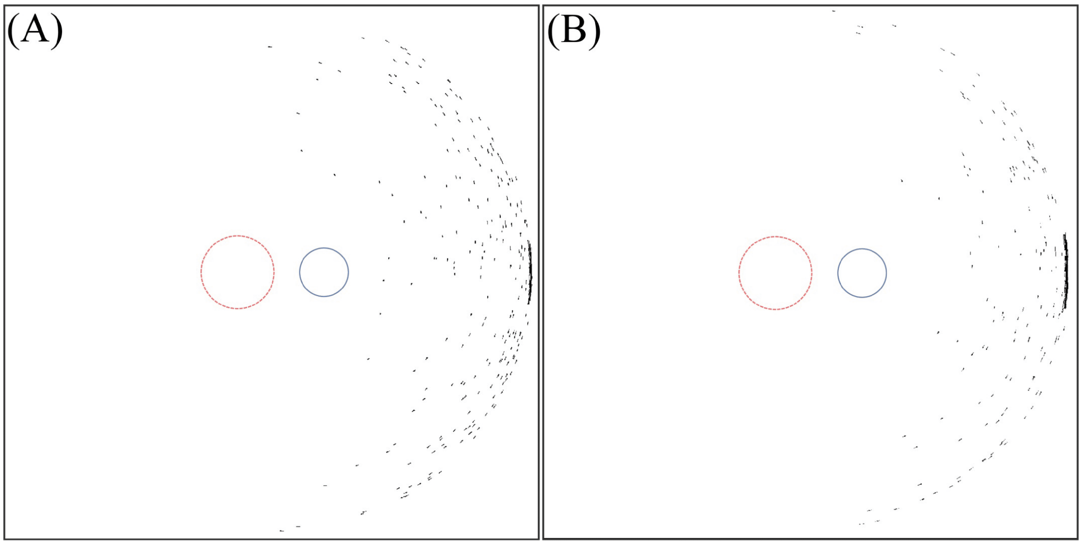

Fig 5. Intensity distribution on the retina for IOL with absorbing edge design. (A) For angle of incidence of 77.5˚ and 6 mm optics diameter. (B) For angle of incidence of 78.2˚ and 7 mm optics diameter.

https://doi.org/10.1371/journal.pone.0262457.g005

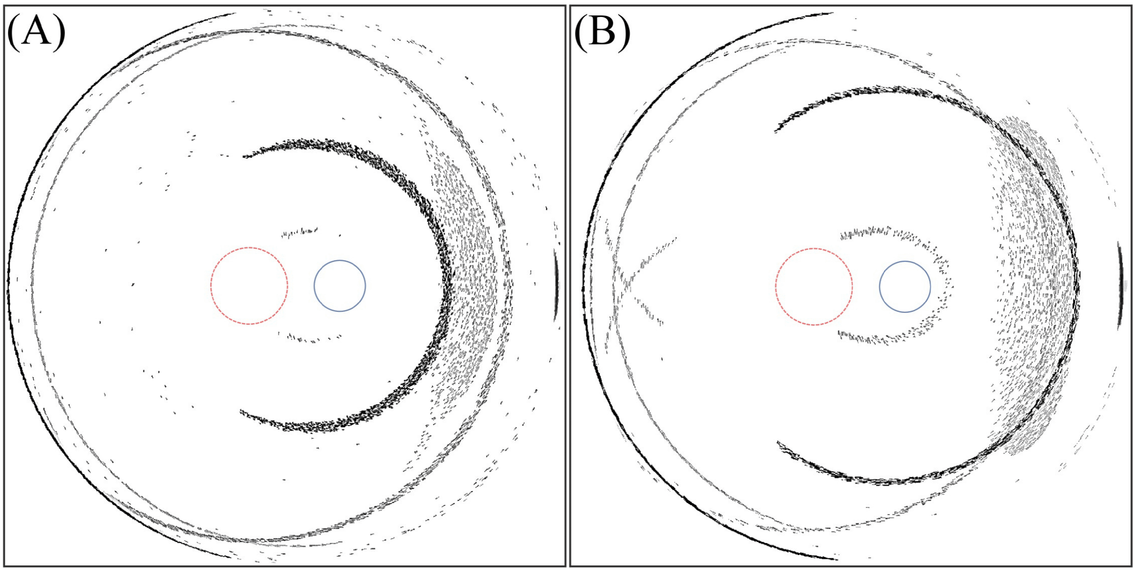

Fig 6. Intensity distribution on the retina for IOL with fully reflecting edge design. (A) For angle of incidence of 77.5˚ and 6 mm optics diameter. (B) For angle of incidence of 78.2˚ and 7 mm optics diameter.

https://doi.org/10.1371/journal.pone.0262457.g006

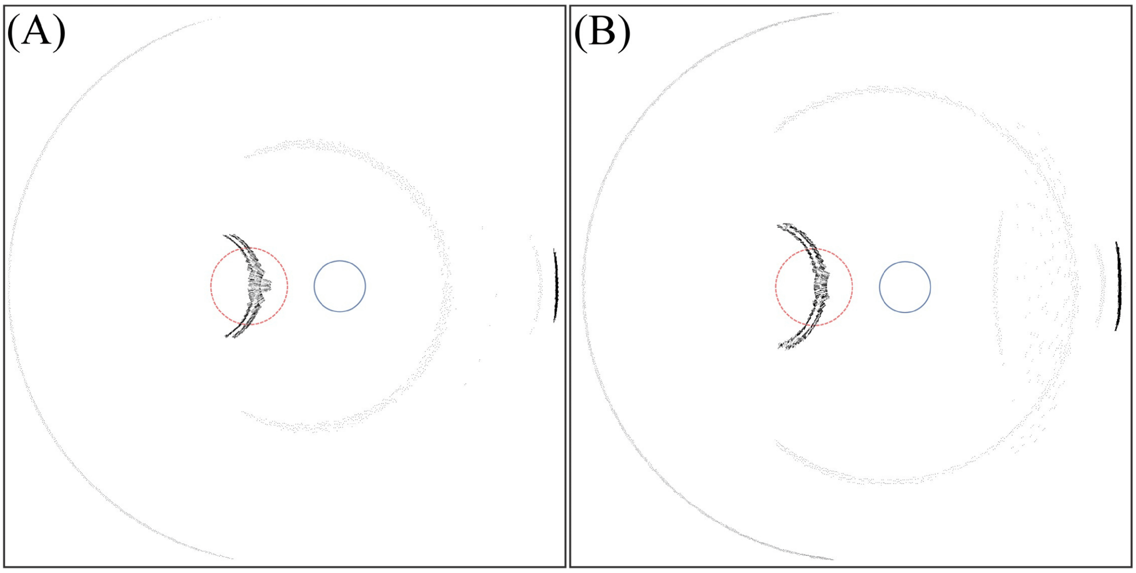

Fig 7. Intensity distribution on the retina for IOL with anti-reflecting edge design. (A) For angle of incidence of 77.5˚ and 6 mm optics diameter. (B) For angle of incidence of 78.2˚ and 7 mm optics diameter.

https://doi.org/10.1371/journal.pone.0262457.g007

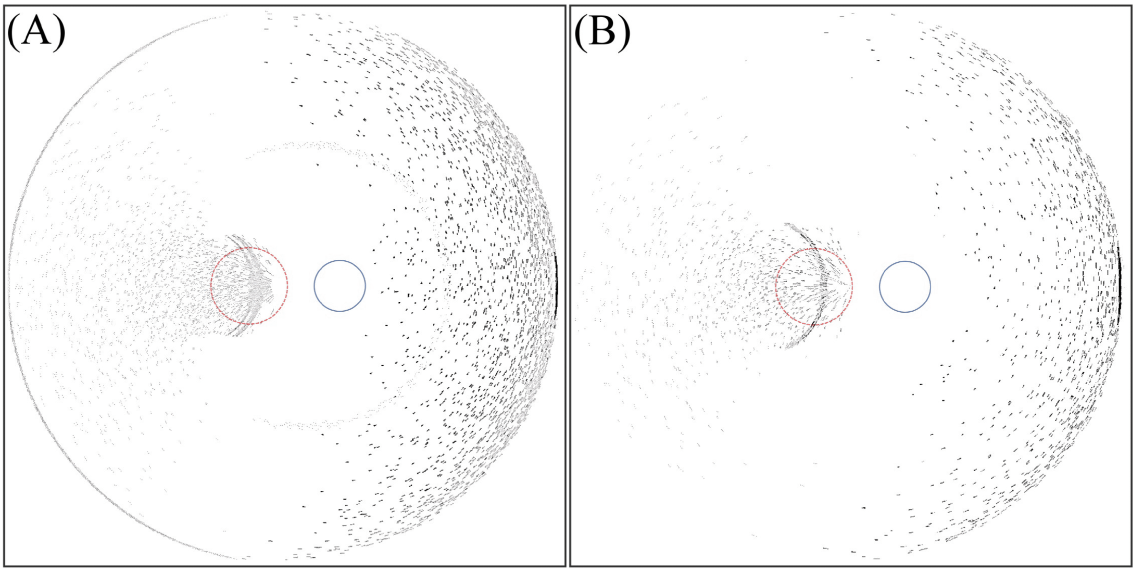

Fig 8. Intensity distribution on the retina for IOL with frosted edge design. (A) For angle of incidence of 77.5˚ and 6 mm optics diameter. (B) For angle of incidence of 78.2˚ and 7 mm optics diameter.

https://doi.org/10.1371/journal.pone.0262457.g008

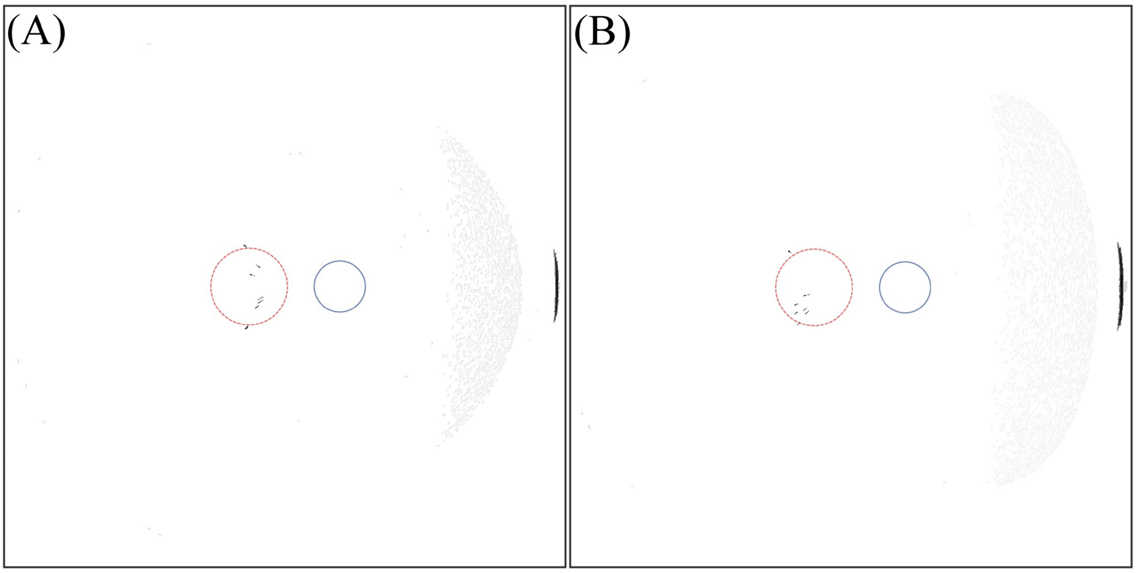

Fig 9. Intensity distribution on the retina for IOL with thin edge design. (A) For angle of incidence of 77.5˚ and 6 mm optics diameter. (B) For angle of incidence of 78.2˚ and 7 mm optics diameter.

https://doi.org/10.1371/journal.pone.0262457.g009

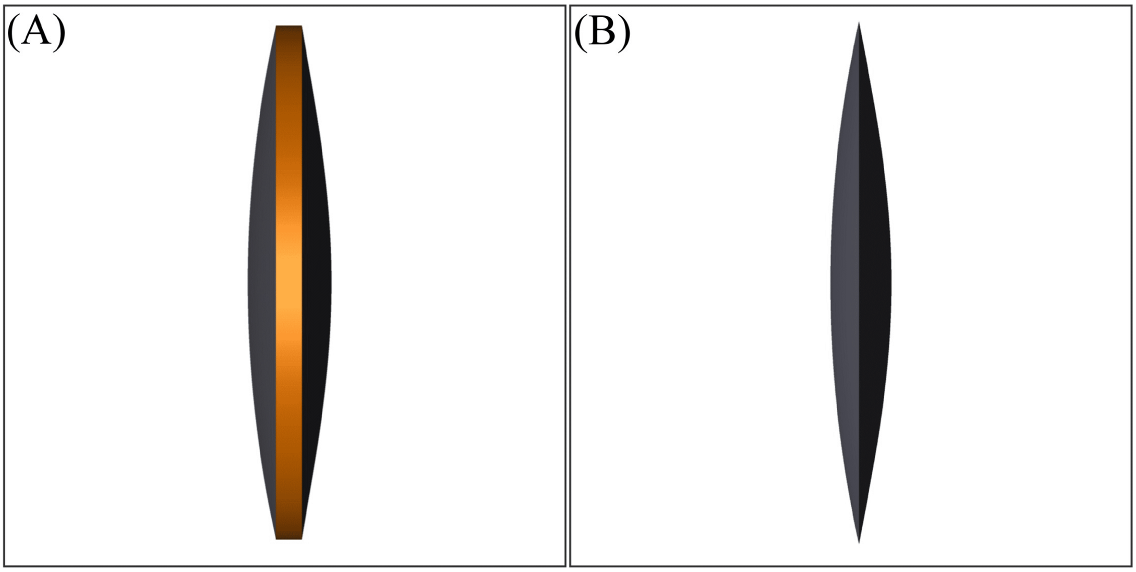

Fig 10. Schematic drawing of the simulated IOLs. (A) Thick IOL with edge thickness of 0.3 mm. (B) Thin IOL with edge thickness of 0.0 mm.

https://doi.org/10.1371/journal.pone.0262457.g010

Similarly, ellipse-like shapes with a lower intensity located at the centre move temporally at the retina. From 50° to 65°, a bean shaped pattern is detected nasally. Moreover, a crescent shape pattern is observed for incident ray angles between 60° and 80° changing in intensity, size, and shape with variation of the incident angle.

With a 6 mm optics IOL, light passing through the interspace between iris and lens is observed from 50° in the temporal region. In observing this effect in IOLs with a 7 mm optics diameter, the inclination angle is 55° as a result of the narrower channel between iris and IOL. In both IOL types, with increasing angle of incidence, the crescent shape pattern moves towards the periphery. The intensity of this crescent increases up to angle of 75° and then decreases. Finally, it can be concluded that between 65° and 80°, photic patterns are located in the foveal region.

From Fig 4, at a 'critical' incident ray angle this light effect hits the fovea, where we expect a serious optical disturbance of the patient because light sensitivity is very high in the foveal spot (Fig 2).

As expected, Fig 5 shows that most of the photic patterns disappear with absorbing an edge.

By analysing Figs 6 and 7, it is concluded that photic patterns can be caused by reflection or transmission of light through the edge of the IOL. In Fig 6, a fully reflective edge causes the crescent that is located at foveal region. Simultaneously, this edge type enhances the intensity of the larger crescent on the temporal region of the retina. Within the temporal region far from the fovea, the sensitivity of the retina is lower and therefore serious optical disturbance is not expected, but the results show that the photic effect could appear in different retinal regions depending on the incident ray angle. The photic effect caused by internal reflection at the edge can appear on the fovea when the incidence angle is 67.4° and 68.8° for IOLs with 6 mm and 7 mm optics diameter respectively. Fig 11 shows the light intensity distribution for this situation.

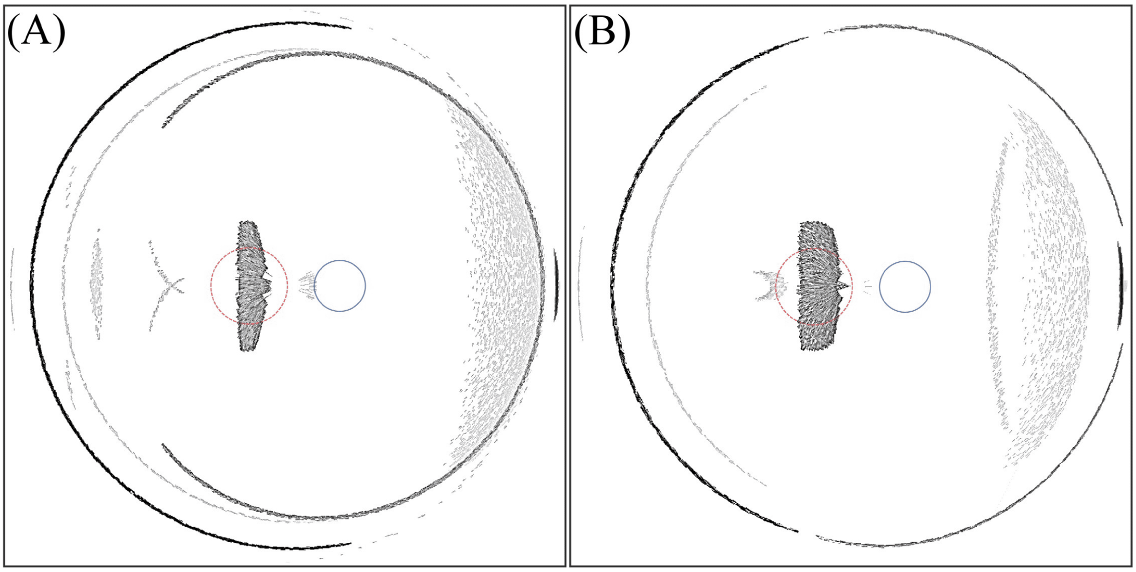

Fig 11. Intensity distribution on the retina for IOL with thin edge design. (A) For angle of incidence of 67.4˚ and 6 mm optics diameter. (B) For angle of incidence of 68.8˚ and 7 mm optics diameter.

https://doi.org/10.1371/journal.pone.0262457.g011

On the other hand, the anti-reflective edge causes the large crescent in the temporal region to disappear but the smaller crescent located on the foveal region is still present and could again cause serious optical disturbance because it is located at the fovea.

Variously, the frosted optics edge design causes a particular effect on the photic patterns on the retinal surface. From Fig 8, it is concluded that the frosted edge scatters the rays transmitted or internally reflected from the IOL edge.

Technically, this effect does not change the overall intensity of the light transmitted or reflected by the edge, but it distributes the light intensity over a larger retinal area, thus reducing the contrast of the patterns. As a result, patients will have less optical disturbance with IOLs with frosted edges by reducing the contrast of the photic effects.

It should be noted that in all of the results with different edge types, the temporal photic pattern generated by light passing through the interspace between iris and IOL does not change. Consequently, modifying the edge design does not affect this aspect of the photic effect. Although it is not possible to eliminate this photic effect with IOL customisation, it does not disturb patients, being located away from the fovea as the most sensitive region of the retina.

Finally, by studying Fig 9, it is observed that there is no photic pattern in the nasal region of the retina with the thin edge design. As expected, the photic pattern originated by the light passing through the interspace between iris and lens, is also observed with this thin edge IOL.

Supporting information

S1 Table.
(XLSX)

Author Contributions

Conceptualization: Pooria Omidi.

Formal analysis: Pooria Omidi, Achim Langenbucher.

Methodology: Pooria Omidi.

Software: Pooria Omidi.

Supervision: Achim Langenbucher.

Validation: Alan Cayless, Achim Langenbucher.

Visualization: Pooria Omidi.

Writing – original draft: Pooria Omidi.

Writing – review & editing: Alan Cayless, Achim Langenbucher.

References

1. Masket S, Geraghty E, Crandall AS, Davison JA, Johnson SH, Koch DD, et al. Undesired light images associated with ovoid intraocular lenses. Journal of Cataract & Refractive Surgery. 1993; 19(6):690–694. https://doi.org/10.1016/s0886-3350(13)80336-7 PMID: 8271163
2. Tester R, Pace NL, Samore M, Olson RJ. Dysphotopsia in phakic and pseudophakic patients: incidence and relation to intraocular lens type. Journal of Cataract & Refractive Surgery. 2000; 26(6):810–816. https://doi.org/10.1016/s0886-3350(00)00427-2 PMID: 10889424
3. Davison JA. Positive and negative dysphotopsia in patients with acrylic intraocular lenses. Journal of Cataract & Refractive Surgery. 2000; 26(9):1346–1355. https://doi.org/10.1016/s0886-3350(00)00611-8 PMID: 11020620
4. Narváez J, Banning CS, Stulting RD. Negative dysphotopsia associated with implantation Z9000 intraocular lens. Journal of Cataract & Refractive Surgery. 2005; 31(4):846–847. https://doi.org/10.1016/j.jcrs.2004.08.059 PMID: 15899465
5. Radford SW, Carlsson AM, Barret GD. Comparison of pseudophakic dysphotopsia with Akreos Adapt and SN60-AT intraocular lenses. Journal of Cataract & Refractive Surgery. 2007; 33(1):88–93. https://doi.org/10.1016/j.jcrs.2006.09.014 PMID: 17189799
6. Osher RH. Negative dysphotopsia: long-term study and possible explanation for transient symptoms. Journal of Cataract & Refractive Surgery. 2008; 34(10):1699–1707. https://doi.org/10.1016/j.jcrs.2008.06.026 PMID: 18812121
7. Vámosi P, Csákány B, Németh J. Intraocular lens exchange in patients with negative dysphotopsia symptoms. Journal of Cataract & Refractive Surgery. 2010; 36(3):418–424. https://doi.org/10.1016/j.jcrs.2009.10.035 PMID: 20202539
8. Cooke DL. Reply: Optical phenomena causing negative dysphotopsia. Journal of Cataract & Refractive Surgery. 2010; 36(10):1620–1621.
9. Masket S, Fram NR. Pseudophakic negative dysphotopsia: surgical managemanet and new theory of etiology. Journal of Cataract & Refractive Surgery. 2011; 37(7):1199–1207.
10. Holladay JT, Lang A, Portney V. Analysis of edge glare phenomena in intraocular lens edge design. Journal of Cataract & Refractive Surgery. 1999; 25(6):748–752.
11. Holladay JT, Zhao H, Reisin CR. Negative dysphotopsia: the enigmatic penumbra. Journal of Cataract & Refractive Surgery. 2012; 38(7):1251–1265. https://doi.org/10.1016/j.jcrs.2012.01.032 PMID: 22727295
12. Schweigerling J. Recent developments in pseudophakic dysphotopsia. Current option in ophthalmology. 2006; 17(1):27–30.
13. Holladay JT, Bishop JE, Lewis JW. Diagnosis and treatment of mysterious light streaks seen by patients following extracapsular cataract extraction. American Intra-Ocular Implant Society Journal. 1985; 11(1):21–23. https://doi.org/10.1016/s0146-2776(85)80108-7 PMID: 3967988
14. Holladay JT. Evaluating the intraocular lens optic. Survey of ophthalmology. 1986; 30(6):385–390. https://doi.org/10.1016/0039-6257(86)90092-5 PMID: 3726748
15. Liou HL, Brennan NA. Anatomically accurate, finite model eye for optical modeling. JOSA A. 1997; 14(8): 1684–1695. https://doi.org/10.1364/josaa.14.001684 PMID: 9248060

4.4 Paper 4

Title: Intensity simulation of photic effects after cataract surgery for off-axis light sources

Authors: Pooria Omidi, Alan Cayless, Achim Langenbucher

Publication date: 05/08/2022

Journal: Plos one (Public Library of Science)

Volume(Issues): 17(8)

Pages: e0272705

PLOS ONE

RESEARCH ARTICLE

Intensity simulation of photic effects after cataract surgery for off-axis light sources

Pooria Omidi[1]*, **Alan Cayless**[2], **Achim Langenbucher**[1]

1 Department of Experimental Ophthalmology, Saarland University, Homburg, Saar, Germany, **2** School of Physical Sciences, The Open University, Milton Keynes, United Kingdom

* Pooria.omidi@uks.eu

Abstract

Photopsia is a photic phenomenon that can be associated with intraocular lenses after cataract surgery. To calculate the relative light intensity of photic effects observed after cataract surgery at the foveal region as the most sensitive region of the retina, photopsia was simulated using the ZEMAX optical design software. The simulations are based on the Liou-Brennan eye model with a pupil diameter of 4.5 mm and incorporating implanted IOLs. The hydrophilic IOLs implanted in the eye model have a power of 21 diopter (D) with an optic diameter of 6 mm and 7 mm. Four different intensity detectors are located in specific regions of the eye in this simulation. The ray-tracing analysis was carried out for variations of incident ray angle of 0˚ to 90˚ (temporally) in steps of 1˚. Depending on the range of incident ray angle, the light intensity was detected at detectors located on the fovea, nasal side of the retina, or the edge surface of the IOLs. Some portion of the input light was detected at specific incident angles in the foveal region. By altering the IOLs edge design to a fully reflective or anti-reflective surface, the range over which the light intensity is detected on the fovea can be shifted. Additionally, with the absorbing edge design, no intensity was detected at the foveal region for incident ray angles larger than 5˚. Therefore an absorbing edge design can make photic effects less disturbing for patients.

OPEN ACCESS

Citation: Omidi P, Cayless A, Langenbucher A (2022) Intensity simulation of photic effects after cataract surgery for off-axis light sources. PLoS ONE 17(8): e0272705. https://doi.org/10.1371/journal.pone.0272705

Editor: Michael Mimouni, University of Toronto, CANADA

Received: January 18, 2022

Accepted: July 25, 2022

Published: August 5, 2022

Data Availability Statement: All relevant data are within the paper and its Supporting Information files.

Funding: This work is original and has not been published or is currently under consideration for publication elsewhere. J.S. was supported in part by the Rolf M. Schwiete Stiftung under project nr. 11/2018. (https://schwiete-stiftung.com/).

Competing interests: NO authors have competing interests.

Introduction

Photopsia is an optical phenomenon that sometimes occurs shortly after cataract surgery. In this phenomenon light which is not directly correlated to an object is detected in the visual field. Clinical studies show that the photic effects caused by photopsia are mostly located in the temporal visual field. This effect has been named *dysphotopsia* by Tester et al. [1]. Masket et al. was the first to report that this effect could be associated with the optical design and position of IOLs in the eye [2] and Holladay et al. studied the effect of the IOL edge design on this phenomenon using a ZEMAX software simulation [3, 4].

Generally, patients do not suffer from photic effects after intraocular lens implantation. A few cases with these symptoms do not feel disturbed and they can tolerate this phenomenon [5, 6]. However, in rare cases, patients are severely disturbed by photopsia [3, 7, 8]. There is no clinical test to verify photopsia as this phenomenon cannot be measured objectively.

In the literature, several explanations for this phenomenon such as defects in the IOL optics during manufacturing, central optical defects during folding and injection [9], IOL material with a high index refractive index [5, 10, 11], optics with sharp or truncated edges [5, 10, 11], a cataract incision located temporally in the clear cornea [12], a prominent globe [13], lack of neural adaptation [14], and reflection of the anterior capsulotomy edge projected onto the nasal peripheral retina for photopsia, have been discussed. Moreover, there is no systematic correlation between photopsia and corneal diameter, anterior chamber depth, iris pigmentation, and photopic and scotopic pupil diameter or refraction [12].

In our previous study, we modelled the impact of the edge design of intraocular lenses (IOL) on the location, shape and relative intensity of photic effects at different regions of the retina [15].

In this paper, we have simulated the photic effects after cataract surgery in different regions of the pseudophakic eye. The main objective of this study is to calculate the relative light intensity of the photic effects on the foveal region as the most sensitive part of the retina, in order to better understand the effect of incident angles on the fixed eye model. Therefore we have defined our model based on parameters derived from the schematic model eye. Moreover, we have simulated the impact of the IOL edge design on the relative light intensity of the photic effects on the fovea.

Methods

This study was registered at the local ethics committee of the Medical Association of Saarland (Ärztekammer des Saarlandes, 157/21).

Eye model specifications

In this study, a pseudophakic eye model based on the Liou-Brennan schematic model eye introduced in 1997 was used for simulation [16]. Liou-Brennan model eye has an equivalent power of 60.35 D and an axial length of 23.95 mm.

The cornea of this model is defined by two rotationally symmetric surfaces (the front and back surface) with radii of 7.77 mm and 6.40 mm and asphericity of -0.18 and -0.60, respectively. The interspace between corneal surfaces is 0.5 mm with a refractive index of 1.376. The retina in defined by a half sphere with a radius of 12 mm and the fovea as the intersection of the visual axis and the retina with a diameter of 1.5 mm. The pupil diameter used in this model is 4.5 mm.

According to the schematic model eye of Liou & Brennan, all optical elements (corneal front and back surface, lens front and back surface) are centred on the 'optical axis'. The pupil is somehow decentered by 0.5 mm in the nasal direction with respect to the optical axis to consider the incident ray angle of 5° from the nasal direction, as given by the model eye.

In this model, two acrylic hydrophilic IOLs with a refractive power of 21 D and refractive index of 1.458 are aligned with their equator in the equatorial plane of the crystalline lens of the eye model.

The front surface of the IOLs is defined by a spherical surface and the back surface by an aspherical surface optimized for 0.26 μm spherical aberration in the total eye model. These IOLs have a sharp circular optical edge with a thickness of 0.3 mm and optical diameters of 6 mm and 7 mm respectively. Finally, after IOL implantation in the model, the anterior chamber depth of the model eye is about 4 mm.

In our simulation we used these model eye data as a baseline and varied the incident ray angle to determine the critical ray incidence where (unwanted) light effects at the foveal region are observed. Table 1 lists all the relevant parameters of the proposed pseudophakic model eye and the polynomial coefficients that describe the rotationally symmetric aspheric surface of the IOL. Note that any polynomial coefficient values not specified in the table equal zero.

Table 1. Structural parameters of the pseudophakic eye model.

Surface	Medium	Radius[mm]	Asphericity	Thickness[mm]	Optical diameter[mm]
1	Cornea	7.77	-0.18	0.5	14
2	Aqueous	6.40	-0.6	3.16	14
3	Aqueous	∞	-	1	4.5
4	Hydrophilic IOL	13.86	-	0.97	6 and 7
5	Vitreous	-11.66	-1.5	18.32	6 and 7
6	-	-12	-	-	24
Surface	α_2[mm^{-1}]	α_4[mm^{-3}]	α_6[mm^{-5}]	α_8[mm^{-7}]	α_{10}[mm^{-7}]
5	-6.34e^{-3}	1.15e^{-3}	-3.86e^{-7}	-2.47e^{-8}	-

https://doi.org/10.1371/journal.pone.0272705.t001

To analyse the intensity of photic effects, four different light detectors are placed on different regions of the eye model. Fig 1 illustrates a schematic sketch of the eye model used in this study. Each surface is labeled with a number from 1 to 6 and detectors are shown in orange.

A circular light detector is located at the pupil to calculate the total intensity of light passing through the pupil. This detector is named as ”Detector-P”.

A second detector that named as ”Detector-N” is located at the periphery of the nasal side of the retina and calculates the light intensity passing through the interspace between iris and IOL without hitting the lens.

Another detector is located at the edge surface of the IOLs and measures the intensity of the light hitting the lens edge surface. This detector is named ”Detector-E”.

Finally, the last detector named ”Detector-F” is located at the foveal region to calculate the light intensity of the photic effects at the fovea.

Since the foveal region is the most sensitive region of the retina, even low intensities of light uncorrelated to the object space may cause optical disturbance for patients. The closer to the fovea, the more sensitive is the retinal surface.

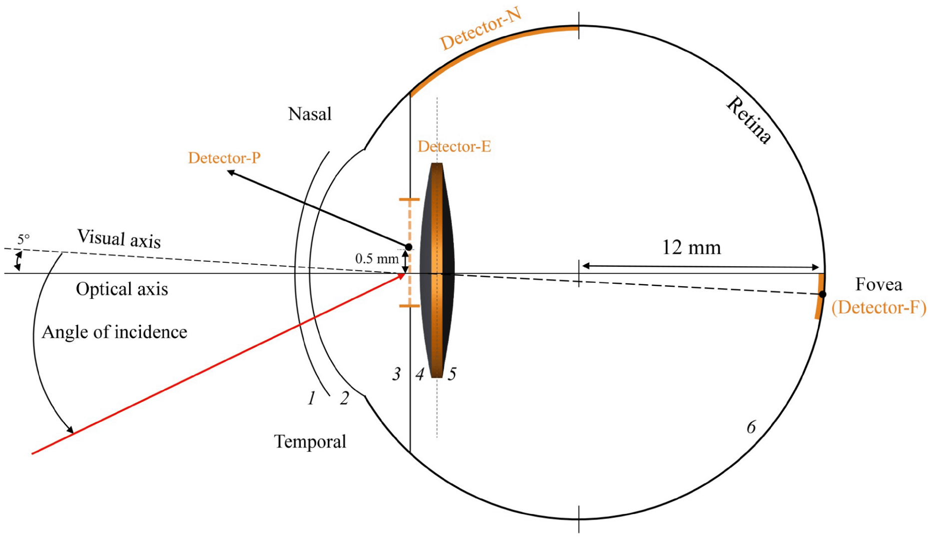

Fig 1. Schematic drawing of the pseudophakic eye and the detectors. (see Table 1 for parameter values).

https://doi.org/10.1371/journal.pone.0272705.g001

To evaluate the contribution of the edge surface properties of the IOL on the intensity of the photic effects at the foveal region (Detector-F), three different edge designs with fully reflective, anti-reflective, and absorbing surfaces respectively were simulated.

With specular reflecting and anti-reflecting IOL edges, the effects of internal specular reflection and transmission are highlighted, respectively. By simulating an IOL with an absorbing edge, light transmission through and reflection off the edge is suppressed. These simulations provide insight to study the transmission, reflection, and absorption of the edge surface separately.

Ray tracing procedure

Ray tracing was performed to calculate the intensity of photic effects reaching the foveal and retinal surface in comparison to the total power passing through the pupil. All of the simulations were carried out using the non-sequential ray-tracing mode of the ZEMAX professional ray-tracing software (Version 21.3, Washington, USA).

A collimated light pencil with 5 million rays from an extended light source is used to analyse the intensity of photic effects. The rays are distributed homogeneously over the pupil, and there is no weighting in their distribution function.

Rays from 0° to 90° degrees from the temporal direction in steps of 1° with respect to the visual axis (slanted by 5° to the optical axis) were traced temporally through the pupil to evaluate the intensity of the photic effects on the different detectors.

For each incident angle, the intensity obtained by the detectors are documented and referenced to the light intensity passing through the pupil.

Results

Fig 2 shows the total input intensity detected by Detector-P as a function of the incident ray angle in comparison to the cosine squared function which resamples the intensity characteristics of a light pencil passing through a circular pupil.

With increasing incident ray angle, the total intensity of light decreases, but the difference between the normalised intensity of the light passing through the pupil and the cosine squared function increases.

Fig 3 shows the light intensity detected by Detector-N which passes through the pupil without interacting elements in between. Note that the light intensities are normalised to the total light intensity passing through the pupil at each angle.

It can be seen that rays passing through the interspace between IOL and pupil are detected for incident ray angles exceeding the critical angles 44° and 55° for IOLs with an optical diameter of 6 mm and 7 mm, respectively. The light intensity increases with the angle of incidence from these critical angles to 90°.

Fig 4 shows the total intensity of the rays interacted with the IOL edges which are detected by Detector-E subdivided by the total intensity entering the eye (Detector-P) over the angle of incidence.

In this figure, rays from the incident angle of 42° start to interact with the edges of 6 mm IOL, and the rays from the incident of 48° start to interact with edges of 7 mm IOL. With increasing angle of incidence, the detected intensity at the edges initially increases dramatically, and then the intensity fluctuates slightly.

Fig 5 shows the total intensity of the rays hitting with the foveal (Detector-F) region normalised by the total intensity passing through the pupil when the IOLs are simulated with a fully reflective edge surface.

For small incident ray angles from 0° to 5°, almost all of the light passing through the pupil reaches the foveal region. For larger incident ray angles the light intensity on the foveal region

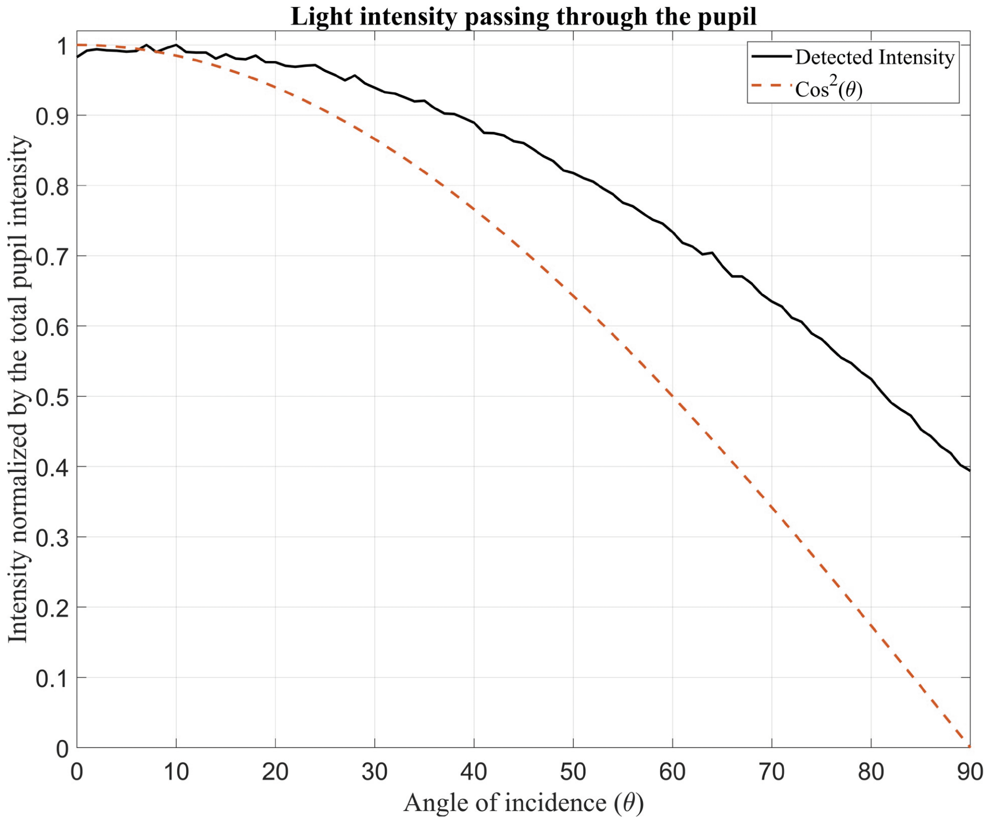

Fig 2. Normalised input intensity detected by the detector located on the pupil (Detector-P) over the incident ray angle.

https://doi.org/10.1371/journal.pone.0272705.g002

decreases down to 0.001% of the light intensity passing through the pupil. In the range from 60˚ to 70˚, about one percent of the total input light is detected at the foveal region.

Fig 6 shows the total intensity of the rays hitting the foveal region (Detector-F) normalised by the total intensity passing through the pupil when the IOLs are simulated with anti-reflective edge surfaces.

In this figure, it can be observed that from incident ray angles between 70˚ to 80˚ about one percent of the light at the foveal region is detected. For the IOLs with 6 mm and 7 mm optical diameter, 0.3% of the input light is detected at angles of 77˚ to 78˚ respectively.

Finally, Fig 7 displays the total light intensity hitting the detector at the foveal region (Detector-F) normalised by the total light intensity passing through the pupil as a function of incident ray angle when the IOLs are simulated with absorbing edge surfaces.

In this figure, no intensity is detected at the fovea for incident ray angles exceeding 50˚.

Discussion

There have been several studies focused on IOL design and position to reduce photic effects [17]. Holladay et al. showed that the IOL edge design can affect the location and relative

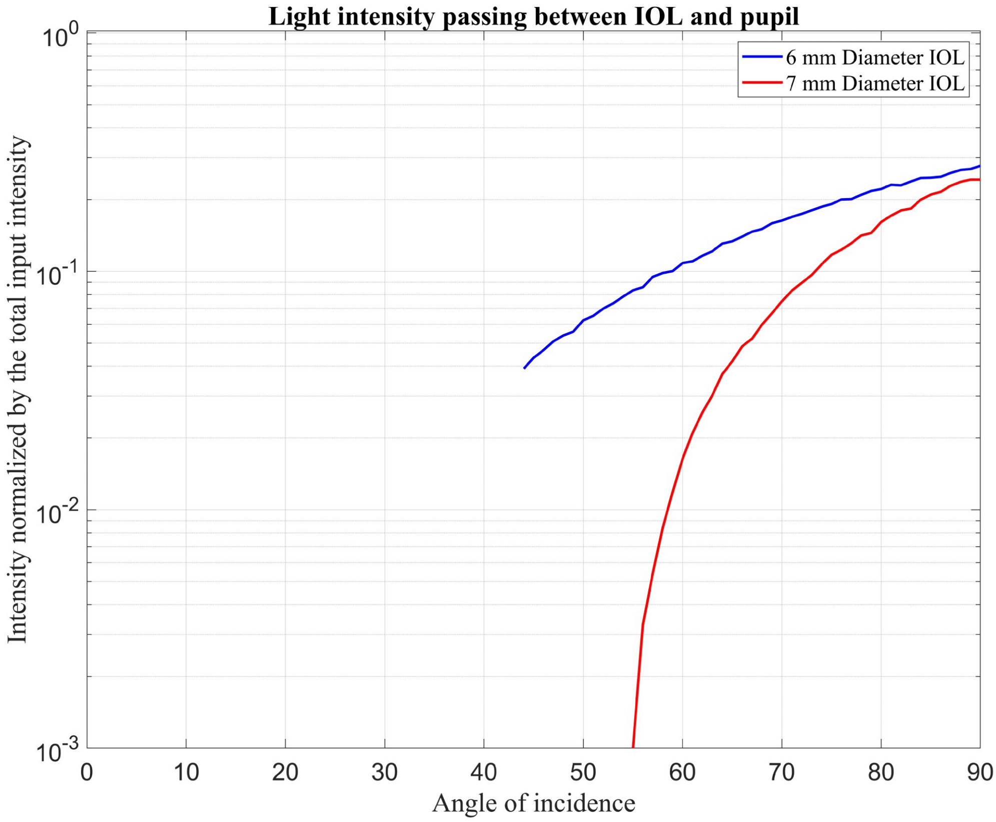

Fig 3. Normalised input intensity detected by the Detector-N over the incident ray angle.

https://doi.org/10.1371/journal.pone.0272705.g003

intensity of photic effects. Moreover, a sharp edge design of the IOL is one of the primary optical factors required for negative dysphotopsia [4]. Erie et al. modified the IOL design to reduce the intensity of photic effects. They showed that their new IOL design (having a peripheral concave posterior surface) provides more uniform illumination of the peripheral nasal retina and could thereby reduce negative dysphotopsia [18]. In the present study, we have modified the optical properties of the edge surface to investigate their impact on photic effects.

Standard ray-tracing techniques show that different incident angles cause the incoming light to be directed to various regions of the retinal surface. The intensity and location of these rays depend on how they interact with the IOL surfaces (front, back, edge). There is expected to be a correlation between the location of the photic effects and the amount of disturbance for the patients because different regions on the retina are differently sensitive to light.

In Fig 2 the black curve showing the total intensity passing through the pupil when a cornea is simulated in front is located above the red curve which shows total intensity passing through the pupil. As a result of the positive refracting power of the cornea, more light enters the eye at higher angles of incidence. These simulation results confirm that the illumination to the model eye has been implemented correctly.

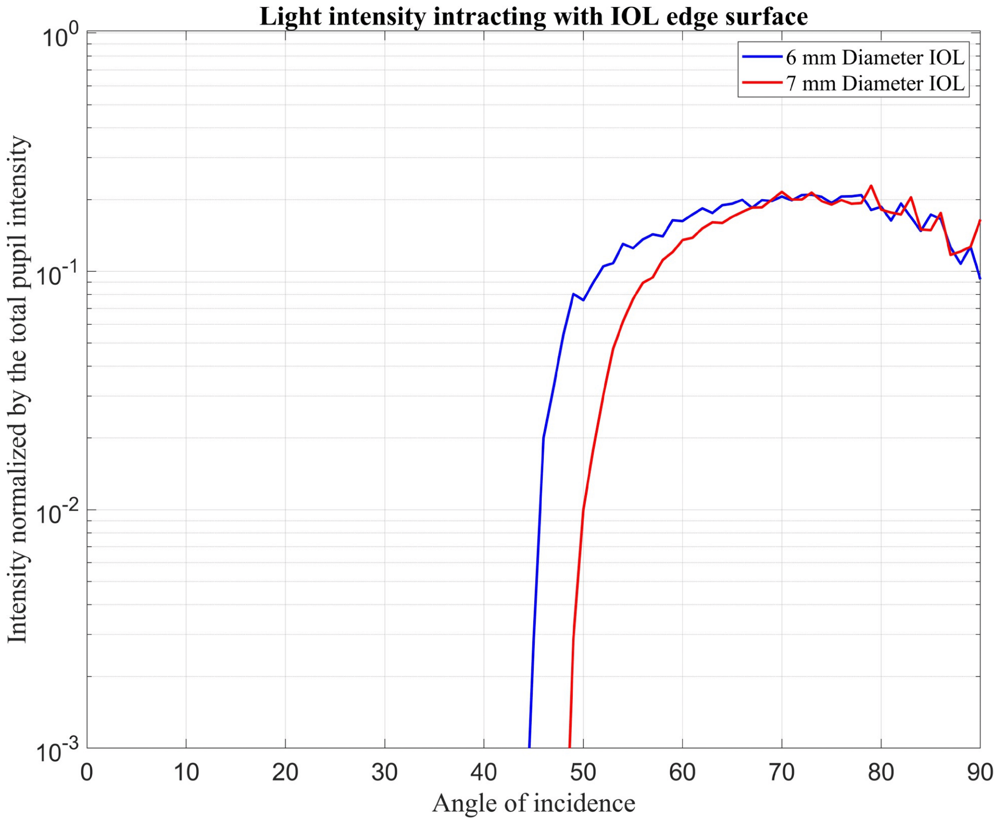

Fig 4. Normalised input intensity detected by the Detector-E over the incident ray angle.

https://doi.org/10.1371/journal.pone.0272705.g004

In Figs 3 and 4, both detectors start to detect light intensity at lower angles for 6 mm IOL size. The standard explanation is that the 6 mm IOL is smaller than the 7 mm IOL and occupies less space in the eye. More space in the pseudophakic eye allows beams to reach the retina at lower angles. Moreover, in the 6 mm IOL, beams interacted with the edges of the IOL earlier (42˚) than in the 7 mm IOL (48˚). With increasing angle of incidence, the detected intensity at the edges initially increases dramatically, and then the intensity slope reduces. This phenomenon can be explained in terms of a range of incident ray angles covering the total edge surfaces.

In Fig 5, for the IOL with a 6 mm optical diameter, 0.5% of the input light is detected at an angle of 66˚ and for the IOL with a 7 mm optical diameter, 1.4% of the input light is detected at an angle of 67˚. These intensities are caused by the reflection of beams entering the front surface and reflected from the IOL edge surface.

By changing the edge design from a fully reflective to an anti-reflective surface, the photic effects are detected within a different range of incident angles.

For incident ray angles in a range between 0˚ and 50˚, the light intensities shown in Figs 5 and 6 are almost similar. These results show that with the specific incident ray

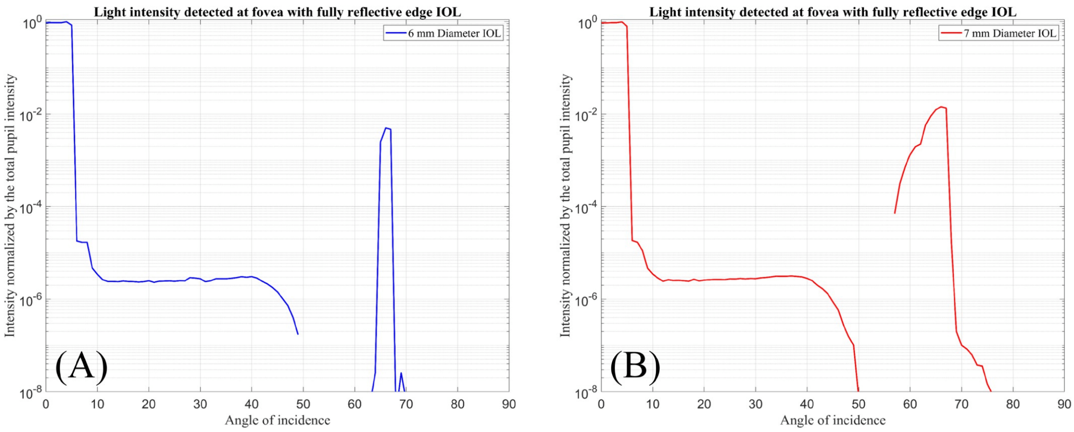

Fig 5. Normalised input intensity detected by Detector-F over the incident ray angle. (A) For 6 mm diameter IOL with fully reflective edge surface. (B) For 7 mm diameter IOL with fully reflective edge surface.

https://doi.org/10.1371/journal.pone.0272705.g005

angles light reflected or transmitted from the edges could cause disturbance for the patients.

Finally, Fig 7 shows that with an absorbing IOL edge, no intensity is detected at the fovea with incident ray angles exceeding 50°. Therefore, it can be concluded that all of the photic effects detected at the foveal region are generated by light reflected or transmitted from the edges. As a result, among these three IOL types, with absorbing edge IOL we can expect that patients will have less optical disturbance after cataract surgery.

Clinical studies in the future will be needed to prove the validity of our simulation model in a clinical environment.

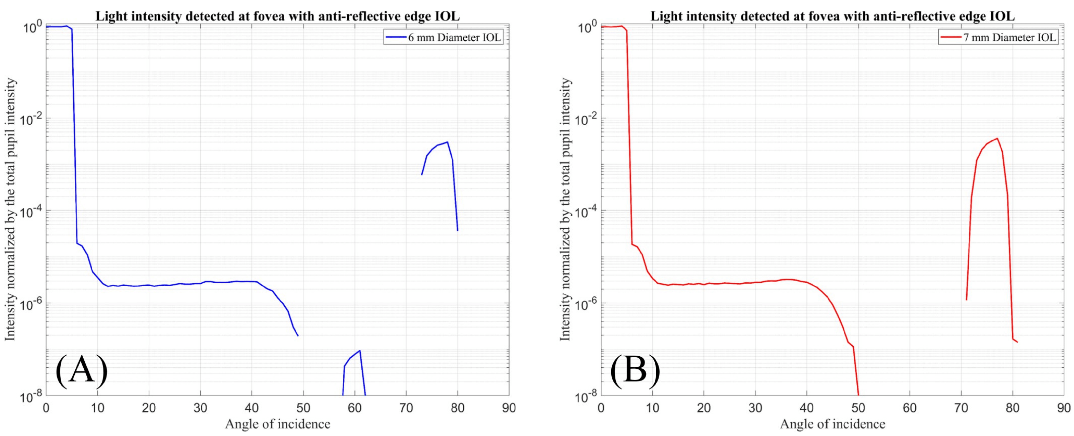

Fig 6. Normalised input intensity detected by Detector-F over the incident ray angle. (A) For 6 mm diameter IOL with anti-reflective edge surface. (B) For 7 mm diameter IOL with anti-reflective edge surface.

https://doi.org/10.1371/journal.pone.0272705.g006

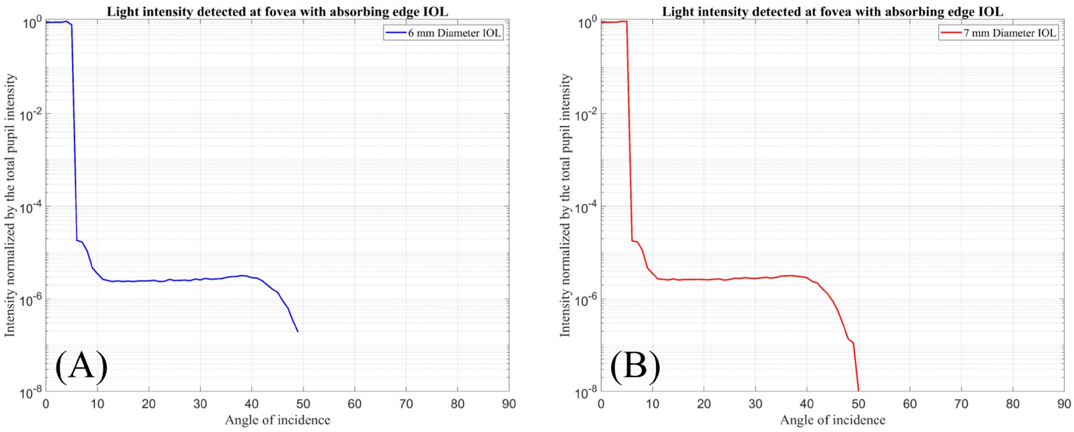

Fig 7. Normalised input intensity detected by Detector-F over the incident ray angle. (A) For 6 mm diameter IOL with absorbing edge surface. (B) For 7 mm diameter IOL with absorbing edge surface.

https://doi.org/10.1371/journal.pone.0272705.g007

Limitations of this study

This study has the character of a pilot study and our principal aim has been to demonstrate the applicability of this concept. Our model in this study is based on the Liou-Brennan schematic model eye. This model reflects only an average geometry of a human eye. Since we would expect the behaviour of photic effects to vary across eyes with different proportions and corneal shape as well as pupil sizes/locations, it can be concluded that our results cannot be generalised to all human eyes on the basis of the current study alone.

Supporting information

S1 Data.
(XLSX)

Author Contributions

Conceptualization: Pooria Omidi, Achim Langenbucher.

Formal analysis: Pooria Omidi, Achim Langenbucher.

Funding acquisition: Achim Langenbucher.

Methodology: Pooria Omidi.

Project administration: Achim Langenbucher.

Software: Pooria Omidi.

Supervision: Achim Langenbucher.

Validation: Pooria Omidi, Alan Cayless, Achim Langenbucher.

Visualization: Pooria Omidi.

Writing – original draft: Pooria Omidi.

Writing – review & editing: Alan Cayless, Achim Langenbucher.

References

1. Tester R, Pace NL, Samore M, Olson RJ. Dysphotopsia in phakic and pseudophakic patients: incidence and relation to intraocular lens type. Journal of Cataract & Refractive Surgery. 2000; 26(6):810–816. https://doi.org/10.1016/s0886-3350(00)00427-2 PMID: 10889424
2. Masket S, Geraghty E, Crandall AS, Davison JA, Johnson SH, Koch DD, et al. Undesired light images associated with ovoid intraocular lenses. Journal of Cataract & Refractive Surgery. 1993; 19(6):690–694. https://doi.org/10.1016/s0886-3350(13)80336-7 PMID: 8271163
3. Holladay JT, Lang A, Portney V. Analysis of edge glare phenomena in intraocular lens edge design. Journal of Cataract & Refractive Surgery. 1999; 25(6):748–752.
4. Holladay JT, Zhao H, Reisin CR. Negative dysphotopsia: the enigmatic penumbra. Journal of Cataract & Refractive Surgery. 2012; 38(7):1251–1265. https://doi.org/10.1016/j.jcrs.2012.01.032 PMID: 22727295
5. Davison JA. Positive and negative dysphotopsia in patients with acrylic intraocular lenses. Journal of Cataract & Refractive Surgery. 2000; 26(9):1346–1355. https://doi.org/10.1016/s0886-3350(00)00611-8 PMID: 11020620
6. Schwiegerling J. Recent developments in pseudophakic dysphotopsia. Current option in ophthalmology. 2006; 17(1):27–30. https://doi.org/10.1097/01.icu.0000193065.09499.7e PMID: 16436921
7. Holladay JT, Bishop JE, Lewis JW. Diagnosis and treatment of mysterious light streaks seen by patients following extracapsular cataract extraction. American Intra-Ocular Implant Society Journal. 1985; 11 (1):21–23. https://doi.org/10.1016/s0146-2776(85)80108-7 PMID: 3967988
8. Holladay JT. Evaluating the intraocular lens optic. Survey of ophthalmology. 1986; 30(6):385–390. https://doi.org/10.1016/0039-6257(86)90092-5 PMID: 3726748
9. Cecchini P D'Aloisio R, Giacinto C, Turco G, Tognetto D. Scanning electron microscopy study of different one-piece foldable acrylic intraocular lenses after injection through microincisional cataract surgery cartridges. International Ophthalmology. 2020; 40(2): 369–376. https://doi.org/10.1007/s10792-019-01193-7 PMID: 31624987
10. Narváez J, Banning CS, Stulting RD. Negative dysphotopsia associated with implantation Z9000 intraocular lens. Journal of Cataract & Refractive Surgery. 2005; 31(4):846–847. https://doi.org/10.1016/j.jcrs.2004.08.059 PMID: 15899465
11. Radford SW, Carlsson AM, Barret GD. Comparison of pseudophakic dysphotopsia with Akreos Adapt and SN60-AT intraocular lenses. Journal of Cataract & Refractive Surgery. 2007; 33(1):88–93. https://doi.org/10.1016/j.jcrs.2006.09.014 PMID: 17189799
12. Osher RH. Negative dysphotopsia: long-term study and possible explanation for transient symptoms. Journal of Cataract & Refractive Surgery. 2008; 34(10):1699–1707. https://doi.org/10.1016/j.jcrs.2008.06.026 PMID: 18812121
13. Vámosi P, Csákány B, Németh J. Intraocular lens exchange in patients with negative dysphotopsia symptoms. Journal of Cataract & Refractive Surgery. 2010; 36(3):418–424. https://doi.org/10.1016/j.jcrs.2009.10.035 PMID: 20202539
14. Cooke DL. Reply: Optical phenomena causing negative dysphotopsia. Journal of Cataract & Refractive Surgery. 2010; 36(10):1620–1621.
15. Omidi P, Cayless A, Langenbucher A. Simulation of photic effects after cataract surgery for off axis light sources. Plos One. 2022; 17(1): e0262457. https://doi.org/10.1371/journal.pone.0262457 PMID: 35051191
16. Liou HL, Brennan NA. Anatomically accurate, finite model eye for optical modeling. JOSA A. 1997; 14 (8): 1684–1695. https://doi.org/10.1364/josaa.14.001684 PMID: 9248060
17. Masket S. Development of an anti-dysphotopic IOL. Expert Review of Ophthalmology. 2019; 14(1): 1–3.
18. Erie JC, Simpson MJ, Bandhauer MH. A modified intraocular lens design to reduce negative dysphotopsia. Journal of Cataract & Refractive Surgery. 2019; 45(7): 1013–1019. https://doi.org/10.1016/j.jcrs.2019.01.019 PMID: 31003799

5 Discussion

The ray tracing and theoretical models were constructed similarly to the study of the IOL alignment and the effect of misalignment on the fixation axis and refraction. The limitations of these models were largely the same. The models differ in their representation of the cornea and the implementation of the virtual iris.
There are several mathematical and statistical models to represent the corneal surfaces. None of them can perform exactly as an individualized patient's cornea. Only with spherical corneal representation, the residual wavefront error might lead to inaccurate calculations. In addition to the asymmetries and local deformations in the surface geometry of the individualized corneas, the thickness of the corneal tissue differs from patient to patient. There is also another issue that should be addressed. An angle between the corneal axis and the crystalline lens axis can be observed by anterior segment tomography. In most of the model's eyes, this angle is ignored.
These neglected factors could be critical for the new ray tracing model, especially when the corneal surfaces are represented with a conic surface. Moreover, in pseudophakic eyes, the implantation of an artificial lens using a small incision can slightly change the shape of the cornea and thereby influence the aberrations. The spherical aberration is quite stable, and astigmatism changes according to the position of the corneal incisions, while other aberrations (coma, trefoil) change in an unpredictable manner. Corneal shape fluctuations also limit the calculation accuracy for customized IOLs, in addition to IOL alignment errors. This is because alignment errors of the corneal surfaces could not be completely compensated for by the object point correction since the virtual fovea of the ray tracing models was always positioned on the video keratometry axis. With all this, we can conclude that the corneal surface shape and thickness will affect the optical path length of a single ray. In pathological corneas, such as keratoconus, poor accuracy of the models results in a larger approximation error. In addition to possibly less accurate biometry in pathological eyes, the position estimation becomes less reliable for the keratoconus group, and the uncertainty of the selection of the IOL refractive power increases. Because the general methods were developed for the statistical average of normal eyes in healthy conditions. Therefore the closer our models are to the real eye structure, the more accurate the wavefront analysis and position estimation will be.
Our solution was to introduce some appropriate mathematical functions for suitable corneal representation. Zernike polynomials are often used for the analysis of optical

wavefronts. But it is beneficial to expand their use for modelling the height data of the corneal surfaces. The advantage of their use is that they can represent any unique corneal surface with asymmetries and deformations. Therefore, creating eye models with real patient data using Zernike polynomials can lead us to simulate more accurate models of realistic eyes and evaluate their optical performance separately.
One of the primary benefits of this representation is its ability to detect early signs of keratoconus. By accurately analysing the cornea, the Zernike polynomials can model even subtle changes in the cornea that may indicate the presence of keratoconus. This is important because early detection of keratoconus can allow for earlier intervention and better outcomes for patients. This method is also functional in differentiating keratoconus from other conditions that may present with similar symptoms, such as corneal dystrophies or corneal scarring. By comparing the minimum required Zernike terms of different patients, it is possible to intuitively recognize the pathological corneas. This can help ophthalmologists develop more accurate and effective treatment plans for their patients.
In addition to detecting keratoconus, this mathematical approach is also useful in monitoring the progression of the condition over time. By regularly monitoring the Zernike terms, ophthalmologists can make adjustments to treatment plans as needed and provide more effective care for their patients. Moreover, based on the fact that the corneal surface is typically a very smooth surface, with this representation it is possible to eliminate the measurement errors by choosing the appropriate number of Zernike terms. The number of the Zernike polynomials should be high enough to describe the detailed surface information of each patient, but low enough to not represent unwanted local roughness of the surface. So the issue that should be taken into account is the sufficient accuracy of the measurement data. Using Zernike representation or representation with polynomials, in general, has several other disadvantages that should also be mentioned. These disadvantages include:
Limited Spatial Resolution: Polynomials can struggle to represent high-frequency surface details or sharp transitions accurately. This limitation makes them less suitable for describing surfaces with fine features.
Global Representation: Polynomials represent the entire surface with a single set of coefficients. This global representation may not be ideal for surfaces with varying characteristics across different regions.
Non-Intuitive Parameters: The coefficients of polynomials do not have an unequivocal physical interpretation, making it challenging to relate them to specific surface features.
In addition to the surface representation with polynomials, there are various other

kinds of surface representations available, including Subdivision Schemes, Splines, Gaussian Process Representations, Fourier Transforms, Implicit Surfaces, and Point Clouds. The choice of surface representation depends on the specific application and the characteristics of the surface being modeled. Different representations offer varying levels of accuracy, ease of manipulation, and computational efficiency. Therefore, it is crucial to select the most suitable one for a given task. In the end, the Zernike representation allows optical designers to import realistic corneal topographic data to optical design software such as ZEMAX Optics Studio or OSLO. The ZEMAX import function which is used in this study is available in Appendix A1. In conclusion, Evaluating the effects of corneal biometry on the optical performance of the eye leads us to design individualized IOLs for correcting refractive errors. However, corneal biometry is not the only variable that can influence the accuracy of the model eye.

In the ray tracing and theoretical models, all eyes receive the same iris representation by weighting the rays based on the distance to the pupil center. With a slightly tilted or decentered lens, the iris weighting moves so that the entire optical performance is affected. As a result. once again the uncertainty of the models limits the accuracy of the wavefront that can be reconstructed in the phakic and pseudophakic individualized eyes. In order to neutralize the effect of the iris weighting displacement, the foveal position is assumed to be fixed in our simulations. With this setting, all the ray bundles are forced to focus on the fovea. Therefore, any tilt or decentration of the lens can not affect the iris weighting function. However, these lens displacements change the incident angle accordingly.

Another factor that can cause refractive errors and influence the optical performance of the eye is the position of the lens inside. In order to increase the accuracy of the model eye, this issue should not be neglected. In realistic conditions, we cannot expect that the IOL is implanted exactly at its perfect position. Therefore, there is always a chance of IOL misalignment in cataract surgery. IOL misalignment may sometimes be caused by incorrect IOL placement at the time of surgery, occasionally by preoperative miscalculation, but it mostly occurs due to spontaneous rotation shortly after implantation. Postoperative rotation may be due to lens design issues, such as slippery materials or haptics that are too small for the capsular bag or to capsular bag issues. The capsular bag equator is often elliptical rather than circular and the haptics tend to seek out the longer axis.

Generally, it is possible to categorize the lens position in both phakic and pseudophakic eyes as axial and lateral. The axial position of the lens has a significant effect on the effective focal length, visual acuity, and depth perception. On the other hand, lateral misalignment of the lens can induce other aberrations in addition to the defocus. Usually, an optical system with decentered or tilted elements exhibits aberrations that can be neglected in centered systems. In addition to the astigmatism of tilted bundles, a coma error also occurs, revealing itself in the image plane in a pattern like a comet tail, and the focus moves in an axial direction, changing the optical system's refractive power. In order to evaluate the effects of lens misalignment on refractive errors of the eye, a simulation approach was chosen based on a modern non-centered schematic eye model (Liou-Brennan). The reason for choosing this asymmetric model eye is in the human eye due to the eccentric position of the fovea, there is no symmetry in the horizontal direction, and the Liou-Brennan model eye is one of the models that considers this. In the human eye, the place of the sharpest vision deviates temporally from the posterior pole. Thus, the eye's visual axis is inclined about 4 -7° in the horizontal direction. In the Liou-Brennan eye, the input beam is tilted by 5° horizontally. Therefore the effect of lens misalignment is not similar in different directions. The effect of lens decentration and tilt on retinal image quality has been extensively studied in the past in simulations and clinical studies. The isolated consideration of decentration and tilt of the lens is an unrealistic simplification, and the combination of both may increase or decrease the impairment of the imaging performance. Our simulations were performed to analyze the effect of combined lens decentration and tilt on the optical performance of phakic and pseudophakic eyes. The horizontal direction for the decentering and the tilting around the vertical axis was chosen since the eye does not show any symmetry in the horizontal direction anyway due to the tilting of the visual axis.

In both phakic and pseudophakic eyes, for clearly positive decentration and tilting values, the highest positive value occurs in the defocus, and the highest positive value occurs in regular astigmatism. The values of defocus and astigmatism are significantly higher in the pseudophakic eye compared to the phakic eye. In the case of the horizontal coma, the characteristics of the phakic and pseudophakic eye are different from defocus and astigmatism. There is symmetry between the positive and negative coma in the phakic eye but not in the pseudophakic eye. The imaging quality in the phakic and pseudophakic eyes deteriorates significantly when the lens is decentered in the horizontal direction and tilted about the vertical axis. It should be mentioned that to make the simulations as realistic as possible, in the pseudophakic simulation, the IOL model simulated was inspired by the Tecnis Z9000 design since this IOL is widespread and the design data was published by the Tecnis company.

The simulations show that in cataract surgery with the implantation of an artificial lens, a refractive error is to be expected whenever the haptic plane of the artificial lens is decentered or tilted about the equatorial plane of the natural eye lens. Astigmatism caused by this refraction error can't be explained primarily by corneal astigmatism as measured by keratometry, topography, or tomography. However, in addition to the correctable refractive errors of defocus and astigmatism, a significant imaging error also occurs with the coma, which cannot be corrected with classic correction methods such as glasses or contact lenses. It should be noted here that the reference parameters used in the optical simulations are based on statistical studies and cannot be expected to achieve the same results with individualized corneal tomography and different IOLs. However, it can be concluded that in addition to the measurement uncertainties of the corneal biometrics and the permissible manufacturing tolerance for artificial lenses, IOL misalignments can be one of the causes of the limitation of the prediction accuracy of modern cataract surgery.

So far with a combination of IOL models and corneal topographies, it is only possible to model most of the potential refractive errors of cataract surgery for any patient to a realistic extent. Considering the fact that not all of the visual errors originate from the refraction of light from the IOL, it is also required to model additional visual errors originating from other interactions of light and IOL. In addition to refractive errors, some other photic phenomena can influence the visual performance of the human eye. These phenomena could be the consequence of other interactions (instead of refraction) between light and the eye. Several studies have investigated IOL positioning and design to reduce photic effects. The location and relative intensity of photic effects can be affected by the IOL edge design, as reported by Holladay et al. Additionally, it has been reported that modifying the IOL design (having a peripheral concave posterior surface) produces more homogeneous lighting of the peripheral nasal retina and may subsequently decrease negative dysphotopsia. As a result, modifying the optical properties of the IOLs' different surfaces can be one of the approaches to reducing photic effects.

The main interactions between light and the different components of the eye are transmission, scattering, and absorption. These interactions can cause the detection of photic phenomena that are not directly correlated to the imaging of an object. Therefore, the exact amount of visual disturbance is unpredictable and varies from patient to patient. But ray tracing simulations of these photic effects with standard models can predict them under statistically frequent conditions (Liou-Brennan eye model and Z9000 IOL model).

In order to have a better evaluation, the ray tracing results are categorized based on their shape and intensity. It has been observed that several photic patterns shift in shape as the incident ray angle increases, moving from the nasal part of the retina to the retina's centre. Similar to this, some other photic patterns with various sizes and shapes located in the center moved temporally at the retina. The same behaviour with a different quality was observed when the clear optical diameter of the simulated IOL increased from 6 mm to 7 mm. Therefore, regardless of IOL size, there should be a specific incident angle where photic effects end up in the foveal region. Additionally, it is observed that the photic effects disappear in the nasal region of the retina with a thin-edge design. Therefore, it can be concluded that the edge surface of the IOL generates this group of photic effects. Since the thin-edge IOLs are unrealistic (there should be a minimum edge thickness for haptics), the simulations continued with thick-edge IOLs. To put it in a nutshell, the bigger and thicker IOLs generate larger and more intense photic patterns on the central region of the retina respectively. On the other hand, the smaller and thinner IOLs can cause larger and more intense photic patterns on the peripheral region of the retina.

By changing the optical properties of the IOL's edge surface, it is possible to change or eliminate the specific incident angle at which photic effects appear on the fovea. This approach can also help us categorize the photic effects based on their origin. Accordingly, they can be identified from the reflection, transmission, or scatter of light from the edges. Moreover, by eliminating the photic effect originating from the edges with an absorbing edge design, it is also possible to identify the ray bundle that passes through the interspace between the IOL and pupil. As a result, changing the edge design has no impact on this group of photic patterns located in the periphery of the nasal region. Investigating only the shape and origin of the photic effects cannot be sufficient to understand whether they are disturbing for the patients or not. Because some parts of the retina are more or less sensitive to light than others, there should be a correlation between the location of the photic effects and the severity of the patient's visual disturbance. The other key factor in experiencing visual disturbance from photic effects is their intensity. If the intensity of the photic effects is too low, they cannot be detected by the patients. Therefore, photic effects cause no visual disturbance, even if they end up in the foveal region (the most sensitive region of the retina).

In addition to the detector located at the pupil, three supplementary intensity detectors are implanted in different regions of the model eye to measure the intensity of light in each region. These three additional detectors are located at the IOLs' edge surface, the periphery of the nasal side of the retina, and the fovea, separately. With these three additional detectors, it is possible to calculate the intensity of the photic effects

which are categorized by their origin before. Moreover, by normalizing the measured intensity by the total intensity passing through the pupil, we can predict whether the photic effects' intensity can cause visual disturbance after cataract surgery or not.
In the end, the combination of these four simulation studies helps us to have more accurate models which can partially predict the impacts of the imperfection of the corneal surfaces, IOL design and alignment, and ocular biometry in different incidence angles on the visual performance of the patients. This study has the character of a pilot study and our principal aim has been to inform ophthalmologists about potential postcataract visual errors. The simulations do not have 100% accuracy and can not replicate a patient eye completely but the author made an attempt to upgrade common eye models to individualized eye models which differentiate from patient to patient. Our simulation models also have some limitations that should be addressed.

5.1 Limitations of our study

The accuracy of the modelling of individualized eyes is limited by the measurement uncertainties of the refractive index, uncertainties in the axial length measurement, fluctuations in the corneal shape and uncertainties in the positioning of the virtual fovea in the ray tracing model. While the measurement uncertainty of the refractive indices primarily affects the refractive index of the IOL and the fluctuations in the corneal shape represent a decisive limitation for the imaging performance that can be achieved with individualized model eyes. In certain circumstances, an additional assessment of the effects of cataract surgery on the corneal geometry may be helpful. However, the major limitations contain the representation the corneal surfaces with polynomials. Generally, the Zernike representation has a limited spatial resolution. This refers to the inherent difficulty of accurately capturing high-frequency details or sharp transitions on a surface using Zernike polynomials. This limitation arises due to the specific mathematical properties of Zernike polynomials, which are primarily designed for describing smoothly varying surfaces. In some specific cases with a single off-centre irregularity in the surface like corneal scar, a local representation using different approaches like subdivision or Gaussian process is much more functional.
The next largest source of uncertainties after the fluctuations in the corneal shape, is the positioning of the virtual fovea (axial length of the eye). An extension of the ray

tracing models by estimating the relative position of the fovea to the video keratometry axis can reduce these uncertainties.
Moreover, most of the IOL manufacturers do not present references confirming their common designs. Therefore for most of the IOL models, it is possible to evaluate their optical performance of them after cataract surgery in the individualized simulation models. But this study can help IOL manufacturers to predict postoperative visual errors partly.

5.2 Conclusions and Outlook

This work used ray-tracing models to simulate individualized phakic and pseudophakic eyes. These models help us to predict potential refractive and visual errors after cataract surgery. The first benefit of these prediction models is reducing cataract surgery risks. Moreover, more accurate models help eye surgeons to choose more compatible IOL models for patients. On top of that, individualized ray-tracing models are a great tool to calculate some of the visual errors which are not possible to measure with an experimental or clinical ophthalmic device.
These ray-racing models could also improve the calculation and design of individualized IOLs. With the help of these models, individualized IOLs with free-form optics for aberration correction can be effectively determined in normal eyes and keratoconus eyes. The individualization of IOLs currently used in everyday clinical practice is limited to the selection of toric IOLs with appropriate correction of astigmatic and spherical aberrations. But with more accurate models, it is possible to design aberration correcting IOLs for each patient. Compared to the standard IOL, the individualized IOL showed a particularly large reduction in the wavefront aberrations in the eyes of keratoconus patients. It has been established that IOL alignment errors are key determinants of image quality that can be achieved with the help of individualized IOLs. A better prediction of the IOL orientation could improve the calculation of the individualized IOL. At the same time, haptic geometries for the IOL should be designed in such a way that decentration is minimized.
Moreover, many keratoconus patients are relatively young and are not candidates for cataract surgery. They could benefit from treatment with a phakic IOL, which is implanted in the eye in addition to the natural lens to compensate for the aberrations. The accommodation is preserved.

The optics of such a phakic IOL can be individualized based on similar ray tracing models as was done here for pseudophakic eyes. Other groups of patients who may benefit particularly strongly from individualized models are patients after a corneal transplant, after refractive surgery or with other corneal pathologies. With the help of these models, it is possible to calculate the optical performance of their eyes more accurately.
In conclusion, individualized prediction eye models are beneficial in several aspects but they can not represent a patient's eye completely. Therefore, further investigation studies are required to make them even more accurate.

Bibliography

[1] Olsen T (2007). Calculation of intraocular lens power: a review. **in**: Acta Ophthalmologica Scandinavica 85.5: 472–485.

[2] Atchison DA, Smith G, Smith G (2000). Optics of the human eye. **volume** 35. Butterworth-Heinemann Oxford.

[3] Dubbelman M, Weeber HA, Van Der Heijde RG, Völker-Dieben HJ (2002). Radius and asphericity of the posterior corneal surface determined by corrected Scheimpflug photography. **in**: Acta Ophthalmologica Scandinavica 80.4: 379–383.

[4] Garner LF, Owens H, Yap M, Frith MJ, Kinnear RF (1997). Radius of curvature of the posterior surface of the cornea. **in**: Optometry and Vision Science: Official Publication of the American Academy of Optometry 74.7: 496–498.

[5] Lam AK, Douthwaite WA (1997). Measurement of posterior corneal asphericity on Hong Kong Chinese: a pilot study. **in**: Ophthalmic and Physiological Optics 17.4: 348–356.

[6] Le Grand Y, El Hage S (1980). Physiological Optics 1Springer-Verlag. **in**: New York 19802.

[7] Gross H, Blechinger F, Achtner B (2008). Human eye. **in**: Handbook of Optical Systems: Volume 4: Survey of Optical Instruments 4: 1–87.

[8] Schwiegerling JT (2013). Eye axes and their relevance to alignment of corneal refractive procedures.

[9] Mosquera SA, Verma S, McAlinden C (2015). Centration axis in refractive surgery. **in**: Eye and Vision 2.1: 1–16.

[10] Applegate RA, Thibos LN, Twa MD, Sarver EJ (2009). Importance of fixation, pupil center, and reference axis in ocular wavefront sensing, videokeratography, and retinal image quality. **in**: Journal of Cataract & Refractive Surgery 35.1: 139–152.

[11] Holden BA, Fricke TR, Wilson DA, Jong M, Naidoo KS, Sankaridurg P, Wong TY, Naduvilath TJ, Resnikoff S (2016). Global prevalence of myopia and high

myopia and temporal trends from 2000 through 2050. **in**: Ophthalmology 123.5: 1036–1042.

[12] Read SA, Collins MJ, Carney LG (2007). A review of astigmatism and its possible genesis. **in**: Clinical and Experimental Optometry 90.1: 5–19.

[13] Foster P, Jiang Y (2014). Epidemiology of myopia. **in**: Eye 28.2: 202–208.

[14] Artal P (2017). Handbook of visual optics, two-volume set. CRC Press.

[15] Khurana A (2008). Errors of refraction and binocular optical defects. **in**: Theory And Practice Of Optics And Refraction: 460.

[16] Strenk SA, Strenk LM, Koretz JF (2005). The mechanism of presbyopia. **in**: Progress in retinal and eye research 24.3: 379–393.

[17] Rabinowitz YS (1998). Keratoconus. **in**: Survey of ophthalmology 42.4: 297–319.

[18] Schedin S, Hallberg P, Behndig A (2016). Three-dimensional ray-tracing model for the study of advanced refractive errors in keratoconus. **in**: Applied Optics 55.3: 507–514.

[19] Krachmer JH, Feder RS, Belin MW (1984). Keratoconus and related noninflammatory corneal thinning disorders. **in**: Survey of ophthalmology 28.4: 293–322.

[20] Lee LR, Hirst LW, Readshaw G (1995). Clinical detection of unilateral keratoconus. **in**: Australian and New Zealand journal of ophthalmology 23.2: 129–133.

[21] Fecarotta CM, Huang WW (2014). Pediatric genetic disease of the cornea. **in**: Journal of Pediatric Genetics 3.04: 195–207.

[22] Goebels S, Eppig T, Seitz B, Langenbucher A (2013). Early detection of keratoconus system assisted screening methods today. **in**: Clinical Monthly Journals for Ophthalmology 230.10: 998–1004.

[23] Zuberbuhler B, Haefliger E, Menapace R, Neuhann T (2008). Kataraktchirurgie. Springer-Verlag.

[24] Allen D, Vasavada A (2006). Cataract and surgery for cataract. **in**: Bmj 333.7559: 128–132.

[25] Zhao L **andothers** (2015). Lanosterol reverses protein aggregation in cataracts. **in**: Nature 523.7562: 607–611.

[26] Stark Jr W **andothers** (1983). Intraocular lenses: complications and visual results. **in**: Transactions of the American Ophthalmological Society 81: 280.

[27] Ascaso FJ, Huerva V, Grzybowski A (2015). Epidemiology, etiology, and prevention of late IOL-capsular bag complex dislocation: review of the literature. **in**: Journal of ophthalmology 2015.

[28] Lundgren B, Jonsson E, Rolfsen W (1992). Secondary cataract: an in vivo model for studies on secondary cataract in rabbits. **in**: Acta Ophthalmologica 70.S205: 25–28.

[29] Capon MR, Docchio F, Leoni G, Trabucchi G, Brancato R (1990). Comprehensive study of damage to intraocular lenses by single and multiple nanosecond neodymium: YAG laser pulses. **in**: Journal of Cataract & Refractive Surgery 16.5: 603–610.

[30] MacEwen C, Baines P (1989). Retinal detachment following YAG laser capsulotomy. **in**: Eye 3.6: 759–763.

[31] Meucci G, Esente S, Esente I (1991). Anterior capsule cleaning with an ultrasound irrigating scratcher. **in**: Journal of Cataract & Refractive Surgery 17.1: 75–79.

[32] Zaturinsky B, Naveh N, Saks D, Solomon AS (1990). Prevention of posterior capsular opacification by cryolysis and the use of heparinized irrigating solution during extracapsular lens extraction in rabbits.

[33] Setty S, Percival S (1989). Intraocular lens design and the inhibition of epithelium. **in**: British journal of ophthalmology 73.11: 918–921.

[34] Masket S, Fram NR (2021). Pseudophakic dysphotopsia: review of incidence, cause, and treatment of positive and negative dysphotopsia. **in**: Ophthalmology 128.11: e195–e205.

[35] Tester R, Pace NL, Samore M, Olson RJ (2000). Dysphotopsia in phakic and pseudophakic patients: incidence and relation to intraocular lens type. **in**: Journal of Cataract & Refractive Surgery 26.6: 810–816.

[36] Davison JA (2000). Positive and negative dysphotopsia in patients with acrylic intraocular lenses. **in**: Journal of Cataract & Refractive Surgery 26.9: 1346–1355.

[37] Holladay JT, Zhao H, Reisin CR (2012). Negative dysphotopsia: the enigmatic penumbra. **in**: Journal of Cataract & Refractive Surgery 38.7: 1251–1265.

[38] Makhotkina NY, Berendschot TT, Beckers HJ, Nuijts RM (2015). Treatment of negative dysphotopsia with supplementary implantation of a sulcus-fixated intraocular lens. **in**: Graefe's Archive for Clinical and Experimental Ophthalmology 253.6: 973–977.

[39] Heitz R, Enoch J (1987). Leonardo da Vinci: An assessment on his discourses on image formation in the eye. **in**: Advances in Diagnostic Visual Optics: 19–26.

[40] Hellemans A, Bunch BH **andothers** (1988). Timetables of science. Simon **and** Schuster.

[41] Farandos NM, Yetisen AK, Monteiro MJ, Lowe CR, Yun SH (2015). Contact lens sensors in ocular diagnostics. **in**: Advanced healthcare materials 4.6: 792–810.

[42] Watts A, Colby K (2016). Contact Lenses for Keratoconus 16. **in**: Keratoconus: Recent Advances in Diagnosis and Treatment: 187.

[43] Atchison DA (1989a). Optical design of intraocular lenses. I. On-axis performance. **in**: Optometry and vision science: official publication of the American Academy of Optometry 66.8: 492–506.

[44] — (1989b). Optical design of intraocular lenses. II. Off-axis performance. **in**: Optometry and vision science: official publication of the American Academy of Optometry 66.9: 579–590.

[45] — (1989c). Optical design of intraocular lenses. III. On-axis performance in the presence of lens displacement. **in**: Optometry and Vision Science: Official Publication of the American Academy of Optometry 66.10: 671–681.

[46] Langenbucher A, Schröder S, Cayless A, Eppig T (2017). Aberration-free intraocular lenses–what does this really mean? **in**: Zeitschrift für Medizinische Physik 27.3: 255–259.

[47] Kaur M, Shaikh F, Falera R, Titiyal JS (2017). Optimizing outcomes with toric intraocular lenses. **in**: Indian journal of ophthalmology 65.12: 1301.

[48] Langenbucher A, Eppig T, Cayless A, Gatzioufas Z, Wendelstein J, Hoffmann P, Szentmáry N (2021). Simulation of Corneal imaging properties for near objects. **in**: Ophthalmic and Physiological Optics 41.5: 1152–1160.

[49] Rampat R, Gatinel D (2021). Multifocal and extended depth-of-focus intraocular lenses in 2020. **in**: Ophthalmology 128.11: e164–e185.

[50] Osipov V, Doskolovich LL, Bezus EA, Cheng W, Gaidukeviciute A, Chichkov B (2012). Fabrication of three-focal diffractive lenses by two-photon polymerization technique. **in**: Applied Physics A 107.3: 525–529.

[51] Cochener B, Group CS **andothers** (2016). Clinical outcomes of a new extended range of vision intraocular lens: International Multicenter Concerto Study. **in**: Journal of Cataract & Refractive Surgery 42.9: 1268–1275.

[52] Fyodorov S (1967). Estimation of optical power of the intraocular lens. **in**: Vestn Oftalmol 80: 27–31.

[53] Shammas HJ (2004). Intraocular lens power calculations. Slack Incorporated.

[54] Olsen T (2006). Prediction of the effective postoperative (intraocular lens) anterior chamber depth. **in**: Journal of Cataract & Refractive Surgery 32.3: 419–424.

[55] Wang W, Miao Y, Savini G, McAlinden C, Chen H, Hu Q, Wang Q, Huang J (2017). Precision of a new ocular biometer in eyes with cataract using swept source optical coherence tomography combined with Placido-disk corneal topography. **in**: Scientific Reports 7.1: 1–8.

[56] Binkhorst R (1975). The optical design of intraocular lens implants. **in**: Ophthalmic surgery 6.3: 17–31.

[57] Colenbrander M (1973). Calculation of the power of an iris clip lens for distant vision. **in**: The British Journal of Ophthalmology 57.10: 735.

[58] Hoffer K (1984). The effect of axial length on posterior chamber lenses and posterior capsule position. **in**: Current concepts in Ophthal Surg 1: 20–22.

[59] Retzlaff JA, Sanders DR, Kraff MC (1990). Development of the SRK/T intraocular lens implant power calculation formula. **in**: Journal of Cataract & Refractive Surgery 16.3: 333–340.

[60] Hoffer KJ (1993). The Hoffer Q formula: a comparison of theoretic and regression formulas. **in**: Journal of Cataract & Refractive Surgery 19.6: 700–712.

[61] Martinez-Enriquez E, Pérez-Merino P, Durán-Poveda S, Jiménez-Alfaro I, Marcos S (2018). Estimation of intraocular lens position from full crystalline lens geometry: towards a new generation of intraocular lens power calculation formulas. **in**: Scientific Reports 8.1: 1–11.

[62] Cooke DL, Cooke TL (2019). A comparison of two methods to calculate axial length. **in**: Journal of Cataract & Refractive Surgery 45.3: 284–292.

[63] Haigis W, Lege B, Miller N, Schneider B (2000). Comparison of immersion ultrasound biometry and partial coherence interferometry for intraocular lens calculation according to Haigis. **in**: Graefe's archive for clinical and experimental ophthalmology 238: 765–773.

[64] Hitzenberger CK (1991). Optical measurement of the axial eye length by laser Doppler interferometry. **in**: Investigative ophthalmology & visual science 32.3: 616–624.

[65] Franken S (1962). Measuring the length of the eye with the help of ultrasonic echo. **in**: Ophthalmologica 143.2: 82–85.

[66] Binkhorst RD (1981). The accuracy of ultrasonic measurement of the axial length of the eye.

[67] Binkhorst R (1987). **?**Biometric A scan ultrasonography and intraocular lens power calculation**?** **in**: *Current Concepts in Cataract Surgery; Selected Proceedings of the Fifth Biennial Cataract Surgical Congress*. CV Mosby.

[68] Fercher A, Mengedoht K, Werner W (1988). Eye-length measurement by interferometry with partially coherent light. **in**: Optics letters 13.3: 186–188.

[69] Hitzenberger C, Mengedoht K, Fercher A (1989). Laser optic measurements of the axial length of the eye. **in**: Fortschritte der Ophthalmologie: Zeitschrift der Deutschen Ophthalmologischen Gesellschaft 86.2: 159–161.

[70] Huang D **andothers** (1991). Optical coherence tomography. **in**: science 254.5035: 1178–1181.

[71] Liang J, Grimm B, Goelz S, Bille JF (1994). Objective measurement of wave aberrations of the human eye with the use of a Hartmann–Shack wave-front sensor. **in**: JOSA A 11.7: 1949–1957.

[72] Alpern M (1978). The eyes and vision. **in**: Handbook of Optics, Optical Society of America.

[73] Tunnacliffe AH (1997). Introduction to visual optics. Association of British Dispensing Opticians.

[74] Le Grand Y (1964). Optique physiologique: La dioptrique de l'oeil et sa correction. Tome premier. Éditions de la Revue d'Optique.

[75] Pedrotti LS, Pedrotti FL (1998). Optics and vision. Addison-Wesley.

[76] Greivenkamp JE, Schwiegerling J, Miller JM, Mellinger MD (1995). Visual acuity modeling using optical raytracing of schematic eyes. **in**: American journal of ophthalmology 120.2: 227–240.

[77] Kooijman AC (1983). Light distribution on the retina of a wide-angle theoretical eye. **in**: JOSA 73.11: 1544–1550.

[78] Navarro R (2009). The optical design of the human eye: a critical review. **in**: Journal of Optometry 2.1: 3–18.

[79] Liou HL, Brennan NA (1997). Anatomically accurate, finite model eye for optical modeling. **in**: JOSA A 14.8: 1684–1695.

[80] Almeida MSd, Carvalho LA (2007). Different schematic eyes and their accuracy to the in vivo eye: a quantitative comparison study. **in**: Brazilian Journal of Physics 37.2A: 378–387.

[81] Manual Z (2007). ZEMAX Development Corporation. **in**: WA, USA.

[82] Aristodemou P, Cartwright NEK, Sparrow JM, Johnston RL (2011). Intraocular lens formula constant optimization and partial coherence interferometry biometry: refractive outcomes in 8108 eyes after cataract surgery. **in**: Journal of Cataract & Refractive Surgery 37.1: 50–62.

[83] Hill WE, Abulafia A, Wang L, Koch DD (2017). Pursuing perfection in IOL calculations. II. Measurement foibles: measurement errors, validation criteria, IOL constants, and lane length. **in**: Journal of Cataract & Refractive Surgery 43.7: 869–870.

[84] Iskander DR, Collins MJ, Davis B (2001). Optimal modeling of corneal surfaces with Zernike polynomials. **in**: IEEE Transactions on biomedical engineering 48.1: 87–95.

[85] Iskander DR, Morelande MR, Collins MJ, Buehren T (2004). A refined bootstrap method for estimating the Zernike polynomial model order for corneal surfaces. **in**: IEEE transactions on biomedical engineering 51.12: 2203–2206.

[86] Langenbucher A, Szentmáry N, Cayless A, Wendelstein J, Hoffmann P (2023). Technical variability of cornea parameters derived from anterior segment OCT fitted with Fringe Zernike polynomials. **in**: Graefe's Archive for Clinical and Experimental Ophthalmology: 1–13.

[87] Narváez J, Banning CS, Stulting RD (2005). Negative dysphotopsia associated with implantation of the Z9000 intraocular lens. **in**: Journal of Cataract & Refractive Surgery 31.4: 846–847.

[88] Radford SW, Carlsson AM, Barrett GD (2007). Comparison of pseudophakic dysphotopsia with Akreos Adapt and SN60-AT intraocular lenses. **in**: Journal of Cataract & Refractive Surgery 33.1: 88–93.

6 Publications

[1] Langenbucher A, Omidi P, Eppig T, Szentmáry N, Menapace R, Hoffmann P (2021).Combination of lens decentration and tilt in phakic and pseudophakic eyes—optical simulation of defocus, astigmatism and coma. **in**: Der Ophthalmologe 118:828-37.

[2] Omidi P, Cayless A, Langenbucher A (2022). Simulation of photic effects after cataract surgery for off-axis light sources. **in**: Plos one 17(1):e0262457.

[3] Omidi P, Cayless A, Langenbucher A (2022). Evaluation of optimal Zernike radial degree for representing corneal surfaces. **in**: Plos one 17(5):e0269119.

[4] Omidi P, Cayless A, Langenbucher A (2022). Intensity simulation of photic effects after cataract surgery for off-axis light sources. **in**: Plos one 17(8):e0272705.

[5] Borkenstein AF, Borkenstein EM, Omidi P, Langenbucher A (2022). Evaluating impact of Nd: YAG laser associated defects on optical quality of hydrophilic and hydrophobic intraocular lenses using visualization of light propagation and USAF test targets. **in**: BMC ophthalmology 22.1: 1-9.

[6] Omidi P, Cayless A, Langenbucher A (2023). EDOF intraocular lens design: shift in image plane vs object vergence. **in**: BMC ophthalmology 23(1):397.

[7] Borkenstein AF, Borkenstein EM, Omidi P, Langenbucher A (2023). Image contrast and spectral transmission in intraocular lenses with Nd: YAG pits. **in**: Current Eye Research: 1-8.

7 Abbreviations and Mathematical Symbols

Abbreviations

IOL	Intraocular lens
dpt	Diopter
OCT	Optical coherence tomography
AS-OCT	Anterior segment optical coherence tomography
LASIK	Laser assisted in situ keratomileusis
PCO	Posterior capsule opacification
YAG	Yttrium Aluminum Garnett
PD	Positive dysphotopsia
ND	Negative dysphotopsia
ACD	Anterior chamber depth
RGP	Rigid gas permeable
PMMA	Polymethyl methacrylate
MF	Multifocal
EDOF	Extended depth of focus
ELP	Effective lens position
AL	Axial length
RNFL	Retinal nerve fiber layer
AMD	Age-related macular degeneration

Mathematical Symbols

P	Intraocular lens power
n_{Eye}	Refractive index of the eye
n_{Cornea}	Refractive index of the Cornea
AL	Axial length
ELP	Effective lens position
K	Keratometry value
Ref	Target Refraction
R	Radius of the cornea
d	Distance between the reflective surface and the object
O	Object size
I	Image size
Z	Surface sag
c	Surface curvature
c_x	Surface curvature cross the x-axis
c_y	Surface curvature cross the y-axis
r	Radial ray coordinate in lens units
x	Ray coordinate on the x-axis
y	Ray coordinate on the y-axis
k	Surface conic constant
α_i	Polynomial aspheric coefficient
N	Number of Zernike coefficients
A_i	Coefficient on the i^{th} Zernike standard polynomial
ρ	Normalized radial ray coordinate
φ	Angular ray coordinate
z	Z coordinate along the optical axis
n_0	Base refractive index
n_{ri}, n_{zi}	Index coefficients for a parabolic gradient

8 Acknowledgments

At this point, I would like to thank everyone who supported me during my time as a doctoral student and research assistant at the Institute of Experimental Ophthalmology at Saarland University. This includes in particular the persons/companies who have directly contributed to this dissertation. My work as a research assistant was supported in part by the Rolf M. Schwiete Stiftung under project nr. 11/2018 [1].

Special thanks go to my supervisor Prof. Dr. Achim Langenbucher. He gave me the opportunity to write this thesis, supported me and advised me. Our joint discussions were motivating and proved extremely helpful. I would like to thank Prof. Dr. Timo Eppig for his good cooperation in the various projects at the Institute of Experimental Ophthalmology. Thanks to his extensive experience in the field of optical simulation and metrology, he often had practical tips for me.

I want to take this opportunity to thank the other current or former institute members Dr. Simon Schröder, Dr. Stephanie Mäurer, Angela Damian, Michael Schwemm, Jan Schatteburg, and Mona Mojerloo for the productive working atmosphere.

Furthermore, I would like to thank the co-operators and co-authors during my time as a doctoral student. thanks for the successful cooperation of Dr. Alan Cayless, Dr. Nóra Szentmáry, Dr. Rupert Menapace, Dr. Peter Hoffmann, Dr. Andreas F Borkenstein, Dr. Eva-Maria Borkenstein, Dr. Timo Eppig, Dr. Loay Daas, Dr. Berthold Seitz and Dr. Hakan Kaymak.

Finally, I would also like to thank my family, especially my parents who endured the hardship of my being away from them and my homeland.

My sincere gratitude
Pooria Omidi.

[1] https://schwiete-stiftung.com

9 Curriculum Vitae

The curriculum vitae was removed from the electronic version of the doctoral thesis for reasons of data protection.

10 Appendix

10.1 MATLAB Code: CASIA 2 Import Function

```
clc;
close all;
clear all;
verzeichnis = 'File Directory';
%% Importing Data
filename = strcat(verzeichnis,'CASIA2 File name'); %Indicate File Name
R = importfile(filename,25,56); %Radius Data [mm]
radius=4; % 4mm or 5mm
pixel=radius*50;
R = [zeros(32,1),R];
R1=R./radius; %Normalization

ZA = importfile(filename,410,441);%Anterior Height [um]
ZA = ZA(1:32,1:pixel);
ZA = [zeros(32,1),ZA];
ZA = ZA*10e-4;%Anterior Height [mm]

ZP = importfile(filename,445,476);%Posterior Height [um]
ZP=ZP-ZP(1,2);%Remove offset
ZP = ZP(1:32,1:pixel);
ZP= [zeros(32,1),ZP];
ZP= ZP*10e-4;%Posterior Height [mm]

%% Creating a Matrix for Meridians
T = (0:pi/16:31*pi/16).*ones(1,pixel+1);

%% Calculating Zernike Coefficients
Data=ZP;%ZA for Anterior and ZP for Posterior
R1=reshape(R1,[],1);
T1=reshape(T,[],1);
```

```
DataA=reshape(Data,[],1);
n=12; %Indicate the maximum radial degree
ad1,nm1=zernmodfit(R1,T1,DataA,n);

%% Reconstructing the Surface and Calculate STD
Nz = size(ad1,1);
z1=zeros(size(R1,1),1);
error = zeros(1,Nz);
for k = 1:Nz
z1=...
z1 + ad1(k,1)*zernfun(nm1(k,1),nm1(k,2),R1,T1 + ad1(k,2));
Delta1=DataA-z1;
error1(1,k)=std(Delta1);
end

%% Extracting Standard Zernike Coefficients
zern=zeros(1,91);
zern(1)=ad1(1,1); %Piston
zern(2)=(1/sqrt(4))*ad1(2,1)*cos(+1*ad1(2,2));%Tilt x
zern(3)=(1/sqrt(4))*ad1(2,1)*sin(-1*ad1(2,2));%Tilt y
zern(4)=(1/sqrt(3))*ad1(3,1);%Defocus
zern(5)=(1/sqrt(6))*ad1(4,1)*sin(-2*ad1(4,2));%Astigmatism x
zern(6)=(1/sqrt(6))*ad1(4,1)*cos(+2*ad1(4,2));%Astigmatism y
zern(7)=(1/sqrt(8))*ad1(5,1)*sin(-1*ad1(5,2));%Coma x
zern(8)=(1/sqrt(8))*ad1(5,1)*cos(+1*ad1(5,2));%Coma y
zern(9)=(1/sqrt(8))*ad1(6,1)*sin(-3*ad1(6,2));%Trefoil x
zern(10)=(1/sqrt(8))*ad1(6,1)*cos(+3*ad1(6,2));%Trefoil y
zern(11)=(1/sqrt(5))*ad1(7,1);%Primary Spherical
zern(12)=(1/sqrt(10))*ad1(8,1)*cos(+2*ad1(8,2));%Secondary Astigmatism x
zern(13)=(1/sqrt(10))*ad1(8,1)*sin(-2*ad1(8,2));%Secondary Astigmatism y
zern(14)=(1/sqrt(10))*ad1(9,1)*cos(+4*ad1(9,2));%Quadrafoil x
zern(15)=(1/sqrt(10))*ad1(9,1)*sin(-4*ad1(9,2));%Quadrafoil y
zern(16)=(1/sqrt(12))*ad1(10,1)*cos(+1*ad1(10,2));
zern(17)=(1/sqrt(12))*ad1(10,1)*sin(-1*ad1(10,2));
zern(18)=(1/sqrt(12))*ad1(11,1)*cos(+3*ad1(11,2));
zern(19)=(1/sqrt(12))*ad1(11,1)*sin(-3*ad1(11,2));
```

```
zern(20)=(1/sqrt(12))*ad1(12,1)*cos(+5*ad1(12,2));
zern(21)=(1/sqrt(12))*ad1(12,1)*sin(-5*ad1(12,2));
zern(22)=(1/sqrt(7))*ad1(13,1);
zern(23)=(1/sqrt(14))*ad1(14,1)*sin(-2*ad1(14,2));
zern(24)=(1/sqrt(14))*ad1(14,1)*cos(+2*ad1(14,2));
zern(25)=(1/sqrt(14))*ad1(15,1)*sin(-4*ad1(15,2));
zern(26)=(1/sqrt(14))*ad1(15,1)*cos(+4*ad1(15,2));
zern(27)=(1/sqrt(14))*ad1(16,1)*sin(-6*ad1(16,2));
zern(28)=(1/sqrt(14))*ad1(16,1)*cos(+6*ad1(16,2));
zern(29)=(1/sqrt(16))*ad1(17,1)*sin(-1*ad1(17,2));
zern(30)=(1/sqrt(16))*ad1(17,1)*cos(+1*ad1(17,2));
zern(31)=(1/sqrt(16))*ad1(18,1)*sin(-3*ad1(18,2));
zern(32)=(1/sqrt(16))*ad1(18,1)*cos(+3*ad1(18,2));
zern(33)=(1/sqrt(16))*ad1(19,1)*sin(-5*ad1(19,2));
zern(34)=(1/sqrt(16))*ad1(19,1)*cos(+5*ad1(19,2));
zern(35)=(1/sqrt(16))*ad1(20,1)*sin(-7*ad1(20,2));
zern(36)=(1/sqrt(16))*ad1(20,1)*cos(+7*ad1(20,2));
zern(37)=(1/sqrt(9))*ad1(21,1);
zern(38)=(1/sqrt(18))*ad1(22,1)*cos(+2*ad1(22,2));
zern(39)=(1/sqrt(18))*ad1(22,1)*sin(-2*ad1(22,2));
zern(40)=(1/sqrt(18))*ad1(23,1)*cos(+4*ad1(23,2));
zern(41)=(1/sqrt(18))*ad1(23,1)*sin(-4*ad1(23,2));
zern(42)=(1/sqrt(18))*ad1(24,1)*cos(+6*ad1(24,2));
zern(43)=(1/sqrt(18))*ad1(24,1)*sin(-6*ad1(24,2));
zern(44)=(1/sqrt(18))*ad1(25,1)*cos(+8*ad1(25,2));
zern(45)=(1/sqrt(18))*ad1(25,1)*sin(-8*ad1(25,2));
zern(46)=(1/sqrt(20))*ad1(26,1)*cos(+1*ad1(26,2));
zern(47)=(1/sqrt(20))*ad1(26,1)*sin(-1*ad1(26,2));
zern(48)=(1/sqrt(20))*ad1(27,1)*cos(+3*ad1(27,2));
zern(49)=(1/sqrt(20))*ad1(27,1)*sin(-3*ad1(27,2));
zern(50)=(1/sqrt(20))*ad1(28,1)*cos(+5*ad1(28,2));
zern(51)=(1/sqrt(20))*ad1(28,1)*sin(-5*ad1(28,2));
zern(52)=(1/sqrt(20))*ad1(29,1)*cos(+7*ad1(29,2));
zern(53)=(1/sqrt(20))*ad1(29,1)*sin(-7*ad1(29,2));
zern(54)=(1/sqrt(20))*ad1(30,1)*cos(+9*ad1(30,2));
zern(55)=(1/sqrt(20))*ad1(30,1)*sin(-9*ad1(30,2));
```

```
%% Ploting STD
figure (1)
semilogy(error1)
xline(2,'–r','n=2')% Radial degree 2
xline(4,'–r','n=3')% Radial degree 3
xline(6,'–r','n=4')% Radial degree 4
xline(9,'–r','n=5')% Radial degree 5
xline(12,'–r','n=6')% Radial degree 6
xline(20,'–r','n=7')% Radial degree 7
xline(25,'–r','n=8')% Radial degree 8
xline(30,'–r','n=9')% Radial degree 9
xline(36,'–r','n=10')% Radial degree 10
xline(42,'–r','n=11')% Radial degree 11

%% Ploting the Constructed and Reconstructed Cornea
z11=reshape(z1,32,pixel+1);
figure (2)
subplot(1,2,1);
surf(R,T,ZA);
subplot(1,2,2);
surf(R,T,z11);
cummean=zeros(1,pixel*1);
cummedian=zeros(1,pixel*1);
cummax=zeros(1,pixel*1);
for i=1:pixel+1
cummean(i)= mean(mean(abs(Data(:,1:i)-z11(:,1:i))));
cummedian(i) = median(median(abs(Data(:,1:i)-z11(:,1:i))));
cummax(i)=max(max(abs(Data(:,1:i)-z11(:,1:i))));
end
figure (3)
yourx=R(1,:);
plot(yourx,cummean,yourx,cummedian,yourx,cummax)
yourindex= -4<yourx & yourx<4;
plot(yourx(yourindex),cummean(yourindex),yourx(yourindex),cummedian(yourindex))
```

```
%% Exporting Data for ZEMAX
N= 91;
imzern=zeros(N+2,1);
imzern(1,1)=N;
imzern(2,1)=radius;
imzern(3:N+2,1)=zern(1,1:N);
writematrix(imzern,'Any Name.dat','Delimiter',' ');
```

10.2 MATLAB Code: Zernike Fitting Function

```
function [ad,varargout] = zernmodfit(r,theta,data,N)
%ZERNMODFIT Fit data to a modified Zernike basis.
AD = ZERNMODFIT(R,THETA,DATA,N) returns a two-column matrix containing the modal coefficients A and rotation angles (orientation axes) D for DATA expressed at the coordinate locations (R,THETA) within the unit disk. The A and D are computed for all [n m] modes with n = 0 to N, and m = 0:2:n for even n, m = 1:2:n for odd n. R, THETA, and DATA must be vectors, and must contain the same number of elements. N must be a positive integer.

%[AD,NM] = ZERNMODFIT(R,THETA,DATA,N) returns a 2-column matrix NM containing the [n m] mode numbers associated with each (coefficient, angle) pair in the array AD.

%Note: For the m > 0 modes, the computed Zernike coefficients A are always positive, since the orientation axis D for each mode can always be chosen so as to make them positive. For the m = 0 modes, which have no angular dependence, the coefficients can be both positive and negative.

if ( any(size(r )) == 1 ) || ...
( any(size(theta)) == 1 ) ||...
( any(size(data )) == 1 )
error('zernmodfit:NMvectors1','The inputs R, THETA, and DATA must all be vectors.')
end
if ( numel(r) = numel(theta)) || ...
```

```
( numel(r)  = numel(data) ) ||...
( numel(theta)  = numel(data) )
error('zernmodfit:NMvectors2','The inputs R, THETA, and DATA must all have the same number of elements.')
end
if numel(N) > 1
error('zernmodfit:NMvectors4','N must be a single number (scalar - positive integer or zero).')
end
if N < 0 || N  = round(N)
error('zernmodfit:NMvectors3','N must be a positive integer or zero.')
end
r = r(:);
theta = theta(:);
data = data(:);
if any( r>1 | r<0 )
error('zernmodfit:Rlessthan1','All R must be between 0 and 1.')
end

%Build vectors of mode numbers:
n = cellfun(@(x)(x*ones(1,x+1)),num2cell(0:N),'UniformOutput',false);
n = [n:]';
m = cellfun(@(x)([fliplr(-x:2:-1) fliplr(x:-2:0)]),num2cell(0:N),'UniformOutput',false);
m = [m:]';

%Compute the required Zernike functions:
r = r(:);
theta = theta(:);
z = zernfun(n,m,r,theta);
c = z\data(:); %standard Zernike coefficients

%Separate the positive, negative, and zero cases:
cp = c(m>0);
cn = c(m<0);
cz = c(m==0);
```

%Compute the magnitudes and rotation angles from the coefficients:
cnz = sqrt(cp.$^2 + cn.^2$);
dnz = atan2(-cn,cp);
dnz(dnz<0) = dnz(dnz<0) + 2*pi;
dnz = dnz./m(m>0);

%Combine the m==0 and m =0 coefficients and angles into vectors:
a = zeros(size([cz;cnz]));
d = a;
mposandzero = m(m>=0);
iszero = mposandzero==0;
ispos = mposandzero>0;
a(iszero) = cz;
a(ispos) = cnz;
d(iszero) = 0;
d(ispos) = dnz;

%Assign the outputs:
ad = [a d];
varargout = [n(m>=0) m(m>=0)];